The University Of Sheffield.

Avalanche Breakdown Characteristics of Thin $Al_{0.85}Ga_{0.15}As_{0.56}Sb_{0.44}$ Avalanche Photodiodes

By:

Salman Abdullah
M.Eng, B.Eng

A thesis submitted in partial fulfilment of the requirements for the degree of
Doctor of Philosophy

The University of Sheffield
Department of Electronic and Electrical Engineering
Faculty of Engineering

24th May 2019

Acknowledgement

Thanks to Almighty Allah for everything.

Chee Hing Tan and Jo Shien Ng are the people who made this thesis possible. They have been more than supervisors to me. They helped me to grow professionally through the time I have worked with them. They helped me both in and out of work and for that I will always be grateful. I have been very lucky to have worked with them. Throughout these years, I have known them to be very caring, considerate and kind people. They understand the importance of work and family life and they have helped me by going out of their way in many aspects of my professional and personal life. I can't thank them enough for everything they have given me. Thanks to their guidance and rigorous training, I have been offered the position of Photonics Scientist at Seagate Technology, UK even before the award of my doctoral degree. I would like to acknowledge the financial support for this work by PROMIS consortium. Special thanks go to Tony, Susan, Allan and Pamela from Lancaster University for managing the administrative tasks. Thanks to Jose Luis, Flavio Nucciarelli, Emna Amri and Matthieu Legre for their help in making my secondments fruitful. Thanks to the European Commission for funding this work.

Thanks to my colleagues Jon Petticrew, Vladimir Shulyak and Lucas Pinel for the many useful discussions we had together which helped me a great deal in building my understanding. Simon deserves special acknowledgement for his support in smooth conduct of this work. The many discussions I have had with him have helped me a lot during the write up of this thesis. Jon Petticrew and Lucas Pinel are acknowledged for providing data reported in Chapters 4 and 7.

A special thank you to my beloved wife Komal for her support over the years which has enabled me to strike a balance between my work and professional life. Thanks to my son Zahran who has filled my life with joy and laughter. The pleasure of seeing his smiling face and a welcome hug has been the excitement I enjoyed every day after work. Finally, the job offer from Seagate Technology provided me with enthusiasm and motivation to finish my thesis in a timely manner. Thanks to Dr. Kristian Groom from The University of Sheffield and Dr. Jonathan Leach from Herriot-Watt University on providing valuable corrections on my thesis. Thank you once again Professor Tan for being a wonderful boss.

Journal and conference publications

1. **S. Abdullah**, C. H. Tan, X. Zhou, S. Zhang, L. Pinel, and J. Ng, "*Investigation of temperature and temporal stability of $Al_{0.85}Ga_{0.15}As_{0.56}Sb_{0.44}$ avalanche photodiodes*," **Opt. Express 25, 33610-33616 (2017).**
2. L. Pinel, S. Dimler, X. Zhou, **S. Abdullah**, S. Zhang, C. Tan, and J. Ng, "*Effects of carrier injection profile on low noise thin $Al_{0.85}Ga_{0.15}As_{0.56}Sb_{0.44}$ avalanche photodiodes*," **Opt. Express, 26, 3568-3576 (2018).**
3. X. Zhou, C. H. Tan, S. Zhang, M. Moreno, S. Xie, **S. Abdullah**, & J.S. Ng, *"Thin $Al_{1-x}Ga_xAs_{0.56}Sb_{0.44}$ diodes with extremely weak temperature dependence of avalanche breakdown*," **Royal Society Open Science, 4(5), 170071 (2017).**
4. **S. Abdullah**, C.H. Tan, S. Zhang, X. Zhou, L. Pinel and J.S.Ng, " *$Al_{0.85}Ga_{0.15}As_{0.56}Sb_{0.44}$ avalanche photodiodes with high immunity to temperature fluctuation*", SPIE Nanoscience & Engineering Symposium, San Diego, California, US, 2018.
5. **S. Abdullah**, S.J. Dimler, J. Petticrew, V. Shulyak, J.S. Ng and C.H. Tan, "*Timing characteristics of avalanche breakdown in $Al_{0.85}Ga_{0.15}As_{0.56}Sb_{0.44}$ single photon avalanche diodes*" Photonics by the lake conference, Windermere, UK, July, 2018
6. **S. Abdullah**, S.J. Dimler, J. Petticrew, V. Shulyak, J.S. Ng and C.H. Tan, "*Dark count rate and timing characteristics of $Al_{0.85}Ga_{0.15}As_{0.56}Sb_{0.44}$ Geiger mode avalanche photodiodes*", UK Semiconductors conference, Sheffield, UK, July, 2018 .
7. **S. Abdullah**, C. H Tan, L. Pinel, and J. S. Ng, "*Temperature and Temporal Stability of Avalanche Gain for $Al_{0.85}Ga_{0.15}As_{0.56}Sb_{0.44}$ Avalanche Photodiodes*", Semiconductor & Integrated Opto- Electronics (SIOE) Conference, Cardiff, March, 2018.
8. **S. Abdullah**, X. Zhou, S. Zhang, J.S. Ng, C.H. Tan, "*Temporal and Temperature Stability of $Al_{0.85}Ga_{0.15}As_{0.56}Sb_{0.44}$ Avalanche Photodiodes*", UK Semiconductors conference, Sheffield, UK, July, 2017.
9. **S. Abdullah**, L. Pinel, X. Zhou, J.S. Ng and C.H. Tan, "*Determining the capacitance of diodes with high leakage currents*", PROMIS Summer Workshop, Montpellier, France, August 2016. (***Second best student prize for excellence***)

Scope of the project and financial support

This work was financially supported by PROMIS consortium (*Postgraduate Research on Dilute Metamorphic Nanostructures and Metamaterials in Semiconductor Photonics*) which is an initial training network programme funded by the European Union through Horizon 2020 Marie Skłodowska-Curie Actions, grant number H2020-MSCA-ITN-2014-641899. PROMIS network aims to promote photonics as a key-enabling technology for future. The programme is aimed for developing advanced photonic materials and devices for four major application areas including Information and communication technologies (ICT), Security, Energy and Environment, the four work packages of PROMIS consortium. The work done in this thesis is a contribution to the Work Package-2 of the consortium under the project titled "*Nanometre Wide Avalanche Regions for High Performance Single Photon Detectors".* Figure A below shows the constituent projects of the PROMIS consortium.

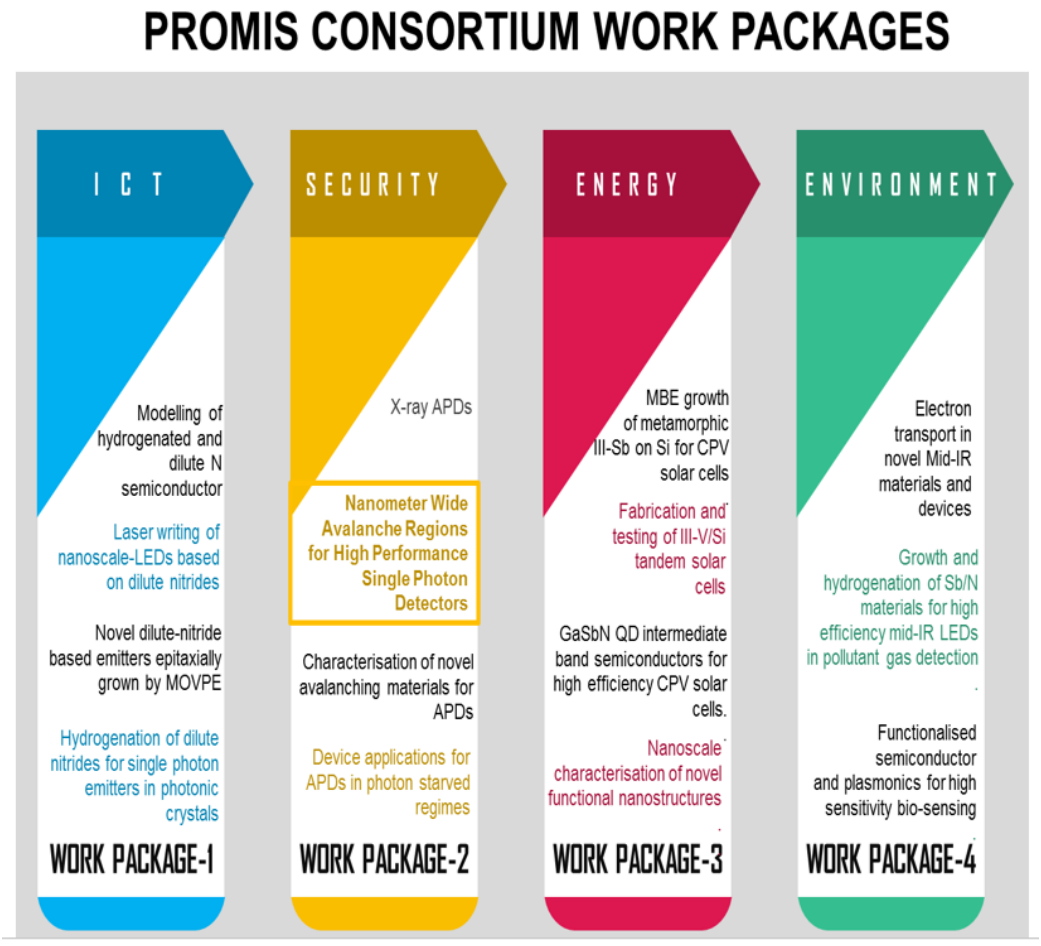

Fig. A. Work packages of the PROMIS consortium.

The network comprises of 8 academic, 2 industrial and 9 associate partners across Europe. The network aims to train a cohort of 15 early stage researchers for a range of skills required in photonics including material growth, device fabrication, characterisation, design, theory and commercialisation. This work is a constituent project of the Work-Package 2 of the PROMIS consortium. The work done in this project involved a number of secondments to associate partners of the consortium at Universidad Autonoma de Madrid, Spain and ID Quantique, SA, Geneva, Switzerland.

Secondments carried out as part of this work

Secondment 1: Autonomous University of Madrid, Madrid, Spain (Oct – Nov' 2016)

The purpose of this placement was to assess Aluminium Nitride (AlN) as a potential sidewall passivation for $Al_{0.85}Ga_{0.15}As_{0.56}Sb_{0.44}$ avalanche photodiodes. The main motivation for AlN is that the surface morphology is better in comparison with Silicon Nitride (the commonly used passivation for $Al_{0.85}Ga_{0.15}As_{0.56}Sb_{0.44}$ APDs and the refractive index is closely matched to Si_3N_4 (SiN). APDs based on a 100 nm nominal thickness of $Al_{0.85}Ga_{0.15}As_{0.56}Sb_{0.44}$ avalanche layer were passivated with AlN using a reactive ion sputtering technique. An Al target was used with a Nitrogen plasma to sputter AlN onto the sidewalls. Dark currents were measured on several device sizes of the $Al_{0.85}Ga_{0.15}As_{0.56}Sb_{0.44}$ APDs before and after the sidewall passivation and the results confirmed that AlN did not degrade the dark currents indicating that it is a stable passivant in comparison with SiN.

Secondment 2: Autonomous University of Madrid, Madrid, Spain (July' 2017)

The purpose of this placement was to perform wet chemical etching of AlGaAsSb APDs. For the passivation studies mentioned under the previous secondment, it is important to passivate the sidewalls right after wet etching as a time lapse between etching and sidewall passivation could potentially risk surface degradation. AlGaAsSb APDs with only top metal contacts were processed at National Epitaxy Facility at Sheffield and photoresist was deposited. Consequently the devices were shipped to Madrid where they

were etched using a sulphuric acid based etchant (for etching InGaAs contact layers) and hydrochloric acid based recipe (for etching AlGaAsSb avalanche layer).

Secondment 3: iD Quantique, IDQ, SA, Geneva, Switzerland (Mar – April' 2018)

iD Quantique, SA is a Swiss company leading global market in single photon detectors for Near Infrared and Quantum Key Distribution (QKD) applications. IDQ was an associate partner of the PROMS consortium and they kindly agreed to characterise Geiger mode AlGaAsSb APDs using their prototype boards. The devices were fabricated at National Epitaxy Facility, Sheffield and were carried to IDQ for subsequent characterisation. The prototype boards at iDQ were custom built to detect and quench avalanche from the Geiger mode AlGaAsSb APDs. Afterpulsing studies were also conducted on the commercial grade single photon detectors *ID-220, ID-210*.

Abstract

Currently Single Photon Avalanche Diodes (SPADs) based on InP multiplication layer dominate the market for single photon detection applications including autonomous driving and remote sensing applications. Major attractions of InP include its wide bandgap (1.46 eV at 296 K) and lattice matching with narrow bandgap absorber $In_{0.47}Ga_{0.53}As$ (0.75 eV at 296 K) which facilitates photon detection at 1550 nm. However a problem with linear and Geiger mode avalanche photodiodes based on InP is their heavy dependence on temperature stabilisation mechanisms owing to higher temperature coefficient of avalanche breakdown of InP (6 mV/K for a nominally 100 nm thick avalanche layer). Moreover thin avalanching layers of InP can suffer from a significant band-to-band tunnelling current. A solution to this problem is an even wider bandgap material that is less susceptible to band to band tunnelling current (due to its wider bandgap) and more temperature robust (due to its temperature insensitive avalanche breakdown). A wider bandgap can reduce the band to band tunnelling currents at high operating fields (typical to Geiger mode detection) whereas a temperature insensitive avalanche breakdown can circumvent the operational complexity of temperature stabilisation circuitries (typical with linear and Geiger mode InP photodiodes). $Al_{0.85}Ga_{0.15}As_{0.56}Sb_{0.44}$ lattice matched to InP substrate is one such material system that provides a wider bandgap (1.59 eV at 296 K) and a reduce temperature dependence of avalanche breakdown (1.60 mV/K for a nominally 100 nm thick layer).

This thesis reports fabrication and characterisation of avalanche photodiodes based on the thin avalanching layers of a novel material $Al_{0.85}Ga_{0.15}As_{0.56}Sb_{0.44}$ lattice matched to InP substrate. The primary objective is to understand the breakdown characteristics of $Al_{0.85}Ga_{0.15}As_{0.56}Sb_{0.44}$ and assess its potential as a replacement for InP Geiger mode APD. The temperature coefficient of avalanche breakdown of *p-i-n* mesa APD based on nominally 100 nm wide avalanche layer of $Al_{0.85}Ga_{0.15}As_{0.56}Sb_{0.44}$ (1.60 mV/K) is 1.56× and 3.75× times smaller than APDs based on InAlAs (2.5 mV/K) and InP (6 mV/K) avalanche layers respectively. As compared to wide bandgap InP and InAlAs, the indirect and wide bandgap of $Al_{0.85}Ga_{0.15}As_{0.56}Sb_{0.44}$ makes it less susceptible to band to band tunnelling currents.

APDs based on 100 nm thick $Al_{0.85}Ga_{0.15}As_{0.56}Sb_{0.44}$ avalanche layer have also demonstrated a promising temporal stability of avalanche gain with a maximum fluctuation of ±1.33% at 353 K. The avalanche gain was to reduce by 15% when the temperature was increased from 294 K to 353 K, compared to 45% and 52% for commercial Si avalanche photodiodes S-5345 and S-6045 respectively. Stable dark current have been observed for $Al_{0.85}Ga_{0.15}As_{0.56}Sb_{0.44}$ avalanche layers and APDs employing these layers show no significant thermal degradation due to gain measurements at elevated temperatures. These attributes are also beneficial for single photon detection applications

Owing to the small device capacitance of the Geiger mode APDs, excellent transient cancellation was achieved which facilitated the detection of weak avalanche signals at low overbias values. The maximum overbias in Geiger mode was limited to 2.5 - 4% due to device design which caused electric field confinement in the avalanche layer. The dark count rate was found to be insensitive to variation in the *DC* bias levels during the gate-OFF time. A stable dark count rate was observed for $Al_{0.85}Ga_{0.15}As_{0.56}Sb_{0.44}$ Geiger mode APDs without relying on temperature stabilisation. A slight increase in dark count rate of 2.46% was recorded over 550 s which is attributed to variation of threshold level while under similar dark count rate conditions, the dark count rate of a Silicon Geiger mode APD decreased by 30%. Studies on dark count rate as function of pulse repetition frequency showed that the detector dead time should be greater than 700 ns to avoid any increase in the dark count due to possible afterpulsing effects. $Al_{0.85}Ga_{0.15}As_{0.56}Sb_{0.44}$ Geiger mode APD demonstrated a potential of room temperature photon detection for shorter overbias pulse durations with reduced dark count rate. An exponential time distribution was recorded in the dark count rate where majority of the breakdown events happen within a well-defined time duration and are registered close to the rising edge of the overbias pulse.

The impact ionisation coefficients were extracted by fitting the experimental data for avalanche gain and excess noise using recurrence method by adjusting the threshold energies field dependence of impact ionisation coefficients. The ionisation coefficients have been extracted for an electric field in the range of 500-1250 kV/cm. using the set of extracted impact ionisation coefficients, breakdown probability was modelled as a function of overbias for Geiger mode APDs based on 100 nm thick $Al_{0.85}Ga_{0.15}As_{0.56}Sb_{0.44}$ avalanche layer. Modelling suggests that the recorded *DCR* increased at a significantly

faster rate than predicted breakdown probability characteristics. This suggests either significant onset of tunnelling current, inaccuracies in ionisation parameters or influence of threshold level used in measurements.

Table of Contents

Dedicated to my father Ameer Abdullah and my mother Bibi Raz

Chapter 1

Introduction

Light detection plays a pivotal role in several cutting edge scientific and industrial research applications. Photon counting has had significant impact on advances in health diagnostics [1], medical analysis and imaging [2], astronomy [3] and biomedical research involving fluorescence detection [4]. The recent development in genomics has been possible by the virtue of microarray technology which detects the chemical reactions between DNA strands and reagents distributed across a microarray slide. Scientists employ the technique of fluorescence detection to achieve this feat and they use single photon detectors to detect the fluorescence. Single photon detectors have also played a crucial role in mapping the human genome [5]. State of the art technologies in single photon detection currently in the market include Photo Multiplier Tubes (PMT) [6], Superconducting Nanowire Single Photon Detectors (SNSPDs) and its variant Superconductive Quantum Interference Devices (SQUID) and Semiconductor Single Photon Avalanche Diodes (SPADs).

1.1 Single Photon Detection Technologies

1.1.1 Photo Multiplier Tubes

Photomultiplier tubes (PMT) have been used conventionally to detect single photon in biomedical imaging, industrial applications and high energy physics experiments [7]. PMT uses the principle of photoelectric effect and secondary electron emission and uses photo-cathodes, focusing electrodes and secondary emission electrodes (Dynodes) for amplifying weak optical signals. Electrons that leave the photo-cathode are accelerated under a high electric field to the first dynode. For each electron striking the dynode, multiple electrons are knocked out of the emissive surface plating the consecutive dynodes. The process is repeated through several

pairs of dynodes and this leads to a high gain. Fluctuation in time taken by electrons to leave the *PMT* results in a broadening of the electrical pulse at the anode. The shape of the output pulse has therefore some broadening with a *FWHM* in the range of few nanoseconds to few hundred nanoseconds. Another figure of merit for *PMT* is the *FWHM* in the variation of the transit time, known as Transit Time Spread (*TTS*). Transit time is the time difference between photon arrival and generation of the output pulse at anode. Typical values include several hundred picoseconds to several nanoseconds. Fig. 1 shows the schematic of the system construction of a *PMT*.

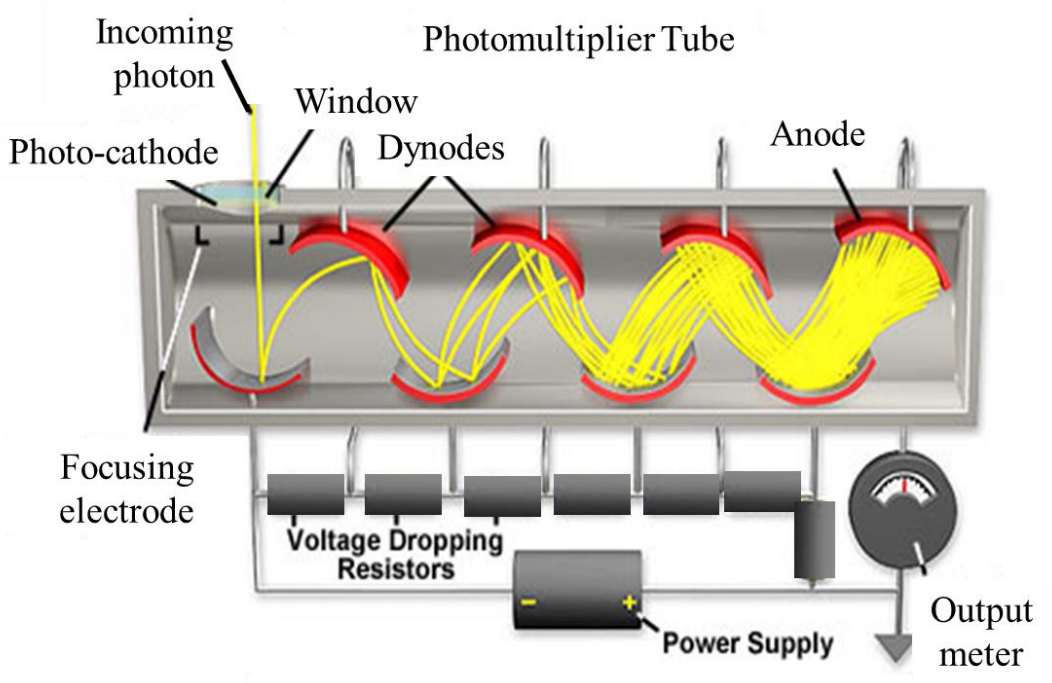

Fig.1 Schematic illustration of photomultiplier tubes. Photo-cathode is used for focusing light onto a chain of dynodes. Figure adapted from ref. [8]

Meticulous alignment and shaping of cathodes, dynode pairs and anode results in a fragile and expensive device. Voltage dropping resistors are used to achieve the potential division for each dynode and the total resistance of the system can be in the range of 10 – 20 MΩ. Typical power supplies required for *PMT* operation are 500 – 3000 V [7]. The photo-cathode determines the quantum efficiency of a *PMT*. The quantum efficiency is a ratio of the generated photoelectrons to incident photons. The peak quantum efficiency of a *PMT* may be less than the quantum efficiency of a single photocathode as in actual *PMT* operation all photoelectrons

ejecting off photocathode may not be collected by the first dynode. Table 1 lists quantum efficiencies and corresponding spectral range for different types of photocathodes [7].

Table 1: comparison of quantum efficiencies of various PMT photocathode materials.

Photocathode material	**Quantum efficiency**	**Wavelength**	**T (K)**
Cs-Te	26%	125 nm	300
Sb-Na-K	30%	260 nm	300
Sb-Na-K-Cs	30%	260 nm	300
GaAs (Cs)	23%	300nm	300
InGaAs (Cs)	2%	1000-1300 nm	300
InP/InGaAs (Cs)	2%	1000-1500 nm	300

Motivations of *PMTs* include wide active area to absorb light, high gain, lower gain fluctuations with typical gain values reaching several millions, lower dark currents and can cover wide spectral range from ultra violet to near infra-red. However their drawbacks include bulky size, high operating voltages and sensitivity to stray magnetic fields [8].

1.1.2 Superconducting Nanowire Single Photon Detectors (SNSPDs)

SNSPDs are a superconducting wires operated at currents slightly below their critical current density. When light is incident, a superconductive hot spot is formed. This leads to the superconducting current flow across the periphery of the hot spot which increases the current density. This leads to the spread of the critical current density quickly across the length of nanowire. Consequently a resistive blocking element is formed across the length of the nanowire which increases the temperature leading to sharp increase in the resistance of nanowire material. This sudden increase in the resistance is read by consequent detection electronics and an arrival of the single photon is sensed.

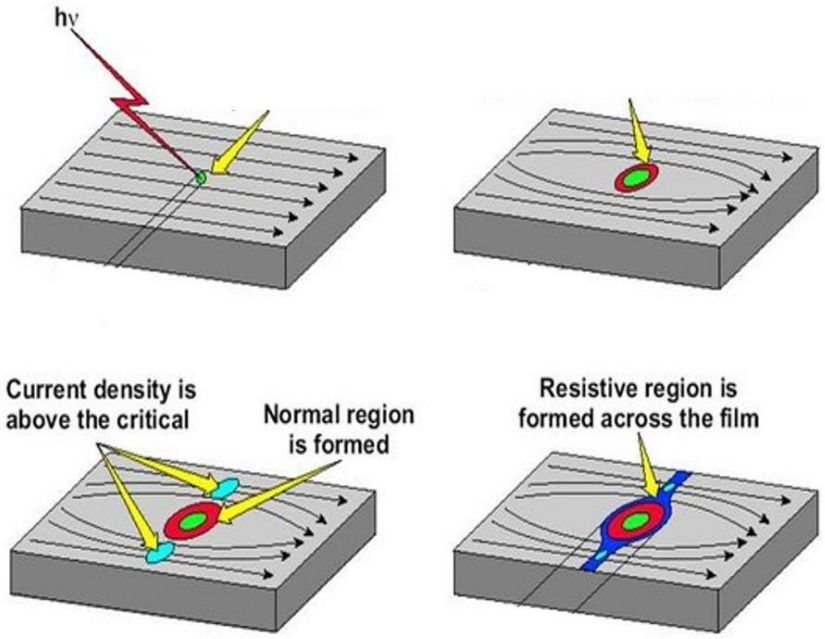

Fig. 2 Schematic illustration of SNSPD. The stepwise process is illustrated showing the increase in the hotspot size and resistance of the sheet as a result of the arrival of the single photon. Figure adapted from ref [8].

The step-wise operation of SNSPD is shown in schematic illustration in Fig. 2. Major advantages of SNSPDs include extremely low dark count rates and very high single photon detection efficiency however they suffer from a number of drawbacks including a bulky size, dependence of liquid helium to reach cryogenic temperatures which limits their use to ground based laboratory applications and are unrealistic for compact and portable applications [9] .

1.1.3 Transition Edge Sensors (TES)

Transition edge sensors are closely related to SNSPDs and are cryogenic particle detectors that us the temperature dependent transition between superconductivity and normal resistance to detect the arrival of single photons. The *TES* is biased through a current source using a load resistor where the power dissipation is kept at a constant level through the *TES.* When a photon is absorbed by the sensor, the resistance increases causing the *TES* current to drop significantly. Subsequent detection electronics can read the transition out and thus single photon detection is achieved.

TES have attractive aspects such as very high quantum efficiency, negligible dark count rates however they strongly depend on cryogenic temperatures and have high timing jitter (time delay between the absorption of incoming photon and generation of an output current pulse corresponding to photo-electron generation). Bolometers also make use of the change in resistance in response to heating of a small area. A carbon resistance bolometer was demonstrated in 1962 by Lalevic [10] compatible with very low RF power levels. *TES* is a superconducting counterpart of the bolometers. Micro-bolometers are used to detect single photons through a change in their resistance as a result of heat dissipation in a tiny area. Fig. 3 shows the schematic of the micro-bolometer. The construction involves an infra-red absorber material, a titanium reflective mirror and a read out circuit. The electrical resistance of the infra-red absorber changes when *IR* radiation is incident. Some incident radiation may get past the absorber in which case the radiation is reflected back using a reflective layer to ensure complete absorption. Micro-bolometers are light weight and can operate at room temperature and are less power hungry compared to cooled detectors. However disadvantages include longer response times and their inability to operate at multispectral and high-speed detection applications and low sensitivity compared to cooled photon detectors.

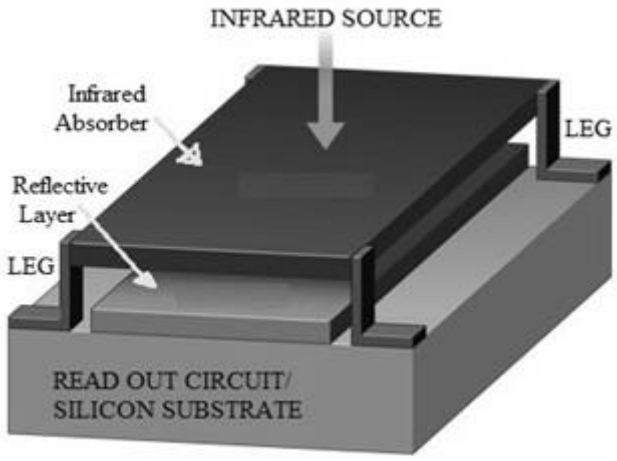

Fig. 3 Schematic of a micro-bolometer. Figure adapted from ref. [11].

1.1.4 Superconducting Quantum Interference Devices (SQUID)

Primarily used as super-sensitive magnetic flux meters, SQUID devices based on thin insulating Josephson junctions formed by sandwiching two superconducting materials have been used to sense single photons. The Josephson junctions in the SQUID are connected to a temperature sensor which measures the increase in the temperature resulting from suppression of Josephson critical current density. This suppression causes a voltage drop across the SQUID device and an AC Josephson effect is subsequently used to sense the voltage drop across the device and a photon arrival is sensed [12]. SQUID-readout based single photon detection systems offer enhanced signal to noise ratio in low temperature ranges (1-4 K) photon count rates up to 20 MHz and low dark counts of down to four in one hour [13]. Schematic of a SQUID Josephson junction is shown in Fig. 4.

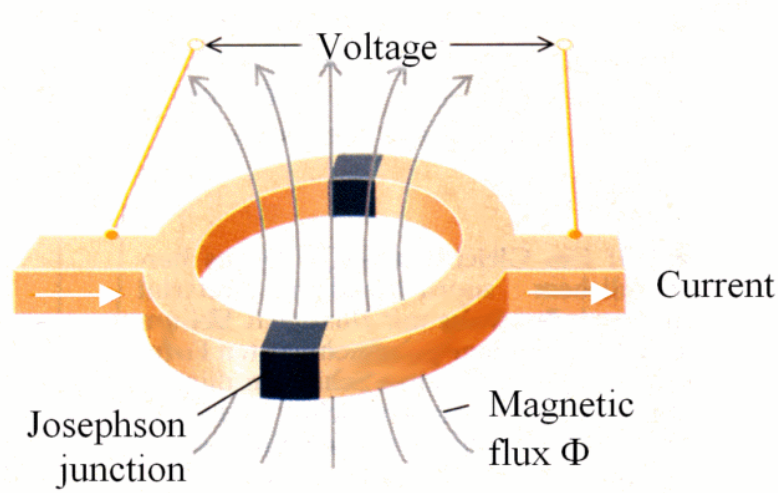

Fig. 4 Thin Josephson junction SQUID device used for sensing the arrival of single photon. Figure adapted from ref [14].

Graphene based Josephson junctions as the material demonstrates excellent single photon calorimetry [15]. Using the absorption properties of graphene, Walsh proposed a superconducting-normal-superconducting Josephson junction where graphene is sandwiched between two superconducting materials. Such a hybrid scheme has been demonstrated to work as a superconducting transistor [16]. The concept involves controlling the super-current through perturbation of the Fermi distribution in the junction through joule heating. In comparison to metals and

semiconductors graphene offers high carrier mobility and thermal response which makes it an attractive candidate for weak links the Josephson junctions. The temperature in the graphene lattice raises as soon as an electron is absorbed. This thermal effect can trigger the Josephson junction to increase its resistance. The heating can described by temperature T_e of electrons in graphene as they thermalise in response to incident radiation. Fig. 5 shows the schematic of the concept used by Walsh.

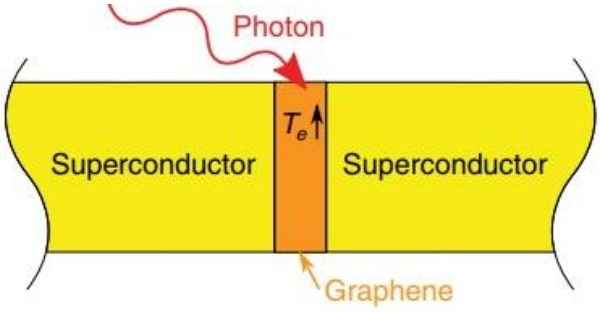

Fig. 5 Schematic of graphene based Josephson junction for single photon counting. Figure adapted from ref. [42]

Practical challenges however include high susceptibility of the Josephson junction based readout system to background/environmental thermal noise, complex construction, a strong dependence on cryogenic liquid helium temperatures and a fast boiling off rate of liquid cryogens. For high sensitivity a large coil size may be needed which may become unrealistic with compact applications [17]. A comparison of various performance parameters of the Josephson junction is given in Table 2.

1.1.5 Semiconductor Single Photon Avalanche Diodes (SPADs)

Semiconductor single photon avalanche didoes are considered as solid state alternative to PMTs based on their ability to detect and amplify extremely weak light signals down to single photon levels. An incoming photon is absorbed the semiconductor material corresponding to a suitable bandgap energy. Under the action of a strong electric field provided by a reverse bias, the photo-generated electrons are excited to overcome the ionisation threshold energy and excite an electron from valence band to conduction band.

The seeded and parent electrons can undergo a further chain of such "impacting" collisions generating more energetic carriers. This process build up into a chain of impact ionisation events thus triggering an avalanche of carriers which subsequently builds up a macroscopic electrical signal in response to the incoming photons. This process is called Impact Ionisation.

Avalanche Photodiodes (APDs) are the commonly used semiconductor single photon detection technology. These devices are made by forming a junction/multiplication layer between two oppositely doped semiconductors. State-of-the-art APDs mostly use planar technology for *p-n* junctions while some use mesa diodes processed using standard wet chemical etching and metallisation. The device layers are normally grown on a substrate material. Fig.6 shows the schematic of an avalanche photodiode. These devices can be illuminated from either top or bottom. Once electron hole pairs are created as a result of photon absorption in an absorber material (narrow bandgap $In_{0.47}Ga_{0.53}As$ is used for 1550 nm detection in linear and Geiger mode APDs), successive electrons and holes are created by impact ionisation process under high electric field (in typically wide bandgap multiplication layers i.e. InP, InAlAs or $Al_{0.85}Ga_{0.15}As_{0.56}Sb_{0.44}$ in this case), amplifying the weak optical signals to strong detectable electronic signals.

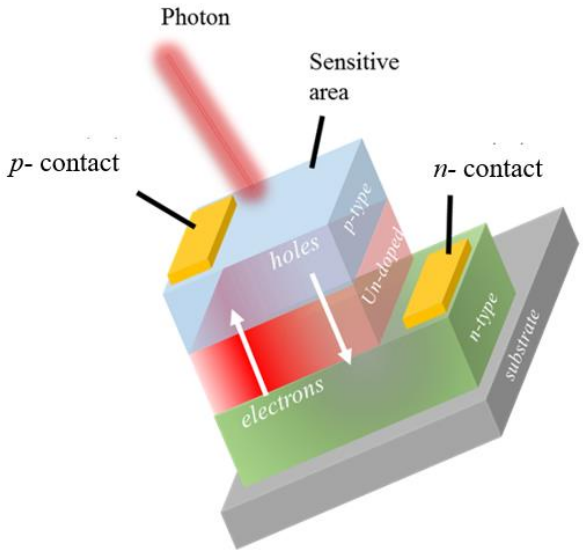

Fig. 6 Schematic illustration of a p-i-n structure semiconductor device grown on a substrate

Such devices provide a robust, cheap and compact alternative to conventional single photon detection technologies described previously. Semiconductor devices using impact ionisation process for light detection are referred to as Avalanche Photodiodes (APD).

State of the art in APD technology has been dominated by Silicon owing to its mature fabrication technology and a high wafer quality resulting in low dark currents and defect densities. However, the recent advances in fibre optic telecommunication applications has pushed the research efforts towards semiconductor photodetectors. In this regards, some of the III-V semiconductor material alloys are important as they provide detection wavelength at 1550 nm which is the preferred wavelength for long-haul fibre optic data communication systems. As shown in the following figure, III-V semiconductor alloy of $In_{0.47}Ga_{0.53}As$ lattice matched to InP substrate can offer detection at 1550 nm.

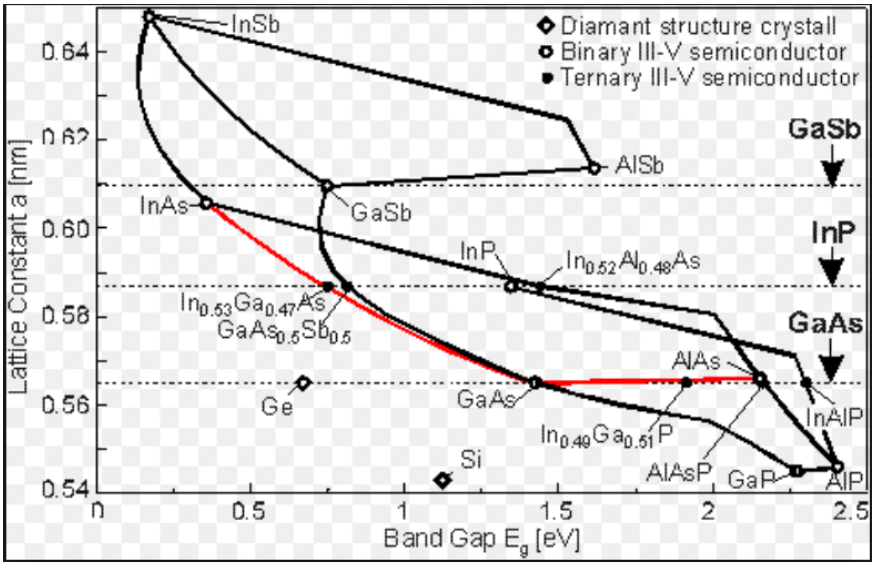

Fig. 7 Lattice constant and bandgap diagram for various ternary and binary alloys. Figure adapted from reference [18]. Red solid line along horizontal direction shows increasing bandgap (GaAs → AlAs) for nominally similar lattice constant whereas the skew direction on the red solid line shows variation in bandgap and lattice constant between GaAs and InAs.

Referring to the dashed line along the lattice constant of 0.588 nm, photon detection at 1550 nm is facilitated by $In_{0.47}Ga_{0.53}As$ absorber material corresponding to the bandgap of 0.75 eV (using the relation $E = \frac{hc}{\lambda}$ where wavelength is in microns). Currently Single Photon Avalanche Diodes (SPADs) based on InP (Negative Feedback Avalanche Diodes, NFADs) and InAlAs avalanche multiplication regions are used for photon sensing in 1550 nm wavelength using $In_{0.47}Ga_{0.53}As$ as absorber layer. A detailed review of semiconductor single photon detection technologies is presented in next section. The possibility of bandgap engineering in these material systems has provided a greater flexibility in application specific detection wavelength. Typical applications that have benefitted greatly from this innovation are

- High bandwidth internet [19]
- Undersea optical fibre networks [20]
- Laser distance mapping [21]
- Quantum Key Distribution (QKD) [22]
- Biomedical imaging [23]
- Autonomous driving technology [24]
- Security applications including
    - Night vision cameras [25]
    - Thermal imaging technology for enhanced security surveillance [26]
    - Imaging applications for harsh and inclement weather and rugged operating conditions in military battlefield and modern warfare applications [27].

Depending on the nature of application, APDs can be operated sub-breakdown mode (linear mode) or above the breakdown voltage (Geiger mode). Typical applications for linear mode include, photodiode mode operation i.e. solar cells and low noise avalanche sensors for optical fibre telecommunication applications [28].

The Geiger mode APD derives its name "Geiger" from the radiation counterpart of APDs i.e. Geiger Müller counter [29] which uses a gas tube filled with inert gases at low pressure and high voltages to generate electrical current in response to radiation flows causing the inert gases to ionise. In Geiger mode, APDs can generate an electrical current signal in response to the absorption of incoming radiation by the bandgap of the semiconductor. Geiger mode APDs are used in application involving detection of ultra-weak light signals down to single photon level and representative applications include Quantum Key Distribution (QKD) [30], Near Infra-Red (NIR) [31] imaging and biomedical imaging technologies [32]. Linear and Geiger mode operation of APDs are dramatically different albeit for similar devices, and therefore it is useful to introduce some performance metrics and consideration for both these modes. In the following section we provide a brief introduction of the major performance metrics of linear and Geiger mode APDs. A comparison of various single photon detection technologies in terms of key performance parameters such as the dark count rate, operating temperature and detection efficiency is shown in Table 2.

Table 2: Comparison of various performance parameters of single photon detection technologies.

Detector type	**T (K)**	**Detection efficiency (%) at wavelength (nm)**	**Dark count rate (Hz)**	**Ref.**
PMT (visible - near infra-red)	300	40 @ 500	100	[33]
Si SPAD (thick)	250	65@650	25	[34]
InGaAs SPAD	200	10@1550	91	[35]
InP NFAD	243	6@1550	28000	[36]
	223	10@1550	600	[37]
	163	11.6@1550	1.2	[38]
SNSPD	3	70@1550	10	[39]
SNSPD (closed cycle cryostat)	0.8	80@400-2500	100	[40]
Transition Edge Sensors	0.1	50@1550	3	[41]
Josephson junctions	0.025	60@1550	1000	[42]
Si SPAD (shallow junction)	250	49@550	25	[43]
PMT-Infrared	200	2@1550	200000	[44]

In summary of Table 2, for InP NFADs, an increase in the operation temperature leads to a higher *DCR* through thermal generation in the narrow bandgap absorber layer which leads to consistently a lower *PDE*. More detailed reviews of single photon detection technologies can be found in ref. [39,45]. Overall, semiconductor single photon detectors provide a compact, cheap and robust alternative to other detection technologies and the following section is dedicated to the review of semiconductor single photon detectors.

1.2 Review of semiconductor single photon detection technology

Despite the best performance of Silicon in visible regions, Si GM-APDs are not suitable for III-V applications in the 1550 nm wavelength due to their poor absorption coefficient in this range. Since the modern optical fibre systems operate at 1550 nm, Si GM-APDs are not compatible in this range. Germanium can be an alternative in this regard as it can

provide detection wavelength up-to 1600 nm at room temperature. Some research efforts have focussed on developing GM-APDs based on Si [46,47]. Ge based GM-APDs however require cryogenic cooling to minimise the *DCR* but the associated trade-off is the inevitable shift of the detection wavelength to 1450 nm which results in a small *PDE* at 1550 nm. Recently progress in research work on Ge has resulted in Ge/Si APDs with good performance however the detectors are capable to operate only in 1310 nm wavelength [48].

Currently InGaAs/InP technologies dominate the market in single photon detection in 1550 nm wavelength region [49,50]. The most common structure of the device used in this technology has evolved over time and was originally conceived for high speed telecommunication [51]. InGaAs/InP based SPAD structures most commonly studied nowadays include a buried p-n junction created through diffusion of Zinc dopants where SiN passivation is used as diffusion mask to define active area. Concentric diffusion rings are created to avoid build of electric field at the outer periphery of the multiplication region. Fig. 8 shows the schematic illustration of the InGaAs/InP Geiger mode APDs.

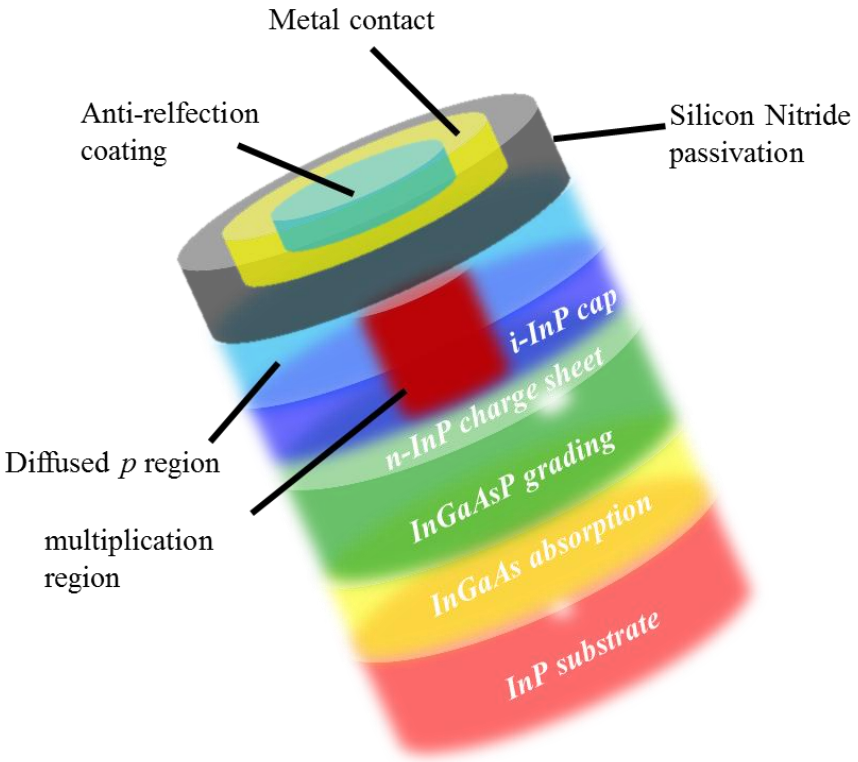

Fig. 8 Schematic of cross section of the device structure of planar InGaAs/InP Geiger mode APDs.

Several research efforts over the last decade have improved the overall performance of these SPADs, of course with some trade-offs. Major performance parameters reviewed in this work are dark count rate (*DCR),* photon detection efficiency (*PDE*) and afterpulsing probability. State of the art Geiger mode APDs based on InP multiplication layer use $In_{0.47}Ga_{0.53}As$ absorber layer lattice matched to InP substrate. Major trade-offs in this research include a higher count rate and an increased afterpulsing probability due to a reduced detector dead time. Therefore, a review of the work given here summarises the efforts done in this regard. A majority of recent work done on InGaAs/InP Geiger mode APDs use a specific configuration called the Negative Feedback Avalanche Diodes (*NFAD*) where the parasitic capacitances were reduced by a surface integrated monolithic resistor used for termination of avalanche (quenching)[52] using the planar structure similar to that of Fig. 6.

Lunghi et al [53] demonstrated a *PDE* of 10% with a *DCR* of 600 Hz at 223 K. This work demonstrated a reduction in the afterpulsing probability and an increase in the detection efficiency by implementing an active hold-off time or the so-called dead time. Further reducing the *DCR* from thermal generation currents, Yan et al [54] recorded a *DCR* of 100 Hz at a *PDE* of 10% by lowering the operation temperature to 193 K with an afterpulsing probability of less than 0.1%. In this regard, Korzh et al [55] demonstrated an even smaller *DCR* of 1 Hz for a free running InP Geiger mode at a *PDE* of 10% at a temperature of 143 K. The afterpulsing probability in this work was recorded at 2.2% with dead times as long as 20 μs. The *DCR* in this work was dominated by thermal generation components and therefore a cooling system called as Free Piston Sterling Cooler was used their work to achieve low temperatures down to 143 K. the reduced afterpulsing in the works of Korzh and Lunghi has been achieved owing to a user defined active hold-off time which can be adjusted in the range of 1-20 μs. Tosi et al [56] reported a *PDE* of 28% at 225 K with a *DCR* of 5 kHz. A negligible afterpulsing was observed by Tosi et al however they used dead times of at least 10 μs. This was the highest ever *PDE* reported for InGaAs/InP SPADs until 2014.

Later, a record high *PDE* of 55% had been demonstrated by Commandar et al [57] at 293 K which remains the highest value reported so far for InGaAs/InP SPADs nonetheless the afterpulsing probability stands at 10.2% for a dead time on the order of 10 ns. Commandar et al observed that the afterpulsing probability increased from 9% to 30% at a *PDE* of 53% when temperature was reduced from 293 K to 273 K.

Currently in III-V single photon detection, a trending research is enhancing the capability of Geiger mode APDs in achieving high count rates. This has been enabled using high frequency gating techniques. At higher repetition frequencies however afterpulsing has been a bottleneck. Improving the material quality to reduce the defect levels in InP is a challenge that is unlikely to be accomplished in near future [58] and the solution to reducing afterpulsing is limiting the charge flow during the avalanche process. In this regard, the so-called high frequency gating has been used to restrict the avalanche charge flow through the Geiger mode APD. Scarcella et al [59] demonstrated a lower afterpulsing probability of 1.5% however at a *PDE* of 30%. Although Scarcella et al operated their detector with a higher gate frequency (1.3 GHz) compared to 1 GHz by Commandar as well as a reduced temperature of 240 K, the reduced afterpulsing could be achieved at lower *PDE* owing to the excess bias dependent nature of afterpulsing. Recently Yu et al [60] have demonstrated a *DCR* of 6.7 kHz with an afterpulsing probability of 13% at 243 K using longer dead times of 600 ns. Yu et al further observed a drop in the *DCR* to 135 Hz by reducing the temperature to 135 K however this was associated with a penalty from an afterpulsing probability of 38%.

High-speed gating technique such as sine wave gating have been used by Lu et al to restrict the charge flow during avalanche using a gating frequency of 80 MHz for an InP Geiger mode APD [61]. For instance, at a detection efficiency of 17%, Lu et al have reduced the dark count rate by an order of magnitude by reducing the pulse duration from 2.5 ns to 1.4 ns. The *DCR* at 10% *PDE* at 240 K was reported to be 8.9 kHz. The reduced dark count in this work had been attributed to a suppression of afterpulsing resulting from a reduced charge flow through avalanche layer which was a factor of 5 smaller than the conventional sine wave gating [62]. Using a 1.25 GHz sine wave gating for an InP Geiger mode APD, Jiang et al [63] obtained an afterpulsing probability of less than 3% at 10% *PDE* at 243 K where a maximum *DCR* of 3.2 kHz was recorded. Recently Chen et al [64] have used a 1 GHz sine wave gating scheme for an InP Geiger mode APD and recorded an afterpulsing probability of 1.3% at 10% *PDE* at 293 K using a dead time of only 1 ns. This work shows a considerable reduction in the dead time in comparison to commercially available 100 MHz single photon detector [65] which demonstrates a 10% *PDE* for a dead time of 10 μs. Table 3 lists a comparison of some high frequency gated InP Geiger mode APDs in terms of important performance parameters such as afterpulsing probability P_a, dark count probability P_d, detection efficiency, dead time and

operating temperature. The scheme as referred to in the table represents the biasing method of SPAD i.e. in a sine wave biasing scheme the SPAD is biased for a limited time above the breakdown, defined by a sine-wave whereas in a free running scheme the SPAD is continuously biased above the breakdown and continues to be biased until an avalanche events is triggered by an incoming photon. Consequently load resistor quenches the avalanche and the SPAD is biased above the breakdown voltage following a recovery (defined by the *RC* time constant of the SPAD capacitance and series resistance).

Table 3. Comparison of different operation schemes for InP GM-APDs in terms of various performance parameters.

Scheme	**T (K)**	***PDE* (%)**	**P_a (%)**	**Gating frequency**	**Dead time**	**Reference**
Sine wave	223	10	11.7	1.25 GHz	0	[66]
Sine wave	233	10.8	2.8	1.5 GHz	50 μs	[67]
Self-differencing	243	9.3	3.4	921 MHz	10 ns	[68]
Self-differencing	293	10	1.7	1 GHz	0	[57]
Negative feedback avalanche diode	163	10	2.2	--	20 μs	[55]
ID-210 free running SPAD (iDQ Geneva)	--	10	--	--	50 μs	[65]
Sine-wave gating	294	10.6	1.3	1 GHz	1 ns	[64]

Recently, $In_{0.48}Al_{0.42}As$ has emerged as an alternative to InP GM-APDs recently owing to the reduced temperature dependence of avalanche breakdown for InAlAs compared to similar thickness of InP. In this context, Meng et al [69] have reported InGaAs/InAlAs SPAD with a *PDE* of 26% at 1550 nm with a *DCR* of 100 MHz at 210 K. In comparison with previous work on InAlAs by Karve et al [70] who reported a similar *DCR* at lower detection efficiency of 19% at 130 K, Meng et al reduced the *DCR* at a similar detection efficiency with no afterpulsing as the operation temperature was higher compared to Karve et al who reported afterpulsing at lower temperatures (50 - 100 K). The reduced *DCR* for Meng et al however was due to a thicker avalanche layer which mitigated the

field assisted *DCR* component resulting from band to band tunnelling. In a previous work by Meng et al [71] excessive band to band tunnelling current was observed in their GM-APD based on InAlAs multiplication layer.

The benefits of using a wide band gap material in this regard are obvious as that could mitigate the tunnelling currents in Geiger mode operation. Wider bandgap is useful as it provides the multiplication layer a higher susceptibility to band-to-band tunnelling currents which are typical to high field operation of a SPAD [31]. In the next section we review recent progress in wide bandgap III-V semiconductor materials with band gap greater than InP and InAlAs.

1.3 Review of wide band gap III-V semiconductor materials

Recently, $AlAs_{0.56}Sb_{0.44}$ lattice matched to InP substrate has emerged as wide bandgap ($E_g = 1.6\ eV$) alternative to InP and InAlAs [72]. $AlAs_{0.56}Sb_{0.44}$ demonstrated a reduced temperature coefficient of avalanche breakdown of 0.95 mV/K for an 80 nm thick avalanche layer. The reduced temperature coefficient of avalanche breakdown for this material was speculated to be (i) the dominance of alloy scattering effect which is temperature independent and (ii) reduced phonon scattering collisions prior to impact ionisation. This was the smallest temperature coefficient of avalanche breakdown compared to the previously reported values of 2.5 mV/K for InAlAs (100 nm thick) and 6 mV/K for InP (130 nm) [73]. A reduced phonon scattering events prior to impact ionisation for thin avalanche layers at high electric field was attributed to the temperature insensitivity of avalanche breakdown for $AlAs_{0.56}Sb_{0.44}$ [74]. A major limitation of $AlAs_{0.56}Sb_{0.44}$ mesa diodes however was the presence of perimeter leakage currents which can induce electric field along the mesa sidewalls and is an undesirable effect for APDs.

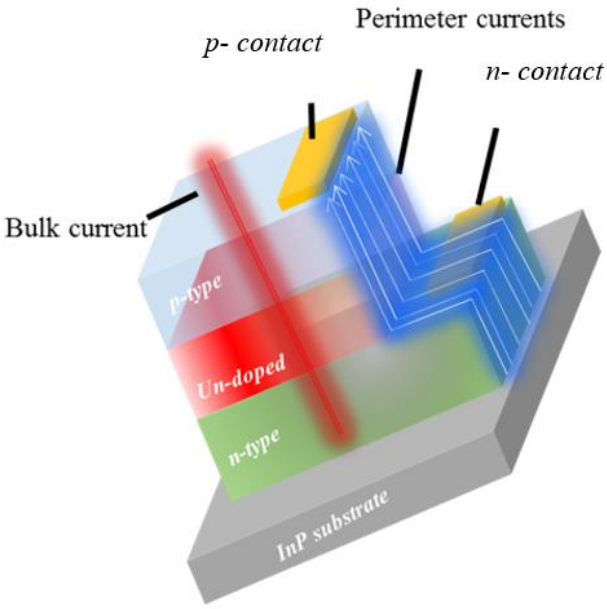

Fig. 9 Schematic illustration of a mesa diode with bulk current (red arrow) through the inner bulk and perimeter leakage current through the sidewalls. The perimeter leakage here is only shown on the right sidewall of mesa for illustration purposes and can flow along the entire perimeter.

Fig. 9 shows schematic illustration of the perimeter leakage currents (blue arrows) simultaneously flowing with bulk current (red arrow) which only flows through the bulk of diode. Perimeter leakage can arise from dangling bonds due to abrupt sidewall termination in mesas. The square shaped mesa in Fig.6 is only shown for the ease of sketch and demonstration and actual mesa devices characterised in this work are circular. Xie et al in their work confirmed the presence of a significant surface leakage currents in their devices. Bozkurt et al [75] have reported on the conduction and valence bands offsets between InP and $AlAs_{0.56}Sb_{0.44}$ with a conduction band and valence band offsets of 1.33 eV and 0.3 eV respectively at 300 K. Zhou and co-workers in their further work [76] on these thin layers incorporated Ga into the ternary alloy in various compositions and observed that addition of Ga significantly suppressed the surface leakage components. The bandgap reduced from 1.6 eV ($Al_xGa_{1-x}As_{0.56}Sb_{0.44,}$ x = 1.00) to 1.56 eV ($Al_xGa_{1-x}As_{0.56}Sb_{0.44,}$ x = 0.85) which corresponded to reduction in breakdown voltage of 64.7 mV per percent Ga. It is known that addition of Ga reduces bandgap of $Al_xGa_{1-x}As_{0.56}Sb_{0.44}$ lattice matched to InP. Reduction of bandgap implies that the carriers will cross the threshold ionisation energies and undergo Impact Ionisation with a relative ease in comparison to a wide bandgap material, and hence a smaller operating voltage would

be required to reach breakdown. Another interesting aspect of $Al_{0.85}Ga_{0.15}As_{0.56}Sb_{0.44}$ is the wide and indirect bandgap which makes it less susceptible to band-to-band tunnelling currents which are typical in InP and InAlAs during Geiger mode operation. Zhou et al confirmed in their work on the breakdown characteristics of $Al_xGa_{1-x}As_{0.56}Sb_{0.44}$ that for $x = 0.15$ the quaternary material did not show significant band-to-band tunnelling which is beneficial for Geiger mode operation of APDs. The lattice mismatch between $Al_{0.85}Ga_{0.15}As_{0.56}Sb_{0.44}$ and InP substrate in the work of Zhou [76] was less than 0.24%.

Mesa diodes based on these layers ($Al_xGa_{1-x}As_{0.56}Sb_{0.44,}$ $x = 0.85$) were subsequently characterised by Zhou and co-workers [77] for temperature dependence of avalanche breakdown. The 100 nm thick quaternary $Al_{0.85}Ga_{0.15}As_{0.56}Sb_{0.44}$ demonstrated a C_{bd} of 0.86 mV/K (in temperature range of 77 – 294 K) which was the lowest among other III-V materials reported to date. The small temperature coefficient of avalanche breakdown in $Al_{0.85}Ga_{0.15}As_{0.56}Sb_{0.44}$ was attributed to a combination of reduced phonon scattering at high fields for thin layer and dominant alloy scattering.

Studies on excess avalanche noise on $Al_{0.85}Ga_{0.15}As_{0.56}Sb_{0.44}$ confirmed lowest excess noise compared to other wide bandgap III-V materials such as InP, InAlAs and $AlAs_{0.56}Sb_{0.44}$ for comparable thickness of avalanche layer [78]. Similarly, studies on temperature coefficient of avalanche breakdown for a nominally 100 nm thick $Al_{0.85}Ga_{0.15}As_{0.56}Sb_{0.44}$ layer in the extended temperature range of 294 – 353 K confirmed a small temperature coefficient of avalanche breakdown of 1.60 mV/K [79]. An investigation of the edge breakdown effect also confirmed that there was no such issue in the mesa diodes based on thin $Al_{0.85}Ga_{0.15}As_{0.56}Sb_{0.44}$ avalanche layers. Recently Pinel et al [28] have reported excess noise studies on a nominally 100 nm thick $Al_{0.85}Ga_{0.15}As_{0.56}Sb_{0.44}$ avalanche layer lattice matched to InP substrate. Using pure carrier injection conditions *n-i-p* and *p-i-n* $Al_{0.85}Ga_{0.15}As_{0.56}Sb_{0.44}$ mesa diodes, a higher electron impact ionisation coefficient has been reported with effective ionisation coefficient ratio *k* was reported in the range 0.08-0.1. This was significantly smaller than those of other III-V avalanche materials such as InP, InAlAs and $AlAs_{0.56}Sb_{0.44}$.

In summary, $Al_{0.85}Ga_{0.15}As_{0.56}Sb_{0.44}$ has the potential of replacing InP and InAlAs as avalanche layers due to its temperature insensitive avalanche breakdown, lower excess noise, a wider bandgap and a higher tolerance to band-to-band tunnelling currents. In the

following section we would like to provide a detailed review of works done on $Al_xGa_{1-x}As_ySb_{1-y}$ (x = 0.1-0.8, y=0.98-0.60) lattice matched to GaSb substrate.

1.4 Review of AlGaAsSb lattice matched to GaSb substrate

Pioneering work on $Al_xGa_{1-x}As_ySb_{1-y}$ layers grown on GaSb substrates (x = 0.2 – 0.5) were carried out by Kagawa and Motosugi [80,81]. $Al_xGa_{1-x}As_ySb_{1-y}$ layers were grown on *n*-doped GaSb (100) substrates where the stoichiometric composition of the quaternary layers ranged from x = 0.2 to 0.8 and y = 0.02 – 0.05. The active layers in most of these studies was several microns thick, typically 2 – 3 µm. The work of Kagawa mostly addressed the dark current analysis and improvement in AlGaAsSb mesa APDs grown on GaSb substrates. In the first work of Kagawa, a maximum avalanche gain of 50 was recorded at 1.3 μm and holes were found to have a higher impact ionisation coefficient than electrons. The second work of Kagawa studied the dependence of diffusion depth inside $Al_xGa_{1-x}As_ySb_{1-y}$ (x =0.2) was studied as a function of temperature and Al composition. A reduction of the dark by one order of magnitude was observed using Zn diffusion in the quaternary alloy.

Law et al studied $Al_{0.43}Ga_{0.57}As_{0.025}Sb_{0.975}$ heterojunction diodes with a nominal thickness of 2-3 μm where an electric field of 160 kV/cm can be inferred from the breakdown voltages specified in the work [82]. In this work Law noted a number of improvements for $Al_xGa_{1-x}As_ySb_{1-y}$ /GaAlSb (x =0.43, y=0.025) heterojunction diodes in comparison with GaAlSb/GaSb diodes. Notable improvements included better surface morphology and 3 times lower dark current density in comparison to the latter diodes. However, the $Al_xGa_{1-x}As_ySb_{1-y}$ /GaAlSb diodes demonstrated an edge breakdown effect. The typical bandgap values for the mentioned quaternary alloys were in the range of 0.7 – 1.2 eV [83]. Subsequent studies by Law and Pilkhun [84 and reference 13 therein] explored the impact ionisation properties of these thick quaternary layers. In this work law studied quaternary $Al_xGa_{1-x}As_ySb_{1-y}$ (x =0.43, y=0.025) alloys grown through liquid phase epitaxy for 1-1.3 μm APD applications. The homo-junction APD exhibited a high gain of 100, a quantum efficiency of 80% however a major problem was still the surface leakage current in the mesa APDs. A higher hole impact ionisation coefficient was reported in this work.

The higher hole impact ionisation coefficient was attributed to the resonance between bandgap and valence band spin orbit split-off band. The phenomenon has been referred to as band resonance by the research community working on these narrow gap Ga rich AlGa(As)Sb alloys. Subsequent works on closely related material such as $Al_{1-x}Ga_xSb$ by Hildebrandt et al [85] and Miura et al [86] for x = 0.065 and 0.947 respectively attributed the enhancement of hole impact ionisation to the spin orbit split off band resonance condition. Hildebrandt demonstrated that ratio of hole to electron impact ionisation increases as the difference between the spin orbit split-off band and bandgap energy decreases. The ratio β/α was found to exceed 20 at 300 K for $Al_{1-x}Ga_xSb$ (x = 0.065). Miura et al in their study demonstrated first ever excess noise measurement for $Al_{1-x}Ga_xSb$ (x = 0.053) and demonstrated an excess noise factor F=3.8 which was 1.2 dB higher than the conventional GaInAs APD at the time. The ratio β/α was demonstrated to be as low as 5 which was the lowest for long wavelength APDs at the time.

Sulima et al [87] reported on improving the dark currents of $Al_xGa_{1-x}As_ySb_{1-y}$ /InGaAsSb/GaSb Separate Absorption and Multiplication APD (SAMAPD) (x = 0.28) by optimising their mesa diode device fabrication using diffused *p-n* junctions in the quaternary layers. Using Zn diffusion, a lower dark current by at least one order of magnitude and a higher breakdown (2 times) was reported for $Al_xGa_{1-x}As_ySb_{1-y}$ (x = 0.28, y=0.014) SAMAPD. The reduction was attributed to the electrical isolation of the defects in the quaternary from the *p-n* junction. Such an isolation was not observed for epitaxial *p-n* junction. A maximum responsivity of 43 A/W was observed at 2100 nm wavelength for a reverse bias of 6.7 V.

Mikhailova and co-workers [88] later reported on low noise InGaAsSb/$Al_xGa_{1-x}As_ySb_{1-y}$ (x=0.33, y=0.014, E_g =1.2 eV) for 1.6-2.4 μm applications. The APD demonstrated a high β/α > 30 and a low excess noise F = 1.6 at M =10. Tuning the bandgap composition of the quaternary, Mikhailova demonstrated an abrupt increase in the hole ionisation coefficient using the band resonance condition described earlier. The resonant composition for this study was x =0.04 for $Al_xGa_{1-x}As_ySb_{1-y}$.

All of the studies referenced hitherto investigated predominantly Ga rich quaternary alloys (composition ~ 70 -99%, E_g : 0.9 – 1.2 eV) for their compatibility with the 1 μm optical window. Recently the interest has shifted to higher wavelength up to 2 μm due to increased interest in extended IR wavelengths. In this regard it is useful to provide some

review of the works done in quaternary $Al_xGa_{1-x}As_ySb_{1-y}$ (x = 0.4 – 0.65) lattice matched to GaSb substrate.

Grzesik et al [89] have characterised the temperature dependence of avalanche breakdown and impact ionisation properties of electrons and holes for three different compositions of $Al_xGa_{1-x}As_ySb_{1-y}$ (x =0.40, y = 0.035), (x = 0.55, y = 0.045), and (x=0. 65, y= 0.054). The ionisation coefficients were extracted form photo-multiplication measurements in temperature range of 77 – 300 K for the three alloys. Grzesik et al reported a higher impact ionisation coefficient for holes than electrons for any temperature. Both electrons and holes impact ionisation coefficients were found to decrease as the Al concentration in the quaternary layer was increased. The values for β/α was reported in the range of 1.2 and 4.0 and was found to depend on temperature, alloy composition and the strength of electric field. The impact ionisation coefficients were reported for 55% alloy composition and the values for ionisation coefficients of electrons and holes at maximum electric field of 400 kV/cm were reported at 2×10^4 cm^{-1} and 2×10^4 cm^{-1} respectively at 300 K. The photo-multiplication measurements in the different temperature ranges were also used to deduce the temperature coefficient of avalanche breakdown. A C_{bd} of 30 mV/K was reported for a 700 nm thick avalanche layer with composition of x =0.55.

Collins et al have recently reported on the field dependence of impact ionisation coefficients for $Al_xGa_{1-x}As_ySb_{1-y}$ (x = 0.90) lattice matched to GaSb substrate [90] in the field range of 150 – 550 kV/cm. The impact ionisation coefficients were extracted using a non-local recurrence model with a variable electric field profile for *p-i-n* and *n-i-p* diodes of difference avalanche layer thicknesses. At maximum electric field, Collins reported a $\beta=\alpha= 1.22\times10^7$ cm^{-1}. Electric field dependence at low field values showed that $\beta>\alpha$ for $Al_xGa_{1-x}As_ySb_{1-y}$ (x = 0.90). The dominance of hole ionisation coefficient was attributed to the band resonance condition between spin orbit split off band and material bandgap (E_g = 2.01 eV at 294 K).

In retrospect, a stark contrast between $Al_{0.85}Ga_{0.15}As_{0.56}Sb_{0.44}$ lattice matched to those lattice matched to GaSb substrate is that the former are thin (100 nm nominal), wide bandgap (1.59 eV at 294 K) and operate at a higher electric field (~1200 kV/cm) while the later are thick (1-4 μm), narrow bandgap (0.7-1.2 eV) and operate at much lower electric fields (55-400 kV/cm). The difference in the impact ionisation coefficients ($\beta>\alpha$ for AlGaAsSb lattice matched to GaSb, $\beta<\alpha$ for AlGaAsSb lattice matched to InP) may

possibly arise from the different alloy composition leading to different bandgaps of these materials.

1.5 Motivation of this work

From the review of the works provided so far, it is now obvious that earlier works on AlGaAsSb quaternary alloys lattice matched to GaSb substrate suffered from either surface leakage or premature edge breakdown effect. In addition to having a wide bandgap, $Al_{0.85}Ga_{0.15}As_{0.56}Sb_{0.44}$ quaternary alloy lattice matched to InP substrate has demonstrated suppressed surface leakage, higher susceptibility to band-to-band tunnelling currents, an absence of premature edge breakdown effect and a reduced temperature coefficient of avalanche breakdown. Such attributes are valuable for linear mode avalanche photodiodes for III-V telecommunication applications. These attributes of $Al_{0.85}Ga_{0.15}As_{0.56}Sb_{0.44}$ motivate me to assess the temporal and temperature stability of avalanche gain in higher temperature ranges previously not covered by any research work. The motivation of assessing the gain stability at higher temperatures (297 K– 353 K) stems from the fact that phonon scattering rates would be higher in comparison with sub-297 K temperature and it would be useful to gain an insight into how the phonon scattering effect competes with alloy scattering in this material. Although this work does not study alloy scattering effect, the temperature coefficient of avalanche breakdown for these temperature ranges can shed light on whether alloy scattering would still be dominant at these high temperatures.

The low temperature coefficient of avalanche breakdown and wide bandgap are also beneficial for Geiger mode applications where a stable *DCR* and higher tolerance to tunnelling currents is needed. Representative examples include fluorescence imaging, long distance mapping and ranging and secure quantum key distribution (*QKD*). The operational complexity of temperature stabilisation circuitry can be circumvented if a material with a temperature insensitive avalanche breakdown is used and from this perspective $Al_{0.85}Ga_{0.15}As_{0.56}Sb_{0.44}$ offers advantage over current InP and InAlAs APDs. In line with this argument, it would be very useful to assess the temporal stability of *DCR* in the Geiger mode without using any temperature stabilisation.

My thesis is dedicated to the fabrication, characterisation and analyses of device performance of APDs based on thin avalanching layers of $Al_{0.85}Ga_{0.15}As_{0.56}Sb_{0.44.}$ I will

also carry out characterisation of the APDs with an aim to achieve Geiger mode device based on thin avalanche layers of $Al_{0.85}Ga_{0.15}As_{0.56}Sb_{0.44}$.

1.6 Organisation of thesis

Chapter 1 introduces various technologies for single photon detection. Benefits and limitations of each technology are listed followed by a motivation for semiconductor single photon detection technology. Basic concepts and performance parameters related to linear and Geiger mode operation of APDs are introduced. A brief introduction to state of the art semiconductor APD technologies for linear an Geiger mode APDs is provided and motivation of $Al_{0.85}Ga_{0.15}As_{0.56}Sb_{0.44}$ is highlighted by comparison with current technology in terms of key performance parameters. A detailed background and review of the semiconductor materials used in state of the art III-V detection technology. A chronological account of research efforts starting with Ga rich narrow bandgap AlGaAsSb materials lattice matched to GaSb substrate leading up to wide bandgap $Al_{0.85}Ga_{0.15}As_{0.56}Sb_{0.44}$ lattice matched to InP substrate is given. A review of InP and InAlAs based semiconductor material systems is provided and a comparison is made with $Al_{0.85}Ga_{0.15}As_{0.56}Sb_{0.44}$ in terms of key parameters. A review of InGaAs/InP and InGaAs/InAlAs Geiger mode APDs is thoroughly conducted with a focus on major performance trade-offs prevalent in the detectors research community.

Chapter 2 provides detailed background theory of the Impact Ionisation, the underlying principle of avalanche photodiodes and single photon detectors. Important concepts related to both the linear and Geiger mode operation of APDs are discussed such as breakdown voltage, avalanche gain, temperature coefficient of avalanche breakdown, Dark Count Rate (*DCR*) afterpulsing and Single Photon Detection Efficiency (*SPDE*).

Chapter 3 details experimental methods used to characterise AlGaAsSb APDs. Important measurement techniques detailed are current-voltage (*I-V*), capacitance-

voltage (*C-V*), photocurrent measurements using Phase Sensitive Detection (*PSD*), gain measurement at elevated temperatures, Dark Count Rate (*DCR*) characterisation as a function of overbias and timing distribution measurement of *DCR* using a Multi-Channel Analyser (*MCA*).

Chapter 4 reports fabrication and characterisation of *p-i-n* $Al_{0.85}Ga_{0.15}As_{0.56}Sb_{0.44}$ APDs. Detailed procedure for various process steps such as photolithography, contact alignment, metal evaporation, wire bonding and packaging and a process flow chart for microfabrication are provided.

Chapter 5 details results on temperature dependence of avalanche breakdown and avalanche gain are provided. Analyses of temporal stability of avalanche gain is provided at different temperature ranging from 294 – 353 K. Temperature stability of gain is compared with commercial Si APDs in the visible and NIR range and analyses of the robustness of the dark currents is provided. A comparison of temporal stability of avalanche gain with $Al_{0.7}In_{0.3}AsSb$ APDs is provided.

Chapter 6 details the characterisation of Geiger mode *p-i-n* $Al_{0.85}Ga_{0.15}As_{0.56}Sb_{0.44}$ APDs. *DCR* characterisation as a function of overbias is done. Influence of the capacitive transient responses on discrimination of weak avalanche signals is discussed. Dependence of *DCR* on pulse repetition frequency and dead time is discussed for investigation of afterpulsing phenomenon. Temporal stability of is reported and a comparison with commercial Si Geiger mode APD is provided. Studies on time distribution of dark and photon counts has been carried out.

Chapter 7 details the modelling of impact ionisation coefficients of thin avalanche layers of $Al_{0.85}Ga_{0.15}As_{0.56}Sb_{0.44}$ using a dead space model and recurrence equations. Using the recurrence equations and the dead space model a parameterised set of field dependent impact ionisation coefficients $\alpha(E)$, $ß(E)$ is provided for pure injection

conditions. The robustness of parameters is checked by fitting the avalanche gain and excess noise data for pure injection conditions with the parameter set derived using recurrence model. Breakdown probability of as a function of overbias is modelled using the similar parameter set, some limitations of the modelling technique are discussed and a detailed discussion on the dark carrier generation rate is provided.

Chapter 8 concludes the work done and suggests future work in light of recent results.

References

[1] A. Olivo, D. Dreossi, “A multilayer edge-on single photon counting silicon microstrip detector for innovative imaging techniques in diagnostic radiology,” *Review of Scientific Instruments*, vol. 74, no. 7, pp. 3460–3465, Jun. 2003.

[2] J. Xu, Zbijewski W, Gang G, Stayman JW, Taguchi K, Lundqvist M, Fredenberg E, Carrino JA, Siewerdsen JH, “Cascaded systems analysis of photon counting detectors,” *Medical Physics*, vol. 41, p. 101907, Oct. 2014.

[3] C. Barbieri, G. Naletto, T. Occhipinti, C. Facchinetti, E. Verroi, E. Giro, A. Di Paola, S. Billotta, P. Zoccarato, P. Bolli, F. Tamburini, G. Bonanno, M. D'Onofrio, S. Marchi, G. Anzolin, I. Capraro, F. Messina, M. Belluso, C. Pernechele, M. Zaccariotto, L. Zampieri, V. Da Deppo, S. Fornasier & F. Pedichini (2009), AquEYE, a single photon counting photometer for astronomy, *Journal of Modern Optics*, 56:2-3, 261-272, DOI: 10.1080/09500340802450565

[4] X. Michalet, R. A. Colyer, G. Scalia, A. Ingargiola, R. Lin, J. E. Millaud, S. Weiss, Oswald H. W. Siegmund, Anton S. Tremsin, John V. Vallerga, A. Cheng, M. Levi, D. Aharoni, K. Arisaka, F. Villa, F. Guerrieri, F. Panzeri, I. Rech, A. Gulinatti, F. Zappa, M. Ghioni, S. Cova, Phil. Trans. R. Soc. B 2013 368 20120035; DOI: 10.1098/rstb.2012.0035. Published 24 December 2012

[5] N. G. Cooper, *The Human Genome Project: Deciphering the Blueprint of Heredity*.

University Science Books, 1994. Google-Books-ID: A5Adp4NPj7wC

[6] M. B. Das, S. Bose, and R. Bhattacharya, “Single photon response of photomultiplier tubes,” *Nuclear Instruments and Methods in Physics Research Section A: Accelerators, Spectrometers, Detectors and Associated Equipment*, vol. 242, no. 1, pp. 156–159, Dec. 1985.

[7] Hamamatsu, ‘PMT Handbook’, 2006. [Online]. Available: http://www.hamamatsu.com/eu/en/support/lib/index.html

[8] Department of Biophysics, Max Planck Institute of Biophysical Chemistry, https://www.mpibpc.mpg.de/637633/projects?page=3

[9] L. You, J. Quan, Y. Wang, Y. Ma, X. Yang, Y. Liu, H. Li, J. Li, J. Wang, J. Liang, Z. Wang, and X. Xie, "Superconducting nanowire single photon detection system for space applications," *Opt. Express* 26, 2965-2971 (2018).

[10] B. Lalevic, Review of Scientific Instruments 33, 103, (1962); https://doi.org/10.1063/1.1717628

[11] http://www.rfwireless-world.com/Terminology/Advantages-and-Disadvantages-of-Microbolometer.html

[12] P. Solinas, F. Giazotto, and G. P. Pepe, “Proximity SQUID single photon detector via temperature-to-voltage conversion,” *arXiv:1711.10846 [cond-mat]*, Nov. 2017.

[13] A. Kirste, "SQUID-Readout for the Superconducting Nanowire Single-Photon Detector," in *IEEE Transactions on Applied Superconductivity*, vol. 19, no. 3, pp. 313-317, June 2009.

[14] Department of Phycis, San Jose State University, http://www.sjsu.edu/people/raymond.kwok/courses/physics/phys120s-lab/squid/

[15] K. C. Fong and K. C. Schwab, Ultrasensitive and Wide Bandwidth Thermal Measurements of Graphene at Low Temperatures, Phys. Rev. X 2, 031006, 2012.

[16] F. K. Wilhelm, G. Schön, and A. D. Zaikin, Mesoscopic Superconducting–Normal Metal–Superconducting Transistor, Phys. Rev. Lett. 81, 1682, 1998.

[17] R. Fagalay, Technical note, “SQUID Instruments and applications”, Tristen Technologies, San Diego, November 2005.

[18] http://www.iue.tuwien.ac.at/phd/brech/ch_2.htm

[19] A. N. Z. Abidin, W. R. W. Abdullah, A. Ramli, and M. Z. M. Jenu, “Interference limit proposal for ADSL2+ using APD methodology,” in *2010 IEEE Asia-Pacific Conference on Applied Electromagnetics (APACE)*, 2010, pp. 1–4.

[20] S. Tang, Y. Dong, and X. Zhang, “Receiver design for underwater wireless optical communication link based on APD,” in *7th International Conference on Communications and Networking in China*, 2012, pp. 301–305.

[21] “The Importance of Avalanche Photodiode (APD) for LIDAR Applications,” *AZoSensors.com*, 07-Sep-2017. [Online]. Available: https://www.azosensors.com/article.aspx?ArticleID=864

[22] Z. L. Yuan, A. R. Dixon, J. F. Dynes, A. W. Sharpe, and A. J. Shields, “Practical gigahertz quantum key distribution based on avalanche photodiodes,” *New J. Phys.*, vol. 11, no. 4, p. 045019, 2009.

[23] I. Britvitch, I. Johnson, D. Renker, A. Stoykov, and E. Lorenz, “Characterisation of Geiger-mode avalanche photodiodes for medical imaging applications,” *Nuclear Instruments and Methods in Physics Research Section A: Accelerators, Spectrometers, Detectors and Associated Equipment*, vol. 571, no. 1, pp. 308–311, Feb. 2007.

[24] G. M. Williams, “Optimization of eyesafe avalanche photodiode lidar for automobile safety and autonomous navigation systems,” *OE, OPEGAR*, vol. 56, no. 3, p. 031224, Mar. 2017.

[25] M. Sonka, V. Hlavac, and R. Boyle, *Image Processing, Analysis, and Machine Vision*. Cengage Learning, 2014.

[26] A. Singh, R. Pal., "Infrared Avalanche Photodiode Photodetectors", Defence Science Journal, Vol. 67, No. 2, March 2017, pp. 159-168, DOI : 10.14429/dsj.67.11183

[27] E. J. Lerner, "Inotrduction to Photodectors and Applications", Laser Focus World, January, 2010,

[28] L. L.G. Pinel, S. J. Dimler, X. Zhou, S. Abdullah, S. Zhang, C.H. Tan, and J. S. Ng, "Effects of carrier injection profile on low noise thin Al_{085} Ga_{015} As_{056} Sb_{044} avalanche photodiodes," *Optics Express*, vol. 26, no. 3, p. 3568, Feb. 2018.

[29] https://en.wikipedia.org/wiki/Geiger%E2%80%93M%C3%BCller_tube

[30] G.S. Buller ; R.E. Warburton ; S. Pellegrini ; J.S. Ng ; J.P.R. David ; L.J.J. Tan ; A.B. Krysa ; S. Cova, "Single-photon avalanche diode detectors for quantum key distribution," *IET Optoelectronics*, vol. 1, no. 6, pp. 249–254, Dec. 2007.

[31] A. Tosi, A. D. Mora, F. Zappa, and S. Cova, "Germanium and InGaAs/InP SPADs for single-photon detection in the near-infrared," in *Advanced Photon Counting Techniques II*, 2007, vol. 6771, p. 67710P.

[32] B. Heshmat, G. Gariepy, J. Leach, R. Raskar, and D. Faccio, "SPAD cameras for biomedical imaging: Promise and problems," in *2016 Conference on Lasers and Electro-Optics (CLEO)*, 2016, pp. 1–2.

[33] See http://jp.hamamatsu.com/resources/products/etd/pdf/m-h7422e.pdf (2010) PMT commercially packaged photon-counting module including voltage bias electronics and thermoelectric cooling

[34] http://excelitas.com/ProductPages/Single_Photon_Counting_ Modules_SPCM.aspx

[35] C. Gobby, Z.L. Yuan, A.J. Shields, "Quantum key distribution over 122 km of standard telecom fiber: Applied Physics Letters: Vol 84, No 19." [Online]. Available: https://aip.scitation.org/doi/10.1063/1.1738173. [Accessed: 11-Sep-2018].

[36] P. Lightwave (2010), see http://www.princetonlightwave.com/content/ PNA-20XNFADDatasheet_rv2.pdf

[37] T. Lunghi, C. Barreiro, O. Guinnard, R. Houlmann, X. Jiang, M. A. Itzler, H. Zbinden, "Free Running Single Photon Detection based on a negative feedback InGaAs APD," *Journal of Modern Optics*, vol. 59, no. 17, pp. 1481–1488, Oct. 2012.

[38] B. Korzh, T. Lunghi, K. Kuzmenko, G. Boso, and H. Zbinden, “Afterpulsing studies of low noise InGaAs/InP single-photon negative feedback avalanche diodes,” *arXiv:1411.0653 [physics]*, Nov. 2014.

[39] M. D. Eisaman, J. Fan, A. Migdall, and S. V. Polyakov, “Invited Review Article: Single-photon sources and detectors,” *Review of Scientific Instruments*, vol. 82, no. 7, p. 071101, Jul. 2011.

[40] ID-281, Superconducting Nanowire Single Photon Detector, iDQuantique, 2018.

[41] D. Rosenberg, J. W. Harrington, P. R. Rice, P. A. Hiskett, C. G. Peterson, R. J. Hughes, A. E. Lita, S. W. Nam, and J. E. Nordholt, “Long-distance decoy-state quantum key distribution in optical fiber”, Phys. Rev. Lett. 98, 010503 (2007).

[42] E. D. Walsh, D. K. Efetov, M. Heuck, J. Grossno, T. Ohki, P. Kim, D. Englund, C. Fong, “Graphene-based Josephson junction single photon detector,” *Physical Review Applied*, vol. 8, no. 2, Aug. 2017.

[43] http://www.microphotondevices.com/products_pdm.asp.

[44] http://jp.hamamatsu.com/resources/products/etd/pdf/NIR-PMT_APPLI_ TPMO1040E02.pdf.

[45] R. Hadfield, “Single-photon detectors for optical quantum information applications | Nature Photonics.” [Online]. Available: https://www.nature.com/articles/nphoton.2009.230. [Accessed: 11-Sep-2018].

[46] B. F. Levine and C. G. Bethea, "Single photon detection at 1.3 μm using a gated avalanche photodiode," *Applied Physics Letters*, vol. 44, pp. 553-555, 1984.

[47] W. Haecker, O. Groezinger, and M. H. Pilkuhn, "Infrared Photon Counting by Ge Avalanche Diodes," *Applied Physics Letters*, vol. 19, pp. 113-115, 1971.

[48] R. E. Warburton, G. Intermite, M. Myronov, P. Allred, D. R. Leadley, K. Gallacher, *et al.*, "Ge-on-Si Single-Photon Avalanche Diode Detectors: Design, Modeling, Fabrication, and Characterization at Wavelengths 1310 and 1550 nm," *Electron Devices, IEEE Transactions on*, vol. 60, pp. 3807-3813, 2013.

[49] “Micro Photon Devices - SPAD by Technology.” [Online]. Available: http://www.micro-photon-devices.com/Products/SPAD-by-Technology. [Accessed: 31-Jul-2018].

[50] Near Infra-Red single photon detectors, “Photon Counting Resource Centre from IDQ,” *ID Quantique.*, IDQ SA, Geneva.

[51] J. C. Campbell, A. G. Dentai, W. S. Holden, and B. L. Kasper, “High-speed InP/InGaAsP/InGaAs avalanche photodiodes,” in *1983 International Electron Devices Meeting*, 1983, vol. 29, pp. 464–467.

[52] X. Jiang, M. A. Itzler, B. Nyman, and K. Slomkowski, “Negative feedback avalanche diodes for near-infrared single-photon detection,” in *Advanced Photon Counting Techniques III*, 2009, vol. 7320, p. 732011.

[53] T. Lunghi, C. Barreiro, O. Guinnard, R. Houlmann, X. Jiang, M. A. Itzler, H. Zbinden, “Free Running Single Photon Detection based on a negative feedback InGaAs APD,” *Journal of Modern Optics*, vol. 59, no. 17, pp. 1481–1488, Oct. 2012.

[54] Z. Yan, D. R. Hamel, A. K. Heinrichs, X. Jiang, M. A. Itzler, and T. Jennewein, “An ultra-low noise telecom wavelength free running single photon detector using negative feedback avalanche diode,” *Rev Sci Instrum*, vol. 83, no. 7, p. 073105, Jul. 2012.

[55] B. Korzh, T. Lunghi, K. Kuzmenko, G. Boso, and H. Zbinden, “Afterpulsing studies of low noise InGaAs/InP single-photon negative feedback avalanche diodes,” *arXiv:1411.0653 [physics]*, Nov. 2014.

[56] A. Tosi, N. Calandri, M. Sanzaro, and F. Acerbi, “Low-Noise, Low-Jitter, High Detection Efficiency InGaAs/InP Single-Photon Avalanche Diode,” *IEEE Journal of Selected Topics in Quantum Electronics*, vol. 20, no. 6, pp. 192–197, Nov. 2014.

[57] L. C. Comandar, B. Frohlich, J. F. Dynes, A. W. Sharpe, M. Lucmarini, Z. L. Yuan, R.V. Penty, A. J. Shields, “Gigahertz-gated InGaAs/InP single-photon detector with detection efficiency exceeding 55% at 1550 nm,” *Journal of Applied Physics*, vol. 117, no. 8, p. 083109, Feb. 2015.

[58] M. A. Itzler *et al.*, “Advances in InGaAsP-based avalanche diode single photon detectors,” *Journal of Modern Optics*, vol. 58, no. 3–4, pp. 174–200, Feb. 2011.

[59] C. Scarcella, G. Boso, A. Ruggeri, and A. Tosi, “InGaAs/InP Single-Photon Detector Gated at 1.3 GHz With 1.5 % Afterpulsing,” *IEEE Journal of Selected Topics in Quantum Electronics*, vol. 21, no. 3, pp. 17–22, May 2015.

[60] C. Yu, M. Shangguan, H. Xia, J. Zhang, X. Dou, and J.-W. Pan, “Fully integrated free-running InGaAs/InP single-photon detector for accurate lidar applications,” *Optics Express*, vol. 25, no. 13, p. 14611, Jun. 2017.

[61] Z. Lu, W. Sun, Q.Zhou, J. Campbell, X. Jiang, and Mark A. Itzler, "Improved sinusoidal gating with balanced InGaAs/InP Single Photon Avalanche Diodes," Opt. Express 21, 16716-16721, 2013

[62] Y. Nambu, S. Takahashi, K. Yoshino, A. Tanaka, M. Fujiwara, M. Sasaki, A. Tajima, S. Yorozu, and A. Tomita, "Efficient and low-noise single-photon avalanche photodiode for 1.244-GHz clocked quantum key distribution," Opt. Express 19(21), 20531–20541 (2011).

[63] W. Jiang, J. Liu, Y. Liu, G. Jin, J. Zhang, and J. Pan, "1.25 GHz sine wave gating InGaAs/InP single-photon detector with a monolithically integrated readout circuit," Opt. Lett. 42, 5090-5093 (2017).

[64] H. Chen, M. Jiang, S. Sun, G. Tang, and L. Liang, "Room temperature continuous frequency tuning InGaAs/InP single-photon detector," *AIP Advances*, vol. 8, no. 7, p. 075106, Jul. 2018.

[65] https://marketing.idquantique.com/acton/attachment/11868/f-0239/1/-/-/-/-/ID210_Brochure.pdf

[66] X. Liang, J. Liu, Q. Wang, D. Du, J. Ma, G. Jin, Z.-B. Chen, J. Zhang, and J.-W. Pan, Rev. Sci. Instrum. 83, 083111 (2012)

[67] N. Namekata, S. Adachi, and S. Inoue, Opt. Express 17, 6275 (2009)

[68] J. Zhang, R. Thew, C. Barreiro, and H. Zbinden, Appl. Phys. Lett. 95, 091103 (2009)

[69] X. Meng, S. Xie, X. Zhou, N. Calandri, M. Sanzaro, A. Tosi, C.H. Tan, J.S.Ng, (2016). InGaAs/InAlAs single photon avalanche diode for 1550 nm photons. *Royal Society Open Science*, *3*(3), 150584. http://doi.org/10.1098/rsos.150584.

[70] G. Karve, X. Zheng, X. Zhang, X. Li, N. Li, N. Wang, F. Ma, J. C. Campbell, A. Holmes, J. C. Campbell, G. S. Kinsey, J. C. Boisvert, T. D. Isshiki, R. Sudharsanam, D. S. Bethune, and W. P. Risk, "Geiger mode operation of an In0.53Ga0.47As-In0.52Al0.48As avalanche photodiode," *Quantum Electronics, IEEE Journal of*, vol. 39, pp. 1281–1286, Nov. 2003.

[71] X. Meng, C. H. Tan, S. Dimler, J. P. R. David, and J. S. Ng, "1550 nm InGaAs/InAlAs single photon avalanche diode at room temperature," *Opt. Express, OE*, vol. 22, no. 19, pp. 22608–22615, Sep. 2014.

[72] S. Xie and C. H. Tan, "AlAsSb Avalanche Photodiodes With a Sub-mV/K Temperature Coefficient of Breakdown Voltage," *IEEE Journal of Quantum Electronics*, vol. 47, no. 11, pp. 1391-1395, Nov. 2011.

[73] L. J. J. Tan, D. S. G. Ong., J. S. Ng., C. H. Tan, S. K. Jones, Y. Quan, J. P. R. David, "Temperature Dependence of Avalanche Breakdown in InP and InAlAs," *IEEE Journal of Quantum Electronics*, vol. 46, no. 8, pp. 1153–1157, Aug. 2010.

[74] D. S. Ong, K. F. Li, S. A. Plimmer, G. J. Rees, J. P. R. David, and P. N. Robson, "Full band Monte Carlo modeling of impact ionization, avalanche multiplication, and noise in submicron GaAs p-i-n diodes," *Journal of Applied Physics*, 87, 7885, 2000.

[75] M. Bozkurt, J. M. Ulloa, and P. M. Koenraad, "An atomic scale study on the effect of Sb during capping of MBE grown III–V semiconductor QDs," *Semicond. Sci. Technol.*, vol. 26, no. 6, p. 064007, 2011.

[76] X. Zhou, S. Zhang, J. P. R. David, J. S. Ng, and C. H. Tan, "Avalanche Breakdown Characteristics of Al1 #x2013;xGaxAs0.56Sb0.44 Quaternary Alloys," *IEEE Photonics Technology Letters*, vol. 28, no. 22, pp. 2495–2498, Nov. 2016.

[77] X. Zhou, C.H. Tan, S. Zhang, M. Moreno, S. Xie, S. Abdullah& J.S. Ng (2017). Thin $Al_{1-x}Ga_xAs_{0.56}Sb_{0.44}$ diodes with extremely weak temperature dependence of avalanche breakdown. *Royal Society Open Science*, *4*(5), 170071. http://doi.org/10.1098/rsos.170071

[78] L. L.G. Pinel, S. J. Dimler, X. Zhou, S. Abdullah, S. Zhang, C.H. Tan, and J. S. Ng, "Effects of carrier injection profile on low noise thin Al_{085} Ga_{015} As_{056} Sb_{044} avalanche photodiodes," *Optics Express*, vol. 26, no. 3, p. 3568, Feb. 2018.

[79] S. Abdullah, C. H. Tan, X. Zhou, S.Zhang, L. Pinel, and J. S. Ng, "Investigation of temperature and temporal stability of AlGaAsSb avalanche photodiodes," Opt. Express 25, 33610-33616 (2017)

[80] T. Kagawa and G. Motosugi, "AlGaAsSb Avalanche Photodiodes for 1.0–1.3-μm Wavelength Region," *Jpn. J. Appl. Phys.*, vol. 18, no. 12, p. 2317, Dec. 1979.

[81] T. Kagawa and G. Motosugi, "Zn Diffusion into AlGaAsSb and Its Application to APD's," *Jpn. J. Appl. Phys.*, vol. 20, no. 3, p. 597, Mar. 1981.

[82] H. Law, K. Nakano, and L. Tomasetta, "III-V alloy heterostructure high speed avalanche photodiodes," *IEEE Journal of Quantum Electronics*, vol. 15, no. 7, pp. 549–558, Jul. 1979.

[83] M. Guden and J. Piprek, “Material parameters of quaternary III–V semiconductors for multilayer mirrors at 1.55 μm wavelength,” p. 9., Model. Simul. Mater. Sci. Eng., 4(4), 349-357, May.1996

[84] H. Law, R. Chin, K. Nakano, and R. Milano, “The GaAlAsSb quaternary and GaAlSb ternary alloys and their application to infrared detectors,” *IEEE Journal of Quantum Electronics*, vol. 17, no. 2, pp. 275–283, Feb. 1981.

[85] O. Hildebrand, W. Kuebart, and M. H. Pilkuhn, “Resonant enhancement of impact in Ga1−xAlxSb,” *Appl. Phys. Lett.*, vol. 37, no. 9, pp. 801–803, Nov. 1980.

[86] S. Miura, T. Mikawa, H. Kuwatsuka, N. Yasuoka, T. Tanahashi, and O. Wada, “AlGaSb avalanche photodiode exhibiting a very low excess noise factor,” *Appl. Phys. Lett.*, vol. 54, no. 24, pp. 2422–2423, Jun. 1989.

[87] O. V. Sulima, M. G. Mauk, Z. A. Shellenbarger, J.A. Cox, J. V. Li, P. E. Sims, S. Datta, S. B. Rafol, “Uncooled low-voltage AlGaAsSb/InGaAsSb/GaSb avalanche photodetectors,” *IEE Proceedings - Optoelectronics*, vol. 151, no. 1, pp. 1–5, Feb. 2004.

[88] M. P. Mikhailova, I. A. Andreev, E. V. Kunitsyna, and Y. P. Yakovlev, “Sensitivity of a receiver using GaInAsSb/AlGaAsSb SAM avalanche photodiode for long-wavelength optical communication systems in the mid-infrared spectral range,” in *Photon Counting Applications, Quantum Optics, and Quantum Information Transfer and Processing II*, 2009, vol. 7355, p. 735511.

[89] M. Grzesik, J. Donnelly, E. Duerr, M. Manfra, M. Diagne, R. Bailey, G. Turner, *and* W. Goodhue, “Impact ionization in AlxGa1−xAsySb1−y avalanche photodiodes,” *Appl. Phys. Lett.*, vol. 104, no. 16, p. 162103, Apr. 2014.

[90] X. Collins, A. P. Craig, T. Roblin, and A. R. J. Marshall, “Impact ionisation in Al0.9Ga0.1As0.08Sb0.92 for Sb-based avalanche photodiodes,” *Appl. Phys. Lett.*, vol. 112, no. 2, p. 021103, Jan. 2018.

Chapter 2

Background Theory

2.1 Introduction

Impact Ionisation is one of the elastic scattering processes where momentum and energy are conserved and is the underlying principle of semiconductor single photon detectors. State of the art semiconductor photon detectors consist of a photon absorption layer where carries are either generated using incoming photons or through thermal generation in the absorbing layer. The carriers are subsequently transferred to a high field wide bandgap multiplication layer under the action of a steady electric field. Once the photo-generated/thermal carriers reach the high field multiplication region, they undergo several collisions with lattice between their mean free paths under the presence of a high electric field which imparts enough kinetic energy to the carriers. Enroute their trajectory, the photo-generated carriers excite electrons from valence band to conduction band. A creation of electron in conduction band means a hole in the valence band. Such a collision is referred to as Impact Ionisation. Subsequent carriers generated through successive Impact Ionisation events can setup a chain of ionisation events.

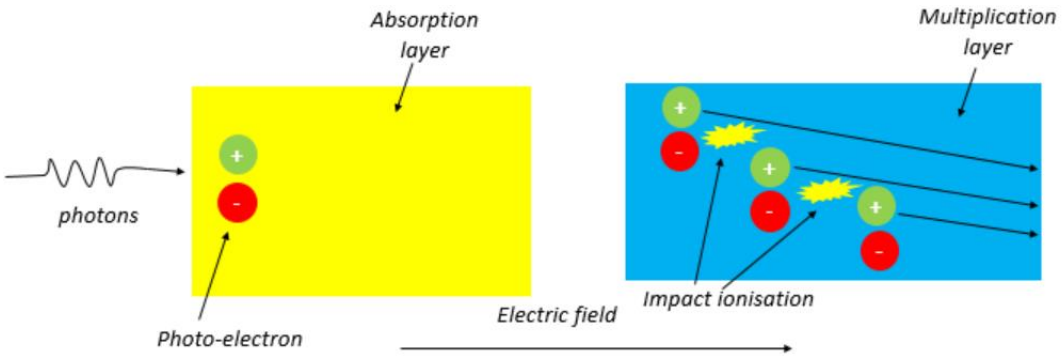

Fig. 1 Schematic illustration of Impact Ionisation process. Photo-generated carriers (electrons indicated as red and holes indicated green circles) created in absorption region (yellow) are accelerated to a high field multiplication region (blue) under the action of a steady electric field. Carriers can impact ionise under high electric field in the multiplication layer creating a strong electrical signal.

Fig. 1 shows a schematic of this process where photo-generated carriers are transferred to a high field region where they undergo successive ionisation. One implication of the ionisation process in high field region is that a strong electrical signal is generated in response to a weak electronic signal. This principle is used to enable the detection of photon radiation and is used in several interesting applications including light detection and ranging, laser distance mapping, fluorescence imaging, quantum key distribution and night vision cameras.

2.2 Impact ionisation and breakdown voltage

In this section, an explanation of the Impact Ionisation process is aided with a bandgap diagram where conduction and valence bands are shown. A pure electron induced impact ionisation is sketched in Fig. 2.

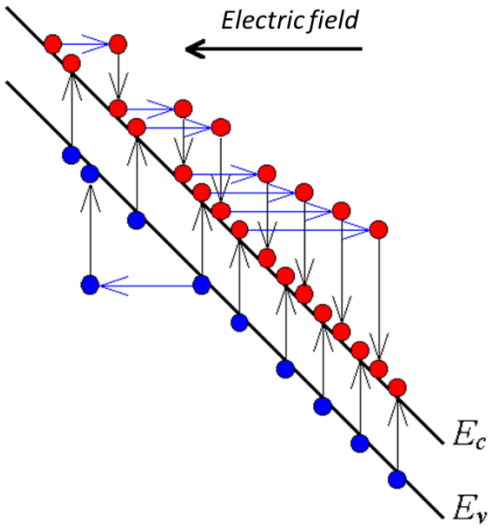

Fig.2. Schematic illustration of pure electron induced impact ionisation. After an electron gains excess energy from the electric field, it travels an average distance before undergoing another collision and generating further electron hole pairs. Red circles show electrons whereas blue are holes. Thin blue arrows show electron impact ionisation events.

The impact ionisation rates of electrons and holes are usually expressed as the Impact Ionisation coefficients α and β respectively. These coefficients define the number of electrons and holes created by a single carrier per unit distance travelled between two impact ionising collisions. Impact ionisation coefficient for electrons, α and holes β can be expressed as [1],

$$\alpha = \frac{1}{n_e v_e} g_e, \tag{1.a}$$

$$\beta = \frac{1}{n_h v_h} g_h, \tag{1.b}$$

Here n_e, v_n, g_e, n_h, v_h, g_h describe electron concentration, electron velocity, electron generation rate in /s, hole concentration hole velocity and hole generation rate in /s respectively. Since the carrier velocity and generation rate are a function of electric field, Impact Ionisation coefficients α and β depend on electric field as well. Considering that excess electron-hole pairs have enough energy, the impact ionisation process can quickly build up to a chain of cascaded avalanche events leading to an avalanche multiplication. The minimum energy needed by the carrier to trigger an impact ionisation event is called as threshold energy denoted by $E_{th.}$ To conserve the energy and momentum of the impact ionising carries, the threshold energies of the carries are larger than the bandgap energy. The impact ionisation coefficients are simply the average number of electron and hole pairs created by the primary carriers per unit distance travelled in the medium. Impact ionisation coefficients depend on material and increase with increasing electric field and reducing temperature.

Impact ionisation coefficients for electrons and holes as a function of electric field are expressed as,

$$\alpha(E) = A_e \exp\left(-\left(\frac{B_e}{E}\right)^{C_e}\right) \tag{2}$$

$$\beta(E) = A_h \exp\left(-\left(\frac{B_h}{E}\right)^{C_h}\right) \tag{3}$$

Where A, B and C are constants that depend on material and E is the electric field. Increasing the electric field increases the number of carrier generated per unit length as the carrier gain more energy from the electric field for impact ionisation. However there are scattering mechanisms in the semiconductor which tend to reduce the impact ionisation coefficients. A major scattering phenomenon is referred to as phonon scattering. Phonon scattering arises from lattice vibration and increases with increasing temperature. Phonon scattering is quantified by phonon occupation number, n_{ph} which is a function of the phonon energy E_p and temperature T and is expressed as [3],

$$n_{ph} = \frac{1}{\exp(\frac{E_p}{k_b T} - 1)} \quad (4)$$

Where k_b is the Boltzmann's constant. As the temperature is increased the phonon scattering is increased which leads to a reduction of impact ionisation for both electrons and holes. This necessitates a higher electric field for the carriers to overcome the cooling effect induced by phonon scattering through loss of energy. Consequently the breakdown voltage increases. The increase in the breakdown voltage as a function of temperature is characterised by the temperature coefficient of breakdown voltage C_{bd} and is expressed as,

$$C_{bd} = \frac{dV_b}{dT} \quad (5)$$

Where V_b is the breakdown voltage. Semiconductor materials with a low temperature coefficient of avalanche breakdown are preferred as they offer immunity to temperature fluctuations.

2.3 Avalanche gain

The process of impact ionisation in avalanche photodiodes results in avalanche gain if the excess carries gain sufficient energy from electric field. The avalanche gain is denoted by *M* and depends on the ionisation coefficients (Eq. 2-3). If the electric field inside the avalanche layer is not uniform the avalanche gain depends on the position inside the medium and is expressed in terms of impact ionisation coefficients as [2],

$$M(x) = \frac{\exp(-\int_0^x [\alpha(x') - \beta(x')]dx')}{1 - \int_0^W \alpha(x')\exp(-\int_0^{x'} [\alpha(x'') - \beta(x'')]dx'')\mathrm{d}x'} \quad (6)$$

Where *W* is the width of the depletion region and the primary current is generated at a position *x* inside the depletion region. Assuming an ideal *p-i-n* diode where the electric field in *i*-layer is uniform, the ionisation coefficients no longer depend on the position and in this case the avalanche gain is expressed as,

$$M(x) = \frac{(\alpha-\beta)\exp[-(\alpha-\beta)x]}{\alpha\exp[-(\alpha-\beta)w]-\beta} \quad (7)$$

M(x) decreases with *x* when $\alpha>ß$ and increases with *x* when $\alpha<ß$. This results in two cases where a maximum avalanche gain is achieved i.e. *x=0* which is gain due to electrons only and *x=W* which is gain due to holes only. These two cases are referred to as pure electron and hole injection conditions. Avalanche gain is a stochastic process and the randomness of impact ionisation process adds an extra source of noise to an otherwise single carrier avalanche process. The noise spectral density of mean square current rising from this randomness is expressed as,

$$\langle i^2 \rangle = 2qI_{pr}M^2F \quad (8)$$

Where *q*, I_{pr}, *M* and *F* are the electronic charge, primary current, avalanche gain and excess noise. McIntyre [2] expressed the excess avalanche noise as a function of avalanche gain and the ratio of impact ionisation coefficients $k=ß/\alpha$ assuming that ionisation coefficients only depend on the electric field and *k* is constant, as

$$F = kM + (1-k)\left(2-\frac{1}{M}\right) \quad (9)$$

Eq. 9 shows that the excess noise is smaller for a smaller *k* value i.e. a pure electron injection for the case when $\alpha>ß$. Similarly for pure hole injection the *k* is defined as $\alpha/ß$ and a low excess noise is expected if only holes impact ionise provided that $ß>\alpha$. For one dimensional depletion region with width, *W*, an electron current density at *x=0* is assumed to trigger the avalanche, the current density increases throughout the repletion region as a result of electrons generated in impact ionisation process as illustrated in Fig. 2. At the end of the depletion region, *x=W*, the electron current density reaches a maximum, amplified by the avalanche gain *M*. In the case where holes also undergo impact ionisation, a hole avalanche results in a bi-directional, random avalanche process as the holes drift in opposite direction under the action of electric field. A higher degree of randomness in the avalanche process leads to a noisier avalanche process in comparison with a single carrier, less noisy avalanche. Fig. 3 schematically illustrates a comparison of a single carrier avalanche initiated by electrons and a bi-directional avalanche due to both electrons and holes. In Fig. 3(a), the red arrow representing the electron avalanche

is thicker in comparison with Fig. 3(b) which represents avalanche due to both electrons and holes.

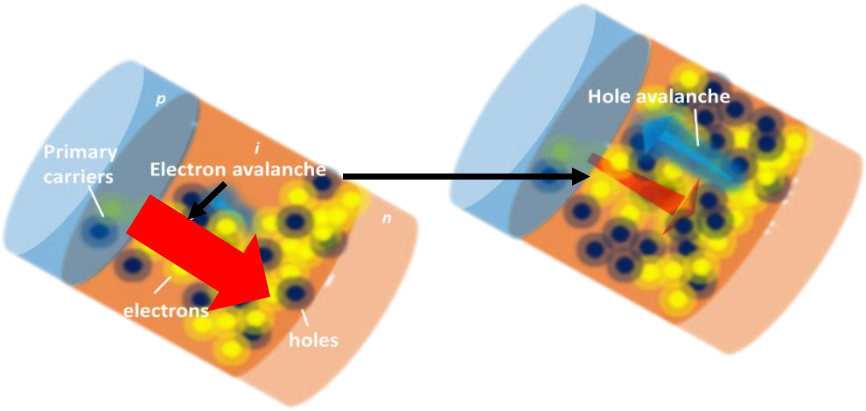

Fig.3 Conceptual schematic of avalanche excess noise. (Left) p-i-n diode showing a dominant impact ionisation of electrons. Red arrow shows the direction of electron avalanche. (Right) A noisy avalanche process where electrons and holes ionise simultaneously setting up electrons and holes avalanche.

In practical applications where APDs are routinely used with amplifiers to boost the signal, the signal to noise ratio is enhanced by the APD provided that the excess noise arising from avalanche (APD noise) is smaller than amplifier noise.

2.4 Geiger mode operation of avalanche photodiodes

The detector sensitivity can be increased by increasing the applied reverse bias. Depending on the magnitude of reverse bias, the detector operates in either the linear mode or Geiger mode. In linear mode, a finite gain can be achieved typically less than 1000 as a result of chain of impact ionisation events. However to enhance the sensitivity of the detector down to single photon level, the device is biased above the breakdown level. Fig. 4 shows the dark *I-V* characteristics for a typical APD with nominal breakdown voltage in the range of 12.3 V.

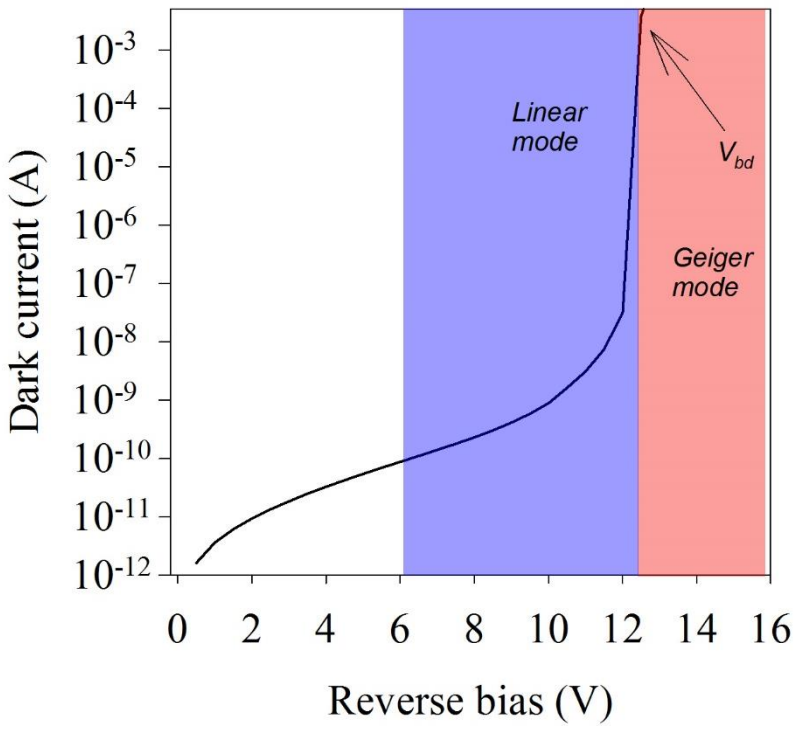

Fig.4 Dark I-V of a p-i-n APD. Linear and Geiger modes are shown. Typical breakdown voltage in this case is 12.3 V.

As shown in Fig.4, the Geiger mode APDs (GM-APDs) are biased above the breakdown voltage which enhances their capability to detect single photons by generating a macroscopic avalanche current through impact ionisation process. The impact ionisation process can be triggered by photo carriers generated by absorption of incoming light or by dark carriers generated through thermal effects. Due to their enhanced sensitivity, GM-APDs can achieve higher gain in the order of 10^6. The macroscopic avalanche current however continues to grow and can increase to an extent the device could suffer from a permanent heat damage. Therefore an avalanche "quenching" mechanism is needed to reduce the applied reverse bias quickly below the breakdown voltage. This is achieved by superimposing an *AC* pulse (overbias pulse) on a *DC* bias which is held slightly below the breakdown voltage. This way the GM-APD is only armed to detect photons or dark carriers only during the narrow overbias pulse duration. The total voltage above the breakdown is referred to as excess bias. Fig. 5 shows a schematic illustration of the process.

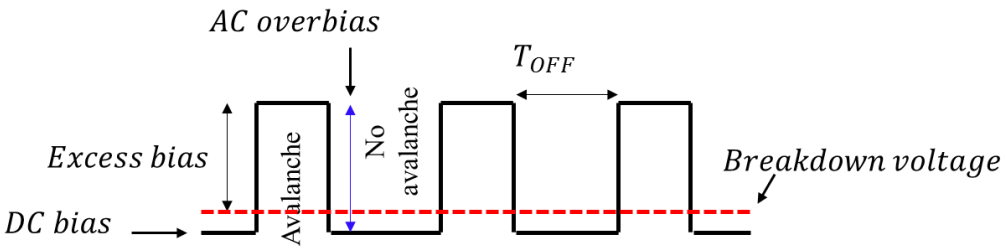

Fig. 5 Schematic illustration of gated mode operation of a Geiger mode APD. The red line shows the breakdown voltage, vertical black double headed arrow shows the pulse amplitude above the breakdown voltage while the blue arrow shows the magnitude of the AC "Overbias" pulse.

Following are the steps needed to operate a Geiger mode APD for a photon or a dark carrier detection.

1. A *DC* bias (close to breakdown voltage) is applied to the cathode of the Geiger mode APD.
2. A narrow *AC* pulse (several nanoseconds) is superimposed on the *DC* bias. The pulse repetition frequency is set such that the device is biased above the breakdown for a small period of time, typically nanoseconds. The duty cycle of the pulse trains determines the time for which the detector is armed to sense the onset of avalanche breakdown.
3. Narrow pulses are used to prevent the diode from thermal damage and the avalanche process quickly needs to be "quenched" which is achieved by bringing the applied bias below the breakdown voltage.
4. The device is armed to detect an avalanche event during the ON time of the pulse and is unable to sense the avalanche during the OFF time.

In the Geiger mode however the major source of noise that limits the single photon detection efficiency (*SPDE*) is the so-called Dark Count Rate (*DCR*) and Afterpulsing.

2.4.1 Dark count rate (*DCR*)

Dark Count Rate (*DCR*) is a major source of noise in Geiger mode operation of avalanche photodiodes. It is defined as the number of times per seconds an avalanche is triggered inside the avalanche layer in absence of photo-generated carriers. Such "dark" carriers can be thermally generated inside the avalanche region and the number of these carriers

increase with operation temperature or through band-to-band tunnelling. Avalanche material with a wider bandgap is beneficial in mitigating the excessive band-to-band tunnelling. Eq. (10) shows band-to-band tunnelling current as a function of the material bandgap energy [3].

$$I_{tunn} = \frac{(2m*)^{0.5} q^3 EVA}{h^2 E_g^{0.5}} \exp\left(\frac{-2\pi\sigma_t (m*)^{0.5} E_g^{1.5}}{qhE}\right) \quad (10)$$

Where m^*, q, E, V, A, E_g, h are effective electron mass, electronic charge, electric field, applied reverse bias, device area, bandgap energy and Planck's constant respectively and σ_t is a material dependent constant. For indirect bandgap materials, the bandgap energy E_g in Eq. (10) is replaced with $E_g + E_p$ where E_p is phonon energy. Considering N number of dark carriers present in the avalanche region during a certain time, the effective number of dark counts (C_D) recorded when the Geiger mode APD is biased above the breakdown for time t using a pulse train of a repetition frequency, f can be expressed as,

$$C_D = f\left(1 - exp(-Nt)\right) \quad (11)$$

If the product Nt is very small, the exponential term in the braces can be expanded according to Taylor's series as simply 1- Nt and the dark count C_D is fNt. The number N is referred to as dark count rate (*DCR*) and is simply the dark counts C_D normalised to duty cycle ft of the pulse train. The *DCR* in this thesis is consistently expressed in terms of pulse width t (in nanoseconds) and pulse repetition rate f according to,

$$N\ (DCR) = \frac{C_D}{ft} \quad (12)$$

DCR can be lowered by cooling the temperature of Geiger mode APD and/or lowering the overbias. Most practical systems utilising the state-of-the-art single photon detectors [4] are equipped with Peltier cooler elements to keep the temperature low enough to minimise the thermal generation component of *DCR*.

2.3.2 Afterpulsing

Afterpulsing is a major bottleneck in high frequency operation of SPADs. Afterpulsing refers to the re-triggering of the avalanches resulting from charge carriers trapped in the material defect sites or charge trapping centres. These trapped carriers result from the

charge flow during avalanche process and they can initiate unwanted avalanches once they are released from the trapping centres. These trapping centres have a finite life time and the carries trapped within these defects are re-emitted at their characteristic life time. Afterpulsing results in increase of *DCR* and therefore it is preferred to keep afterpulsing to a minimum.

In Geiger mode where the device is biased above the breakdown voltage, an avalanche could seed a significant charge flow through the material. To reduce the afterpulsing there are two major approaches:

- Improve material quality and eliminate the defect centres.
- Reduce the charge flow to minimise the trapped carriers.

State of the art Geiger mode technology for 1550 nm detection suffers from high DCR and afterpulsing compared to Si owing to its poor material quality in terms of defects [5] which act as charge carriers trapping centres. It is therefore a common practice in the 1550 nm Geiger mode technology to restrict the amount of charge in the first place to suppress *DCR* and afterpulsing.

Restricting the amount of charge flow through the avalanche layer however poses some challenges and trade-offs must be made. To illustrate this point, we express afterpulsing probability as [6]

$$P_{ap}\,(\%) \propto e^{-\frac{t_d}{\tau}}(C_d + C_p)\int_0^t V_e(t)dt \tag{13}$$

Here $t_d, \tau, C_d, C_{p,}, t,\ V_e$ are the dead time, decay time of the trapping centres, device capacitance, parasitic capacitance of the circuit, avalanche duration and excess bias. Dead time usually refers to the time following an avalanche detection where the detector remains inactive (T_{off} in Fig. 4). This allows for charge carriers to release and evacuate the traps. Generally, the dead time should be longer than the trap life time to allow a proper release of the trapped carriers.

From Eq. (13), there are several approaches to minimise the afterpulsing probability, namely:

1. Increasing the dead time or the hold off time where the device remains inactive following a detection event. This time must be greater than the life time of the de-trapping centres so that any residual charge is released, and the traps emptied.

2. Reducing the total capacitance of the device including any parasitic capacitance.
3. Reducing the total charge through the active layer.
4. Reducing the excess bias and
5. Reducing the trap life time by increasing temperature.

However, these approaches carry their own limitations. Using approach (1) can reduce the afterpulsing however this approach severely limits the speed of detector. In such a scenario a maximum repetition is limited by the inverse of T_{off}. This approach can however severely limit the gating frequency and hence detection rates are limited.

Approach (2) and (3) can reduce the avalanche charge however a major challenge with this scheme is the extraction of weak avalanche signals if the transient signals due to rising edge of bias pulses are stronger [6]. Approach (4) can reduce the afterpulsing however this leads to a reduced breakdown probability which lowers the *PDE* (defined in Eq. 14). Approach (5) can precipitate the release of trapped carries from the defect sites however this can exacerbate the *DCR* through thermal generation component. It is therefore clear that trade-offs must be made to achieve an optimal performance depending on the type of application. In this context the major trade-off in the current SPAD market is to find a sweet point between achieving a maximum *SPDE* and a reduced afterpulsing. To achieve a maximum count rate, a high gating frequency must be used to benefit from duty cycle however this exacerbates the afterpulsing due to a relatively smaller dead time.

2.4.3 Single Photon Detection Efficiency (SPDE)

When the electric field is increased, the probability that an avalanche breakdown is initiated by a photo-generated carrier in the avalanche layer increases. Consequently, the ability of a Geiger mode APD to generate an avalanche signal in response to single photon is enhanced. The capability of a Geiger mode APD to convert a single photon generated photo-carrier to an avalanche is quantified as a *SPDE* (expressed in percentage). *SPDE* is mathematically expressed as the ratio of avalanche events registered under light illumination to the number of events registered under zero illumination, normalised to the number of photons in the incident radiation. Both the *DCR* and *SPDE* increase with applied overbias [7] and therefore commercial single photon detector are characterised by both the *SPDE* and *DCR* in commercial specification sheets provided by

manufacturers. As a standard approach, a sweet spot is always selected corresponding to an overbias which ensures a maximum *SPDE* while maintaining a minimal *DCR*. *SPDE* can be mathematically expressed as

$$SPDE = \frac{1}{n_p}\ln\left(\frac{1-counts_D/f_g}{1-counts_L/f_g}\right) \quad (14)$$

Where n_p , $counts_L$ and $counts_D$ are the mean number of photons per laser pulse, total number of counts registered under light illumination (sum of dark and photon counts) and total counts registered under no light. In quantifying Eq. 14 a Poisson distribution of arrival of photons is considered where f_g is the pulse duty cycle. Qualitatively Eq. 14 refers to the mean number of photons detected per second when a SPAD is illuminated with a laser pulse with a pre-defined mean photon number per pulse relative to the total *DCR* registered when the SPAD is not illuminated.

For practical application systems utilising linear mode APDs, the temperature coefficient of avalanche breakdown, C_{bd} has to be considered. In rugged operating conditions and applications where a maintaining a stable gain for APDs is crucial, APDs with a reduced C_{bd} are preferred. Commercial APD detector packages are installed with temperature stabilisation/ compensation mechanisms [8] which adjust the bias voltage to compensate any variation in the breakdown voltage due to temperature effects. Similarly for commercial GM-APDs the datasheets often specify the performance in terms of *DCR*, *PDE* and afterpulsing [9,10].

References

[1] http://www.iue.tuwien.ac.at/phd/triebl/node20.html

[2] R. J. McIntyre, “The distribution of gains in uniformly multiplying avalanche photodiodes: Theory,” *IEEE Transactions on Electron Devices*, vol. 19, no. 6, pp. 703–713, Jun. 1972.

[3] S. Xie and C. H. Tan, "AlAsSb Avalanche Photodiodes With a Sub-mV/K Temperature Coefficient of Breakdown Voltage," *IEEE Journal of Quantum Electronics*, vol. 47, no. 11, pp. 1391-1395, Nov. 2011.

[4] “ID230 NIR photon detector from ID Quantique,” ID Quantique, Geneva, Chemin de Marbrerie, Carouge, Switzelrand.

[5] D. Hall, Y. H. Liu, L. Yan, Y. Yu, and Y. H. Lo, “Approaching the Quantum Limit of Photodetection in Solid-State Photodetectors,” *IEEE Transactions on Electron Devices*, vol. 64, no. 12, pp. 4812–4822, Dec. 2017.

[6] J. Zhang, M. A. Itzler, H. Zbinden, and J.-W. Pan, “Advances in InGaAs/InP single-photon detector systems for quantum communication,” *Light: Science & Applications*, vol. 4, no. 5, p. e286, May 2015.

[7] M. A. Itzler, X. Jiang, B. Nyman, R. Ben-Michael, and K. Slomkowski, “InP-based single photon avalanche diodes,” 2008, pp. 226–227. Princeton Lightwave Inc., *LEOS, 2008*

[8] “Thorlabs.com - InGaAs Avalanche Photodetectors.” [Online]. Available: https://www.thorlabs.com/NewGroupPage9_PF.cfm?ObjectGroup_ID=4047.

[9] https://www.idquantique.com/single-photon-systems/products/id220/

[10] https://www.princetonlightwave.com/products/ingas-nir/

Chapter 3

Experimental Methods

This chapter provides information on experimental methods carried out to characterise linear and Geiger mode photodiodes. These techniques include current-voltage (*I-V*) measurement, capacitance-voltage (*C-V*) measurement, phase sensitive detection for photo-multiplication current measurement, dark count rate (*DCR*) measurements in gated mode, and photon counting characterisation using Multi-Channel Analyser (*MCA*).

3.1 Current Voltage Measurements

The basic characterisation for a diode is the current-voltage (*I-V*) characterisation. *I-V* characterisation were carried out with an HP 4175 picoammeter. The device-under-test (*DUT)* was probed with clean metal probe tips housed in an Everbeing probe holder. The picoammeter applies bias in both forward and reverse polarity and measures current from the *DUT*. The diode current in forward bias is described in Eq. (1) as [1]

$$I_F = I_\circ exp\left(\frac{q(V - I_{Fi}R_S)}{nk_BT} - 1\right) \quad (1)$$

Where I_F is forward current, I_0 is saturation current, q is electronic charge, V is the applied bias, R_s is the series resistance, k_b is Boltzmann's constant and n is the ideality factor of the diode. Fig.1 shows the schematic of experimental setup for recording *I-V* characteristics of a diode. A bias source V_B provides bias in both forward and reverse bias and corresponding current is measured across the resistor, R connected in series with *DUT*.

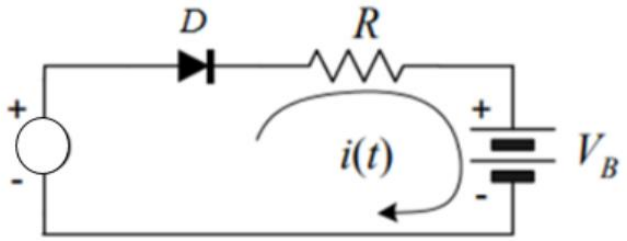

Fig.1 I-V measurement setup for diode, D. Bias source V_B provides forward and reverse bias whereas current through the device is measured across the resistor R (typically 10 – 100 Ω).

Ideality factor, *n* in Eq. (1) is a measure of the slope of the *I-V* data at lower forward bias and shows whether generation-recombination or diffusion is dominant in the *p-n* junction. If *n* =1 signifies the dominance of the diffusion current in the *p-n* junction whereas *n* = 2 signifies the presence of generation-recombination currents in the junction. I_{fi} is the forward current without series resistance effect. Series resistance can result in the deviation of the forward current I_F from an ideally exponential increase as a function of forward bias as shown in Fig. 2.

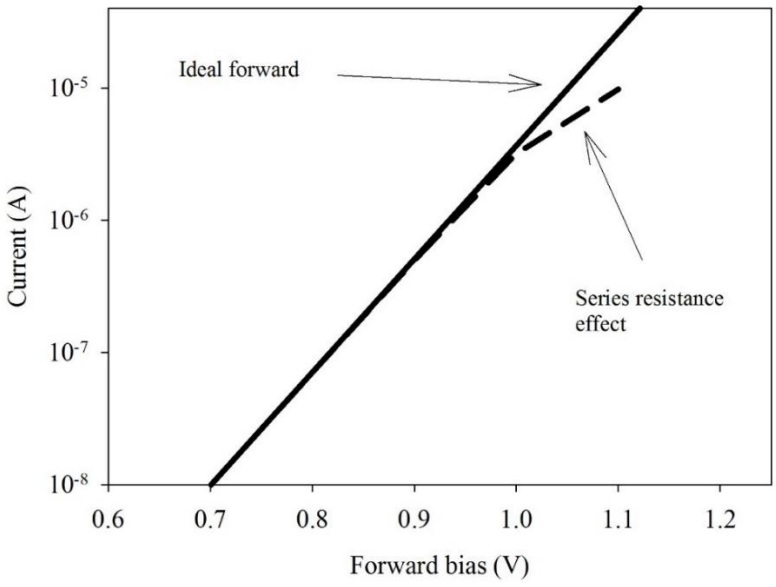

Fig2 Semi-log plot of forward current as a function of forward bias. Series resistance effect is shown where the forward current deviates from ideal exponential increase.

For linear mode diodes studies in this thesis, the dark currents can arise from currents flowing through the bulk of the device or along the perimeter of the mesas. Diffusion current, I_{diff}, generation-recombination currents, $I_{g\text{-}r}$ or band to band tunnelling current, I_{tun} constitute the bulk components. Surface leakage currents can arise from the dangling bonds caused by abrupt termination of the semiconductor surface at the mesa sidewalls. Therefore, the scaling of the dark currents with the bulk area suggests the dominance of the bulk currents. Similarly in case of dark currents scaling with diode perimeter, the dominant mechanism can be surface leakage. For Geiger mode mesa diodes studied in this thesis, dark counts arise from bulk currents through the device. Surface leakage components do not contribute to the dark counts as they do not flow through the diodes' bulk area and hence are not multiplied when the device is operated in Geiger mode. From the reverse bias current, information on breakdown voltage, dark current levels, bulk and surface leakage current levels can be obtained.

3.2 Capacitance Voltage Measurements

C-V measurements are performed to extract important device parameters including depletion width (calculation of depletion width is performed using Poisson's equation and is detailed in Appendix. A) and doping in epitaxial layers. The capacitance of *DUT* is measured with an HP-4275 LCR meter. The schematic experimental setup is shown in Fig. 3. The *LCR* meter is equipped with a four probe capacitance measurement setup. Using this technique, the instrument measures the *AC* impedance of the *DUT* by applying an *AC* voltage superimposed on a *DC* signal to the device and measures the output current. The typical *AC* test signal level is 50 mV with an oscillation frequency of 1 MHz.

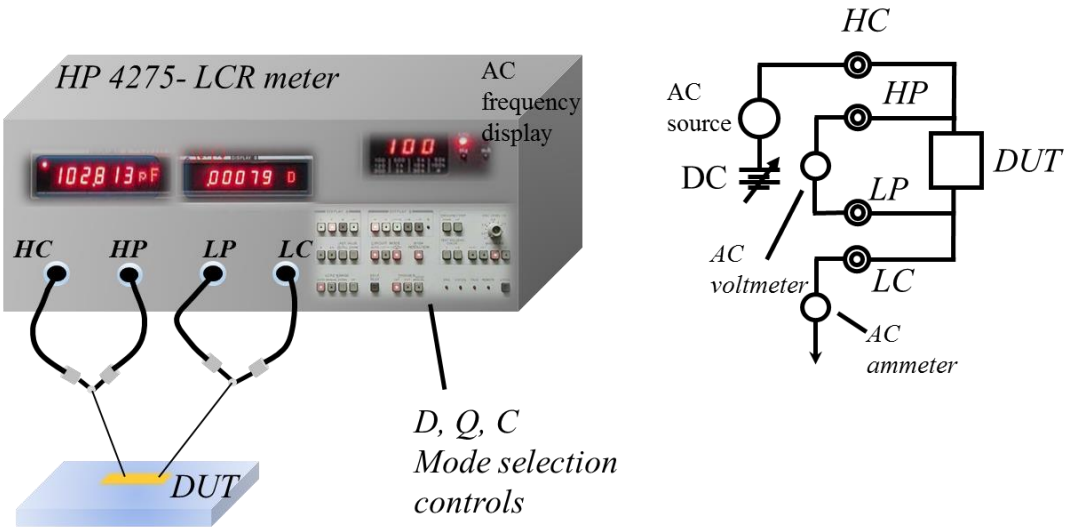

Fig.3 Schematic of experimental setup for C-V characterization. The conceptual illustration of four point probe method is shown in the right pan. Controls for displaying dissipation factor, D, quality factor, Q and capacitance values are provided to output desired parameter. H_C, H_P, L_C, L_P indicate high current, high potential, low current and low potential respectively.

The instrument measures the vector impedance of the sample and calculates various parameters i.e. dissipation factor, quality factor and phase angle between the voltage and current vectors which can be displayed on the channel outputs using the control knobs. The reactance of the sample is subsequently calculated using the test signal and the current recorded from the sample. Subsequently the capacitance of the *DUT* is calculated with the measured reactance using the relation

$$C_{DUT} = \frac{I_{DUT}}{2\pi f V_{AC}} \tag{2}$$

Using the *AUTO* mode on the LCR meter, the instrument selects appropriate mode for recording the capacitance of the device. For semiconductor devices as the *DUT*, a series mode of the device is used to model the capacitance. Using the series mode for the typical capacitance values of the diodes, the instrument measures the reactance of the sample to an accuracy of ± 0.1% at a test signal frequency of 1 MHz. It is of utmost importance to set the appropriate test signal frequency as this directly affects the measurement accuracy of the reactance and hence the capacitance of the sample. As a guideline of estimation of reactance accuracy the reactance chart can in Fig.4 be consulted.

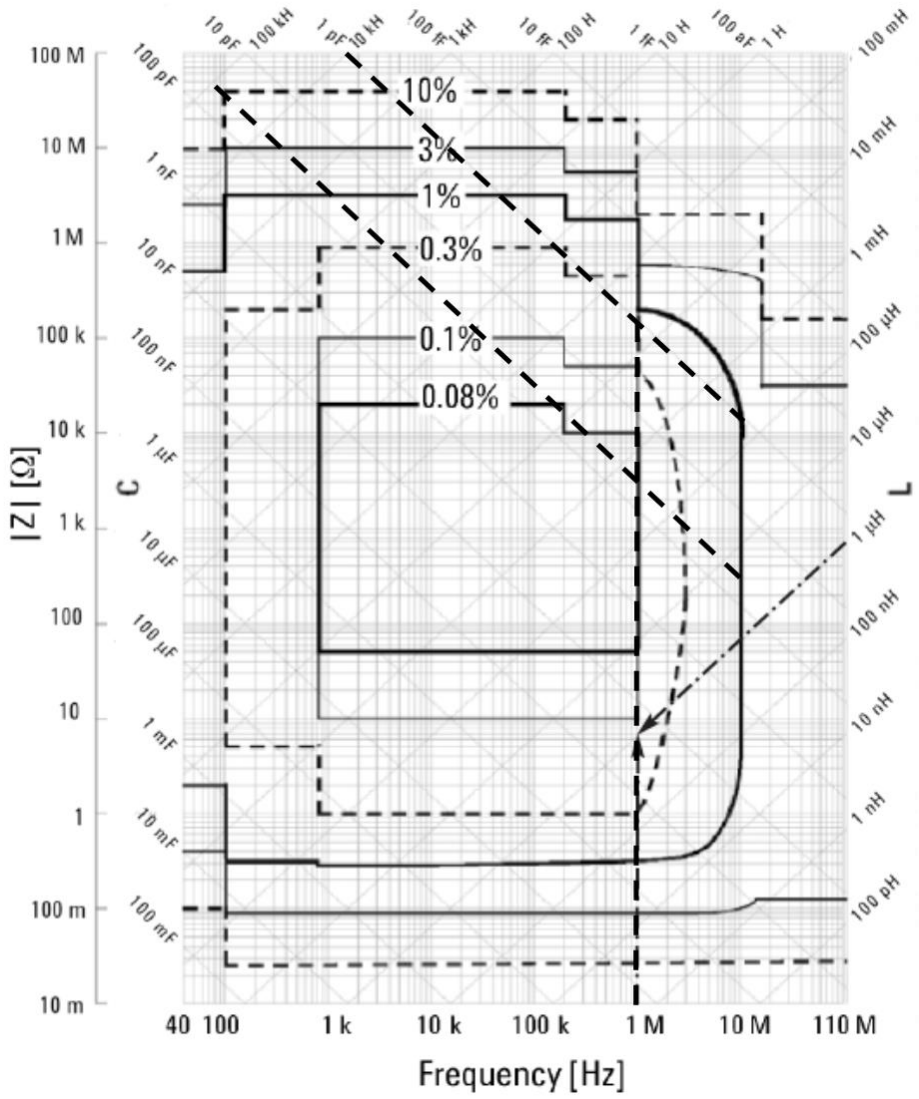

Fig. 4 Measurement accuracy indicated in the reactance chart. Different zones on the chart show ranges of the accuracy provided by the measurement instrument [2].

The reactance can be estimated at 0.08 - 0.3% using a test signal frequency of 1 MHz for the expected capacitance of our diodes using the permittivity of AlGaAsSb layer (ε = 10.95). Using the phasor diagram of the series *RC* circuit, the phase angle between the current and voltage vector is given as

$$\theta = -\tan^{-1}\left(\frac{1}{\omega CR}\right) \tag{3}$$

A phase angle corresponding to -90° is used as a reference for registering accurate capacitance value within in the range specified by the reactance chart. The instrument

alternatively outputs values of dissipation factor and phase angle (channel A) and quality factor and impedance (channel B). The *DUT* capacitance decreases with increasing reverse bias due to increasing depletion width where the capacitance is calculated using Eq. (4).

$$C = \frac{A\varepsilon_o\varepsilon_r}{d} \tag{4}$$

Where *A* is the mesa device area and *d* is the depletion width.

3.3 Photo current measurement

Photo-multiplication current measurement is done to calculate the multiplication gain for linear mode *p-i-n* diodes. The increase in the depletion width as a result of applied reverse bias results in the enhancement of the collection efficiency of photo-generated carriers which contribute to the total current when they are swept across the high field region and collected on *DUT* electrode. The change in this primary current as a function of the photo-generation rate of the carriers can be estimated with Eq. (5) following the method used by Woods [3].

$$I_{pr}(V) = \frac{qR}{cosh(\frac{D(V)}{D_m})} \tag{5}$$

Where *q, R, D (V)* and D_m are charge per carrier, carrier photo-generation rate, bias dependent distance of depletion edge from the surface and minority carrier diffusion length. Under the approximation of $D_m >> D(V)$, the primary current can be linearly approximated as

$$I(pr) = mV + c \tag{6}$$

Where *m* represents the slope of the current vs bias at low voltages where it exhibits a linear dependence on reverse bias. The multiplication gain is then calculated by normalising the photocurrent to the primary current. Fig. 5 shows the primary and multiplied photocurrent in arbitrary units.

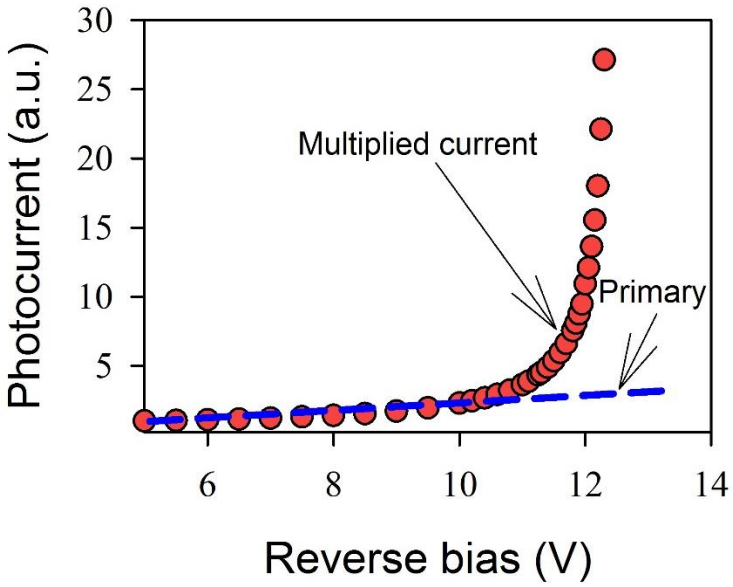

Fig. 5 Multiplied and primary current as a function of reverse bias. Multiplication gain is the ratio of multiplied and primary photocurrent.

For photo-multiplication measurements, the *p-i-n* diodes are illuminated with a laser spot which is focused onto the top of the mesa. The laser spot size is very important and it must be focused onto the center of the mesa to avoid stray light falling on the edges of mesa sidewalls. The reverse bias voltage was provided by a Keithely-236 Source Measurement Unit (*SMU*). The photocurrent generated from the *DUT* was sifted from the dark current using a phase sensitive detection technique (*PSD*) which calculates the photocurrent at a fixed reference frequency. A Stanford Research Systems (SRS-830) Lock-In Amplifier (*LIA*) is used for this measurement. Schematic of the experimental setup is shown in Fig. 6. Photocurrent is extracted through phase sensitive detection which is explained in the following section.

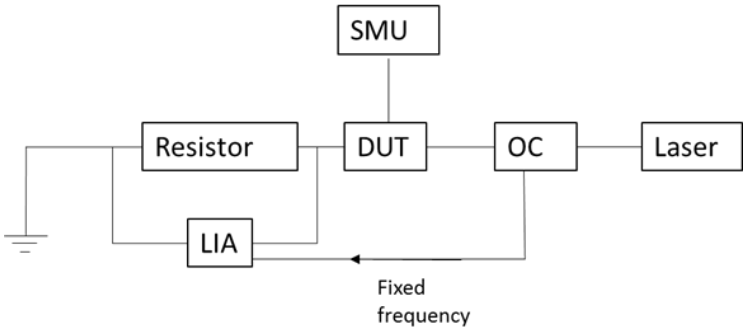

Fig. 6: *Schematic representation for the photo-multiplication measurement. LIA: lock in amplifier, SMU: source measurement unit, OC: optical chopper, DUT: Device under test.*

3.3.1 Phase sensitive detection

The *LIA* measures the signal at a reference frequency across a resistor connected in series with the *DUT* at an external reference frequency provided by an optical chopper, 180 Hz in this case. The reference frequency is chosen to avoid line frequency (50 Hz in the U.K) and its integral multiples. The external chopping of the laser beam will generate a square wave photocurrent at the reference frequency, f_{ref}. Using the Fourier series expansion, an ideal square wave with a peak to peak voltage can be represented as a sum on infinite number of sine waves and is represented mathematically as

$$S(t) = \frac{4}{\pi}\sum_{k=1}^{\infty}\frac{\sin(2\pi(2k-1)ft)}{2k-1} \tag{7}$$

$$= \frac{4}{\pi}\left(\sin(2\pi ft) + \frac{1}{3}\sin(6\pi ft) + \frac{1}{5}\sin(10\pi ft) + \cdots\right) \tag{8}$$

The *LIA* only detects the *RMS* value of first harmonic component and the photocurrent is computed by normalising the *LIA* output to the test resistor, R_{test} and is given by

$$V_{LIA} = \frac{2\sqrt{2}}{\pi}\sin(2\pi ft) \tag{9}$$

$$I_{ph} = \frac{2\sqrt{2}}{\pi\, R_{test}}\sin(2\pi ft) \tag{10}$$

3.3.2 Gain measurement at elevated temperatures

For avalanche gain measurements and elevated temperatures, a setup similar to the photo-multiplication setup in Fig.6 was used with an addition of heated copper plate where the *DUT* is placed. The temperature of the copper plate is monitored through a thermocouple sensor while a current supply to the copper plate was controlled to achieve the desired temperature. The temperature can be adjusted in the range of room temperature up to 373 K. A LABVIEW interface is used to acquire the *LIA* values directly using a GPIB

interface. Fig. 7 shows the schematic of the gain and photocurrent measurement at elevated temperatures.

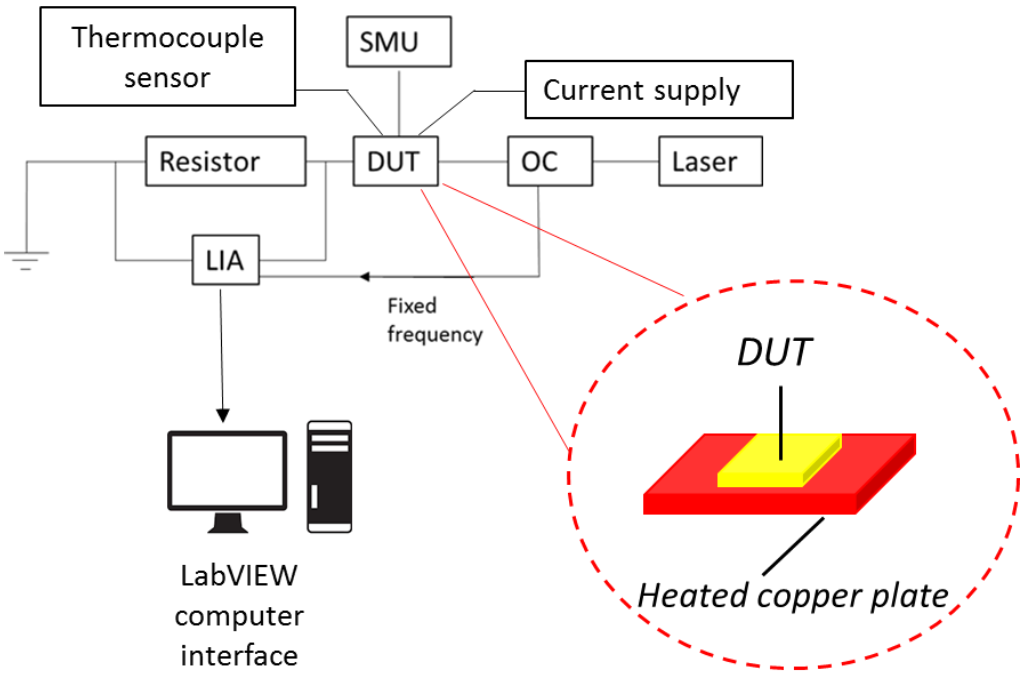

Fig. 7 Schematic setup of the gain measurement at elevated temperature. The DUT is placed on a heated copper plate as shown in the zoomed in portion

3.4 Dark count rate measurement

Dark counts are a major source of noise in Geiger mode operation of avalanche photodiodes as briefly discussed in the introduction. A *DUT* is biased above the breakdown voltage by an excess bias, V_{ex}. In the Geiger mode, the diode is biased with a short gate pulse on the order of few tens of nanoseconds to several hundred nanoseconds. The magnitude of this *AC* pulse is set at a level that biases the devices above the breakdown voltage. Upon a detection of avalanche breakdown event, a sensitive discriminator circuitry senses the avalanche event and registers a count. A capacitive quenching circuitry [4] (developed by Dr. Simon Dimler, University of Sheffield) quickly lowers the bias below the breakdown and terminates the avalanche current. We remind the reader that the experimental setup described in this section yields the dark counts C_D (described in Eq. 12, chapter 2) on a LabVIEW interface and the *DCR* (shown as N in Eq. 12 chapter 2) can then be calculated by normalising the

dark counts to the pulse duty cycle. The following section details the measurement of dark counts C_D as function of excess bias.

3.4.1 Dark count as function of excess bias

Figure 8 shows the schematic diagram for dark count measurement of Geiger mode avalanche photodiodes. Device under test (*DUT*) is housed under the capacitive quenching circuitry (*CQC*). Detailed operation procedure of the *CQC* system is given in ref. [4].

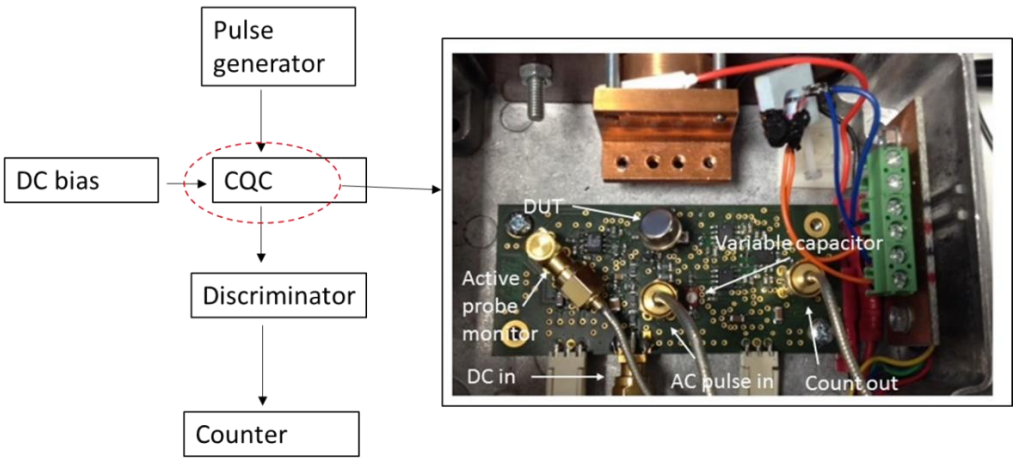

Fig.8 Schematic diagram of dark count measurements with the capacitive quenching scheme. The DUT is mounted inside a capacitive quenching board.

An Agilent 81101-A pulse generator is used to provide *AC*-pulses at repetition rate up to 100 kHz. The typical pulse width used in experiment is adjustable from 9.09 ns to 1 us with a rise time of 4.5 ns. A Keithley 2612 source meter provides *DC* bias to the device. A positive *AC* pulse with an amplitude V_{ac} is superimposed on *DC* bias level. The *DUT* is biased such that $V_{ac} + V_{dc} > V_{bd}$ i.e. above the breakdown voltage. During the overbias pulse active gate, the device remains armed for detection. The active gate along with avalanche signal is schematically shown in Fig. 9.

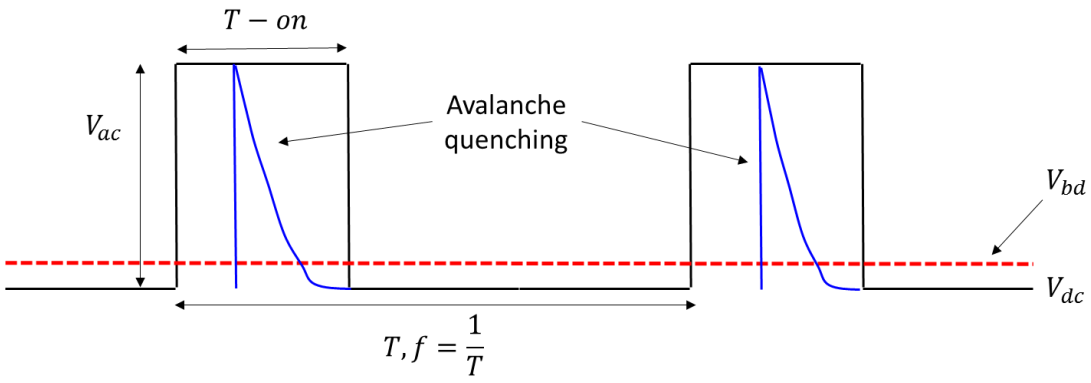

Fig.9 Schematic illustration of gated mode quenching scheme used in this thesis. T-on in the gate duration, f is the gate repetition frequency. Blue trace shows the avalanche event detected and subsequently quenched through discharging of biasing capacitance.

The system can only detect one avalanche event per pulse which places an upper limit of repetition frequency on the maximum dark count, C_D (Eq.12 in chapter 2). The pulse repetition frequency in turn is limited by the recharge time of the *DUT* through the series resistance of the *DUT* and is illustrated in the following section.

3.4.2 Influence of biasing capacitance and device series resistance on pulse repetition frequency

The core of the *CQC* circuit is shown in Fig. 10. The *AC* overbias pulse is applied at the input of the biasing capacitance which limits the charge flow through the device. The *AC* overbias pulses are superimposed on *DC* bias level at the device electrode at point A. Blocking diode, C_D is used to supply a stable overbias pulse to the device, R_2 (1 kΩ) is used to provide protection from accidental DC bias to the device and. Avalanche current can be measured across a resistor R_1 (50 Ω) connected in series with the device

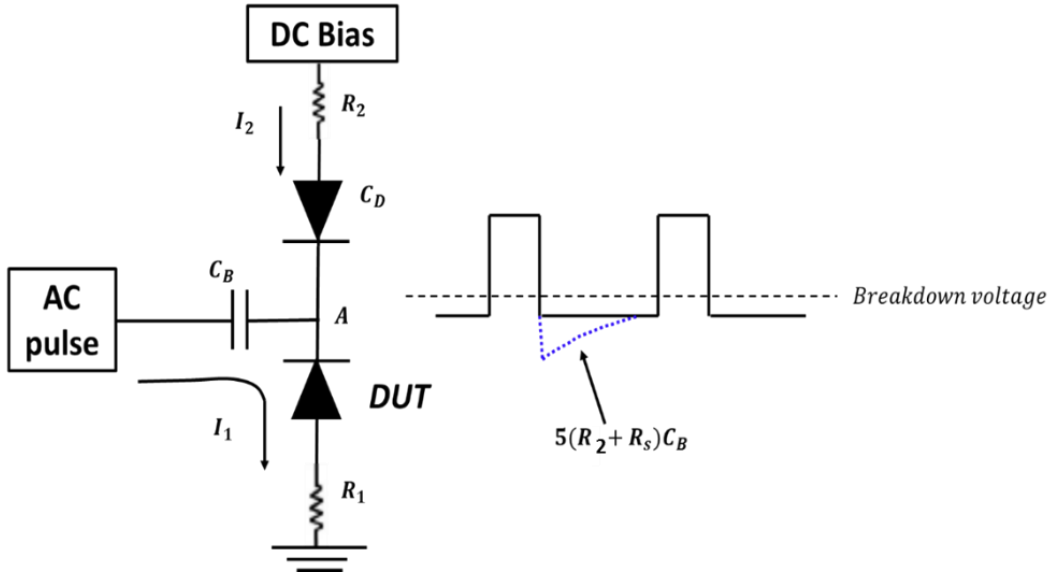

Fig.10 Core of the CQC shown along with the device, DUT. The pulse sequence is shown.Blue dashed line shows the recharge of the DUT voltage at point A to the applied DC bias. The illustration is schematic and is not to scale.

The device remains armed to detect avalanche event during the gate on time when it is biased above the breakdown voltage. In the event of an avalanche event being triggered at the end of the applied overbias pulse, the avalanche signal flows through the device discharging its capacitance through device's series resistance. The current lost from node A, I_1 is quickly replaced by current I_2 which recharges the voltage at point A to *DC* bias. The recharge time is dominated by the biasing capacitance, C_B (15 pF), R_2 and device capacitance. The device series resistance is extracted from the forward *I-V* data using the procedure described in sec. 3.1. The 5× recharge time constant determined by the series resistance of the *DUT* and the biasing capacitance limits the maximum pulse repetition frequency. In our characterisation, R_2 is fixed at 1 kilo Ohms. Relatively fast recharge may be possible if the resistor R_2 is removed however doing so will expose the *DUT* to any accidental *DC* bias. A major challenge in the avalanche signal processing is the extraction of weak avalanche signals particularly in the presence of strong capacitive transient signals due to rising edge of overbias pulses. This is explained in the following section. The use of biasing capacitance involves trade-offs in measurement and are explained below.

- Using a higher biasing capacitance leads to a clean and stable overbias pulse [5] to the *DUT* however it results in a larger recharge time of the *DUT* to the stable *DC* bias level which ultimately limits the pulse repetition frequency.

- A smaller biasing capacitance leads to a reduced charge flow through the avalanche region of a Geiger mode APD however the extraction of weak avalanche signals can be challenging if they are smaller than the capacitive transient signals resulting from the device capacitance and the overbias pulse rise time. In the next section we discuss the extraction of weak avalanche signals.

3.4.3 Avalanche signal discrimination and capacitive transient signals

The avalanche is quenched through a discharging action of the biasing capacitance, C_B which is nominally 15 - 33 pF in our measurements. As mentioned earlier, the rising edge of such an avalanche signal is sensed by a fast discriminator which triggers out a Nuclear Instrument Module (*NIM)* signal for every detection. The resulting *NIM* output is fed to a Canberra 512 counter for counting avalanche events. A LABVIEW interface is used to record the dark counts over a user specified time window and the result is averaged to yield a mean dark count value per second. Fig.11 shows the schematic of the *DCR* measurement where the avalanche signal and *NIM* signal generation is shown. A sequence of waveforms at every node of the system is also shown in Fig.11..

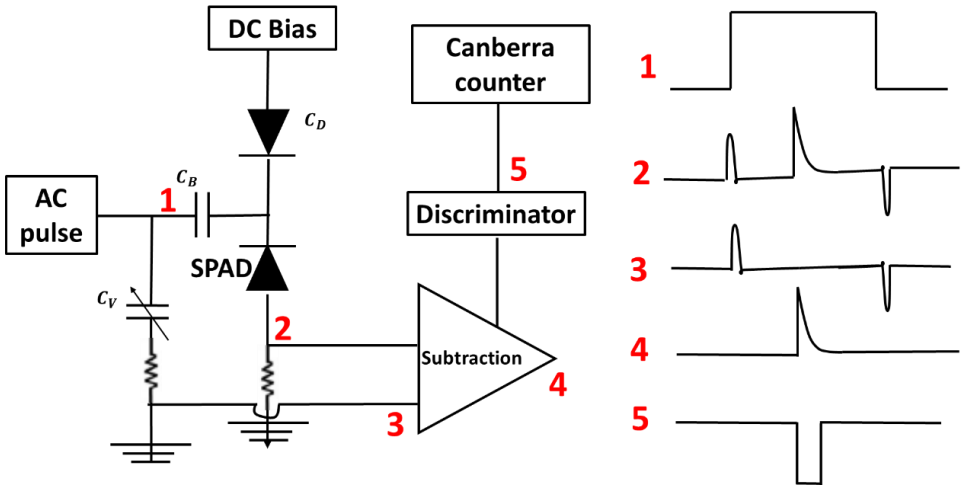

Fig. 11 Schematic of DCR measurement setup. Schematic of signals at different system inputs are shown. Typical values for different components are: C_b: 15 pF, C_d: 27 pF, R=50Ω. Time dependent waveforms are shown on the right pan of the schematic. 1: Square waveform at the input of the biasing capacitance. 2: Avalanche signal superimposed on capacitive transient signal at the output of the SPAD. 3: Capacitive transient signal from dummy capacitance at the input of op-amp. 4: Avalanche signal at the output of the op-amp. 5: NIM signal generated at the output of discriminator. All waveforms are shown as function of time.

The rising edge of the overbias pulse charges the total capacitance of the Geiger mode APD above the breakdown voltage The charging current can then be detected across a 50 Ω resistor connected in series with the *DUT*. When detecting the avalanche signals (see output of node 2 in Fig. 11), the output from the *DUT* is fed to a discriminator circuitry which generates an output pulse once the input level exceeds a certain threshold. When the rise time of the overbias pulse is very short, the current transient through the *DUT* may be strong enough to prevent the detection of avalanche signal. In Fig. 10, a hypothetical avalanche signal is shown which is comparable to the voltage transient signal (node. 2 Fig. 11). A disadvantage in this case is that if the threshold level is lowered, the voltage transient signals are mistaken for avalanche signals and yields an erroneous *DCR* value. As a solution to this, the overbias pulse is simultaneously applied to the *DUT* and a dummy capacitance, C_V with identical capacitance as the *DUT* (see node. 3 in Fig. 11). The voltage transient signal from the dummy capacitance is subtracted from the output of the *DUT* and an avalanche signal can be extracted (node. 4 in Fig. 11). The discriminator employs an Emitter Coupled Logic (ECL) to generate a *NIM* signal (node.5) in response to an avalanche signal and subsequently the Canberra counter 512 counts the number of times per second the *NIM* signal is generated. To avoid strong capacitive transients from the *DUT*, mesa devices of small size (25 μm) are used to minimise the device capacitance for a given pulse rise time. A 4.5 ns (fastest rise time with Agilent pulse generator 81101-A) pulse rise time is used in the *DCR* characterisation carried out in this thesis. Detailed construction of the ECL logic discriminator for *NIM* pulse generation is listed in ref. [4].

An important parameter for *DCR* measurement is the adjustment of threshold level for the discriminator circuitry. Setting a high threshold level can result in an apparently reduced *DCR* while too low a threshold level can result in the discriminator being triggered on noise floor. In the following section we detail the procedure for setting the threshold level.

3.4.4 Procedure for setting discriminator threshold

Following steps should be taken to ensure correct value for the adjustable threshold level of the discriminator circuitry.

- Apply the *DC* bias.
- Apply a small *AC* overbias pulse. We typically use 2 – 6 V AC overbias pulse amplitude in our measurements. Set an overbias pulse duration of 500 ns. The pulse duration should be sufficiently larger than avalanche quenching time which is predominantly determined by the time required for the capacitances of *DUT,* biasing capacitance, C_B, blocking diode, C_D, and circuit parasitic capacitances to discharge via series resistance of the *DUT*.
- Tune the variable dummy capacitor until a complete transient cancellation is achieved. Fig. 12 shows the capacitive transients resulting from the rising and falling edges of the overbias pulse and the *DUT* capacitance. With an overbias pulse amplitude of *V,* rise time of *t,* and device capacitance of *C,* the current that charges the device capacitance can be calculated as *CdV/dt.* In order to show the effect of *DUT* capacitance, the dummy capacitor is deliberately set to zero resulting in strong transient signals which can be cancelled out by tuning the dummy capacitance for complete transient cancellation as shown in Fig. 12 (b).
- Slowly increase the *DC* bias until the avalanche signals start to appear. Increasing the *DC* bias will lead to stronger avalanche signals.
- At the smallest *DC* bias where the avalanche signals start to appear, multiple *NIM* signals will appear indicating that the discriminator is triggered on spurious noise floor in addition to the avalanche signals.
- Slowly increase the threshold level on the discriminator until a *NIM* pulse is triggered once per overbias pulse. Fig. 13 illustrates the avalanche signals and *NIM* output signals for example threshold levels of 1.5 mV and 2.4 mV. For 1.5 mV threshold level (Fig. 13 (a) below), multiple *NIM* outputs are triggered indicating a threshold level too low. Since the *CQC* system is designed to detect only one avalanche event per overbias pulse, a threshold level corresponding to only one *NIM* output per pulse is acceptable. This is achieved by increasing the threshold level until the multiple *NIM* peaks cease to exist. Fig. 13 (b) shows the *NIM* output and the avalanche signal for a threshold level of 2.4 mV.

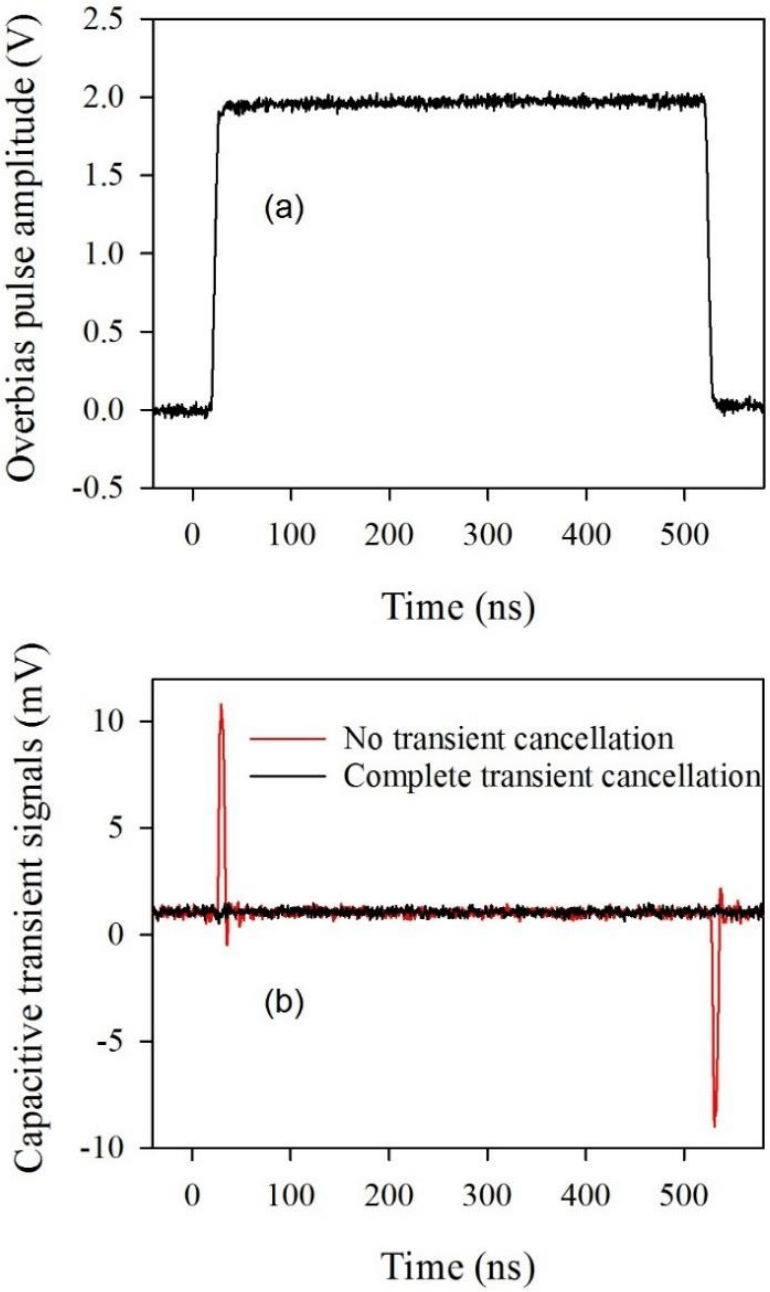

Fig. 12 (a) Overbias pulse applied to DUT using an AC overbias pulse amplitude of 2V. (b) Dummy capacitor is tuned to zero to see the capacitive transients from the DUT (Red line).

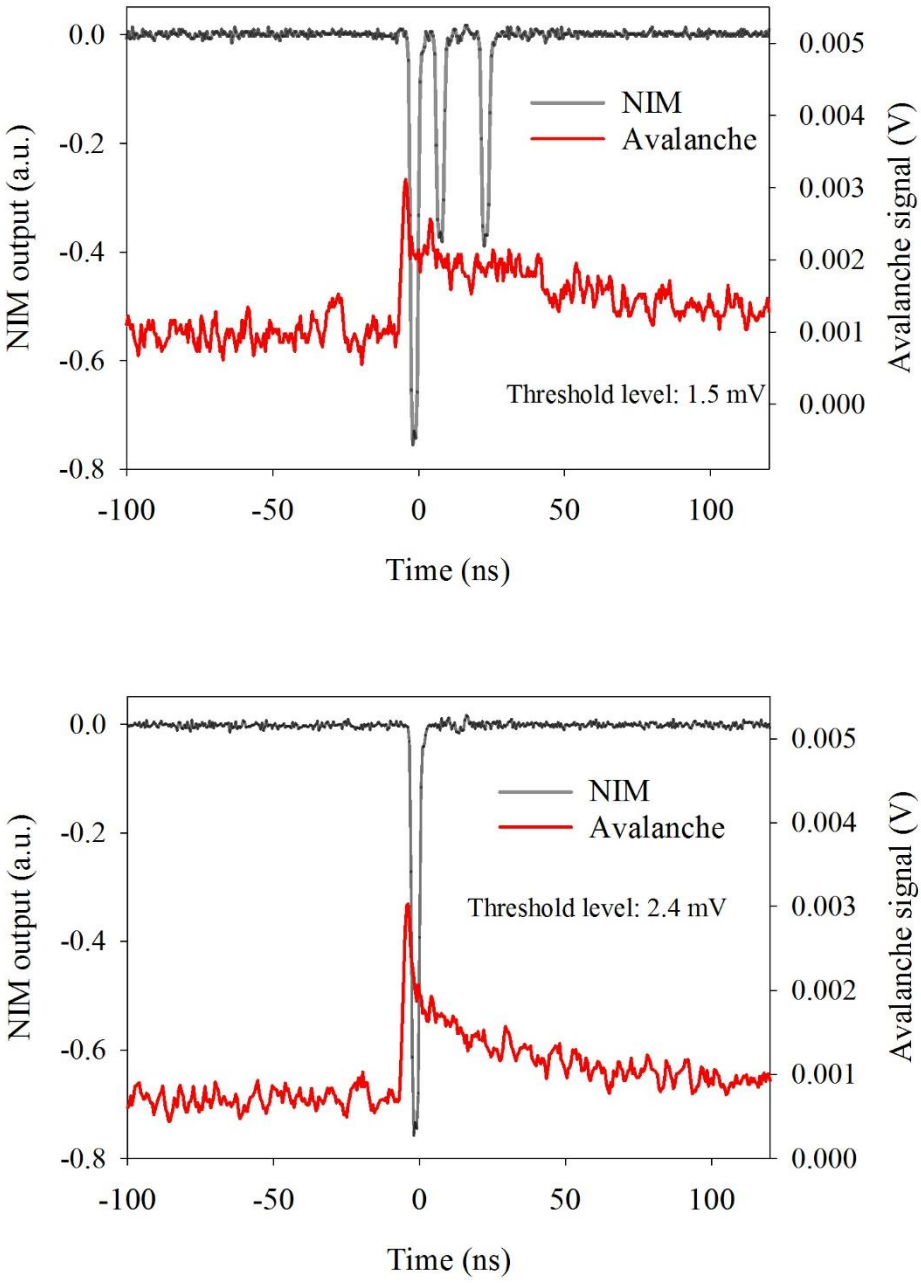

Fig. 13 Avalanche and NIM signals recorded for a DC bias level of 11.22 V, AC overbias amplitude of 2 V and (Top) threshold level of 1.5 mV and (bottom) 2.4 mV.

The detailed construction of ECL logic discriminator and *NIM* pulse generation is listed in ref. [4].

3.4.5 Multichannel analyser measurements

Figure 14 shows the schematic for recording the time histograms of dark counts for Geiger mode photodiodes. The Multi-Channel Analyser (MCA) is used in conjunction with a Time to Amplitude Converter (TAC) for this purpose. An ORTEC-567 Time to

Amplitude Converter (*TAC*) is triggered by the *NIM* output from a discriminator sensing the avalanche signals from the *DUT*.

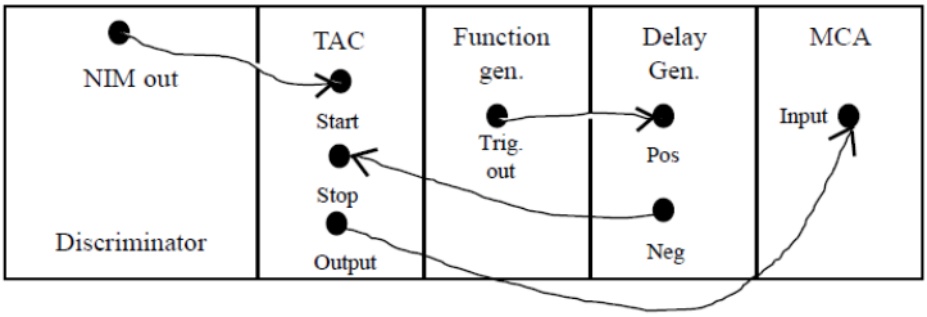

Fig.14. Schematic representation for recording the time histogram of avalanche breakdown events.

The trigger output from the Agilent 81101-A pulse generator is delayed by an ORTEC 416 A gate delay generator. The time delay can be adjusted by a three position toggle switch adjustable in the range of 1.1 - 110 μs. The *TAC* is used to record the breakdown events between a start and stop time specified to its inputs. The time range can be set from 20 to 200 ns with a maximum multiplication factor of 10000. The start to stop time amplitude conversion is accomplished by the *TAC* once a start signal is supplied and the stop pulse has arrived within a specified time range here referred to as *TAC* range. This enables the *TAC* to convert the time between the avalanche event and the delayed trigger to a voltage pulse shown in Fig.15. The amplitude of the voltage signal is directly proportional to the time lapse between the avalanche signal and the delayed negative trigger. The typical *TAC* range has been set to 2 μs in our measurements. The timing diagram for this operation is shown in Fig. 15. The *MCA* then samples the *TAC* output into one of its 16384 bins and generates a histogram of events where the output is represented as number of avalanche events per bin (see Fig. 16). The time scale used by the *MCA* (T_{MCA}) and time per bin (T_{bin}) can be calculated according to Eq. (11-12).

$$T_{MCA} = \frac{n \times T_{TAC}}{16384} \tag{11}$$

$$T_{bin} = \frac{T_{TAC}}{16384} \tag{12}$$

Where *n* is the number of channels which ranges from 1 to 16384. The resolution of each time bin is typically 122 ps. The MCA histogram is simply the time sampling of the magnitude of *TAC* voltage pulses scaled between 0-10 V. The *MCA* time is scaled such that the first avalanche pulse is stored in the largest bin number hence the time axis is finally reversed to record the time distribution of avalanche breakdown events. Figure 16 illustrates how the *MCA* samples the *TAC* outputs and stores the data as counts per bin.

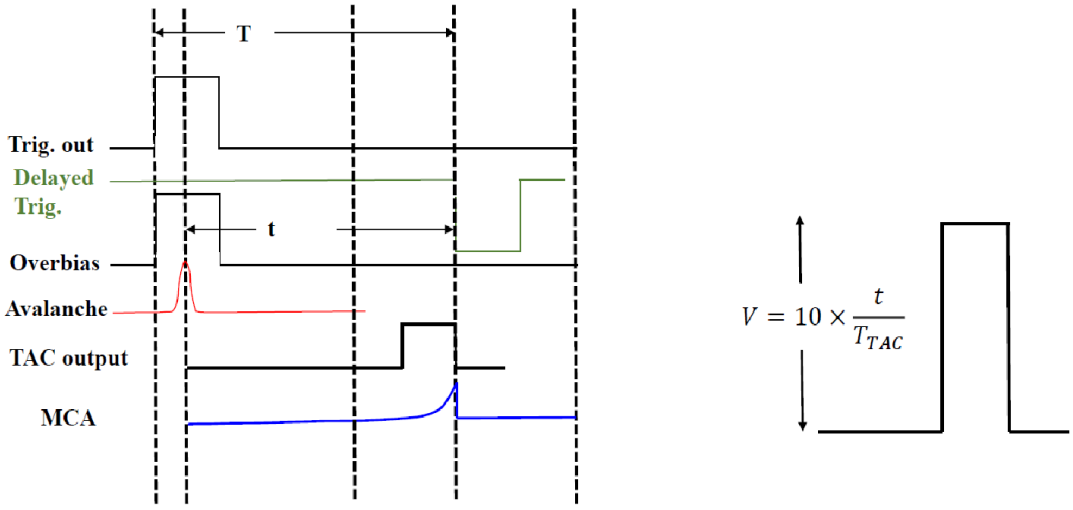

Fig.15 Timing diagram explaining the operation of registering the time distribution of dark counts. The TAC output is also shown as a voltage pulse with a magnitude of ***10 X t/T*** $_{TAC}$ *[6].*

In addition to dark count events, photon counting events are also registered using an *MCA* based setup in a similar manner described in this section. The only difference in this case is that the device is illuminated with a light source.

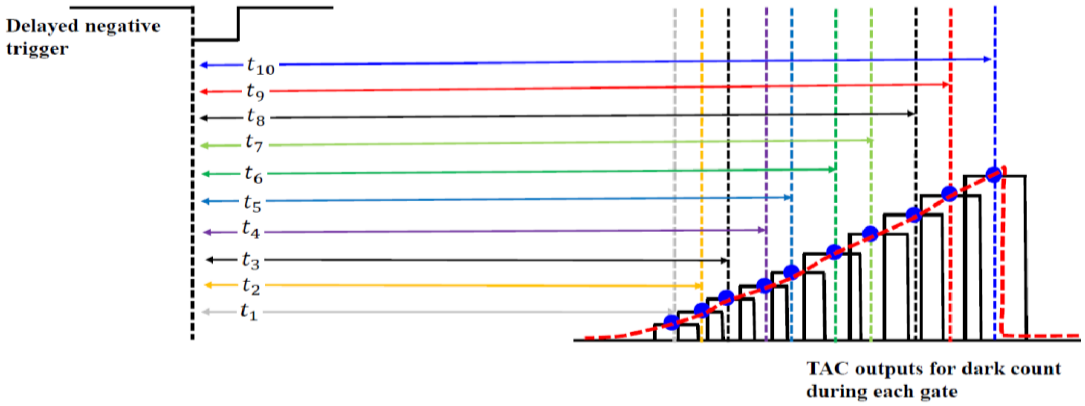

Fig.16 Illustration of the sampling process of MCA. The time delay between individual avalanche events during an active gate and the delayed negative trigger is converted by the TAC to voltage pulses. The overall sampling of the voltage pulses leads to a sampled MCA output which is shown as thick red dashed line.

References

[1] Ben. G Streetman, S. Banerjee, *Solid state Electronic Devices*, 7th Edition, Pearson, 2015.

[2] Application Note, *Keysight Technoloiges,* Impedance measurement handbook, 6th Edition.

[3] M. H. Woods, W. C. Johnson, and M. A. Lampert, "*Use of a Schottky barrier to measure impact ionization coefficients in semiconductors*," *Solid-State Electronics*, vol. 16, no. 3, pp. 381–394, Mar. 1973.

[4] Ph.D Thesis, S.J. Dimler, The University of Sheffield, 2010.

[5] S. J. Dimler, J. S. Ng, R. C. Tozer, G. J. Rees, and J. P. R. David, "Capacitive Quenching Measurement Circuit for Geiger-Mode Avalanche Photodiodes," *IEEE Journal of Selected Topics in Quantum Electronics*, vol. 13, no. 4, pp. 919–925, Jul. 2007.

[6] ORTEC Time to amplitude converter operating manual, https://www.ortec-online.com/-/media/ametekortec/manuals/567-mnl.pdf

Chapter 4

Device Fabrication

This chapter details the fabrication of mesa diodes studied in this thesis. A detailed overview of cleanroom process fabrication is provided for linear and Geiger mode mesa diodes studied in this thesis. A detailed description of SU-8 passivation procedure, UV-Photolithography using contact aligners, thermal vacuum evaporation of metal contacts and wire bonding is given. A detailed micro-process fabrication flowchart for mesa diodes is given which covers the stages from wafer cleaving up to wire bonding and packaging.

4.1 Fabrication of $Al_{0.85}Ga_{0.15}As_{0.56}Sb_{0.44}$ linear mode avalanche photodiodes

$Al_{0.85}Ga_{0.15}As_{0.56}Sb_{0.44}$ APDs used in this work were fabricated from epitaxial layers grown on InP substrate through molecular beam epitaxy (MBE) at the National III-V Epitaxy Facility at the University of Sheffield. The device layer structure is shown in Fig. 1. A 100 nm thick unintentionally doped layer of AlGaAsSb was sandwiched between oppositely doped AlGaAsSb layers, where Be and Te were used as a *p*-type and *n*-type dopants respectively. The *p* and *n* doped AlGaAsSb layers are 300 nm and 100 nm thick respectively. The top 100 nm *p*- doped InGaAs and the lower 1000 nm *n*-doped InGaAs layers are heavily doped to facilitate the electrical probing of the device through the metal contacts. The subsequent 300 nm *p*-doped AlGaAsSb and *n*-doped 100 nm AlGaAsSb layers along with the intrinsically doped 100 nm *i*-AlgaAsSb layers are used to create the *p-n* junction. The thickness of each layer and corresponding doping is selected to provide a full depletion at zero reverse bias and to predict the breakdown voltage of the APD. A calculation of the electric field and depletion width based on Poisson's equation is detailed in Appendix. A.

100 nm p - $In_{0.47}$ $Ga_{0.53}$ As, 5 x $10^{18}cm^{-3}$
300 nm p - Al_{1-x} Ga_x AsSb, 2 x $10^{18}cm^{-3}$
100 nm i - Al_{1-x} Ga_x AsSb
100 nm n - Al_{1-x} Ga_x AsSb, 2 x $10^{18}cm^{-3}$
1000 nm n- $In_{0.47}$ $Ga_{0.53}$ As, 5 x $10^{18}cm^{-3}$
n- InP substrate

Fig.1 Device layer structure for AlGaAsSb mesa APDs used in this work. x=0.15 corresponds to the Ga composition used in this work.

Device fabrication was carried out through standard UV-photolithography and wet chemical etching. Following are the detailed steps taken to fabricate the devices.

1. Hand cleave the bare wafer by applying force gently along the crystal axis. Alternatively use a computer-controlled scriber for cleaving a small piece.
2. Clean the piece using iso-clean acetone, n-butyl and Iso Propyl Alcohol (IPA).
3. Post bake the sample on a hot plate at 373 K for 30 s.
4. Spin resist (BPRS-200/SPR-350) at 4000 rpm for 30s followed by bake at hot plate for 60 s at 373 K. UV photolithography is done using UV-300 or UV-400 mask aligner. Lithography mask should be cleaned prior to the lithography process. IPA can be sprayed to clean the mask and if the stains/residual resist are stubborn, a rinse in Decon-90 solution and IPA is helpful. UV lithography is needed to transfer the resist patterns onto wafer which is important for device fabrication. Following are the steps needed to ensure successful wafer patterning using a UV-300 lithography mask aligner (Fig. 2)
    - Turn on the power supply to mask aligner and lamps. Wait for 20 minutes for the UV lamp to stabilise. Turn the nitrogen pressure toggle switch to ON position (1).
    - Tun on the mask aligner (2).
    - Clean the mask plate before mounting it on vacuum bracket and tighten the adjustment screws (3).
    - Put the sample on chuck, slide it back under the mask holder and lift it towards the mask using the chuck height adjustment lever.
    - Using the eye piece adjustment handle (4), focus on the sample and align it under the mask using the three-dimensional adjustment micro-dials (5).

- Once the sample is perfectly aligned, ensure a contact between the sample and mask and set the exposure time. For UV-300 aligner, an exposure time of 14 s for the top metal contact deposition should be fine using SPR-350 resist.
- Set the exposure time using the adjustment dials (6) and commence exposure using the push button (7).

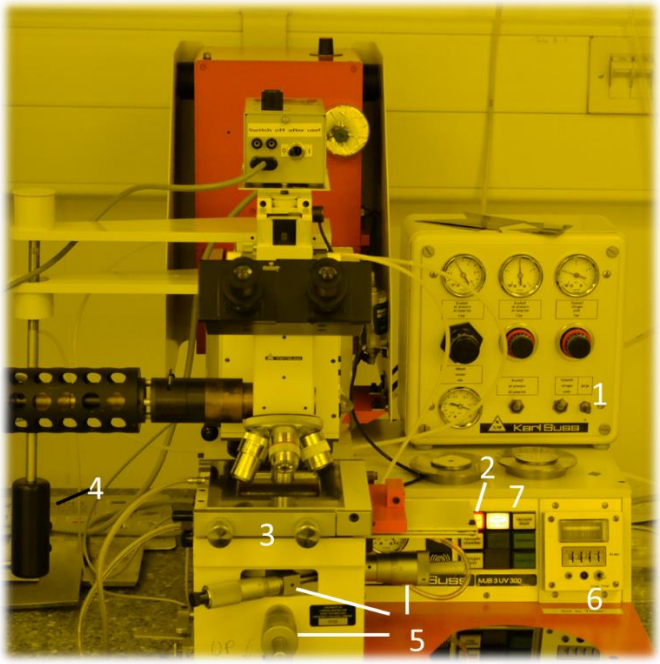

Fig. 2 Suss- UV lithography mask aligner. 1: Nitrogen pressure toggle switch, 2: Power push button for aligner, 3: mask holder bracket and adjustment screws, 4: Handle for eye piece adjustment, 5: Three-dimensional mask plate adjustment, 6: Exposure time adjustment dial, 7: Exposure push button.

- Align the sample under the correct mask layer and expose for a suitable time which can be determined through trial. Alignment features on mask aid in assessing the suitability of lithography time such that under-exposure and over-exposure are best avoided.
- Develop the sample in a suitable developer solution. MF26A and MF26A diluted with DI water are used for resists BPRS-200 and SPR-350 respectively.
- Clean the sample with De-Ionised Water (DIW). Acetone is best avoided at this stage as it washes away the developed pattern.
- Inspect the sample for possible over or under exposure. Under exposure can be assessed by coloured pattern on the sample while over exposure is obvious from the overlapping elongated features on mask. In case of under-exposure the pattern

should be washed away with acetone and the process should be started from step 3.

- In case the pattern is developed well, proceed to the metallisation stage. Pre-clean the sample with nitrogen plasma (ashing) to remove residual photoresist. Clean for typically 3’18”.

5. Load samples to thermal evaporator (Edwards Model 360A). The chamber should be pumped down to atleast 6×10^{-6} mbar which requires around 120 minutes. Carefully load Au and Ti coils into the boats/coils in the chamber and close the chamber to ensure proper pumping. The roughing pump will not pump the chamber down if bell jar is not closed/placed properly. Start pumping down.

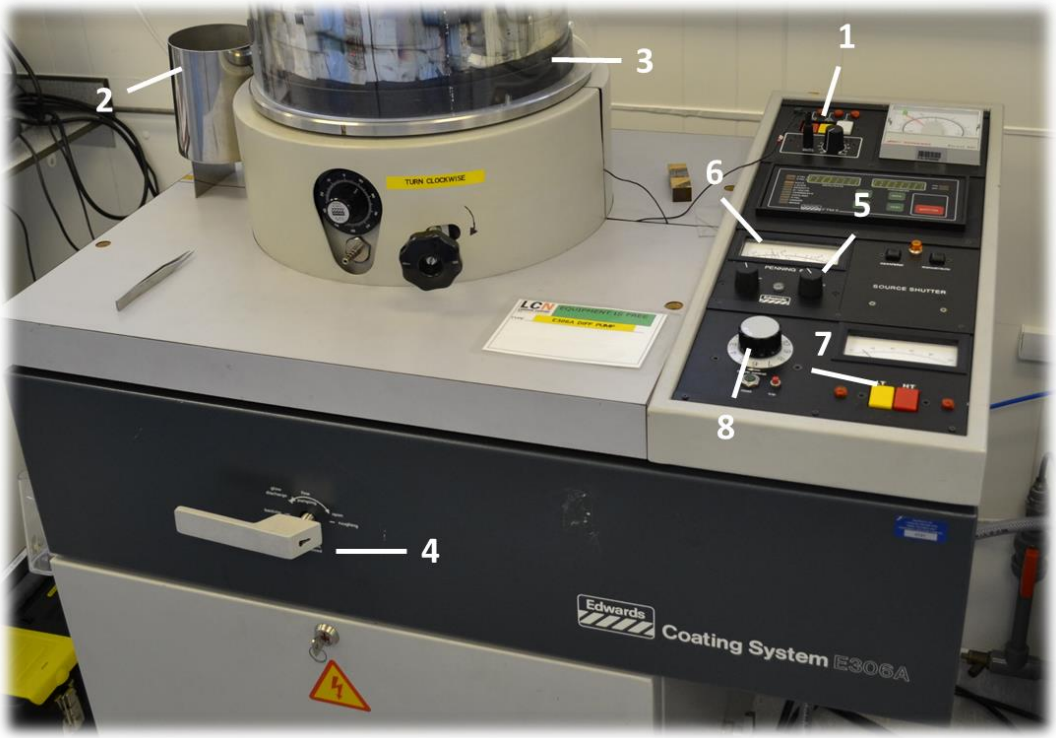

Fig. 3 Snapshot of Edwards 306-A thermal vacuum evaporator. 1: Air admit and diffusion valve, 2: Chrome funnel for liquid nitrogen, 3: Bell jar, 4: Vacuum pump lever, 5: Penning gauge, 6: Vacuum gauge, 7: LT coil current source, 8: Variac LT coil current adjustment knob.

The stepwise evaporation procedure is shown as follows

- Turn the oil diffusion pump ON (1).
- Pour in liquid nitrogen using the side chrome funnel to the left of bell jar (2). Two complete fills are normally enough for the diffusion pump to reach operating vacuum. This process takes around 20 mins.

- Open the air admit valve to allow the chamber to reach the atmospheric pressure.
- Remove the implosion guard and bell jar carefully (3).
- Fit the coils/boats in the chamber. The coils should be loaded with clean Ti and Au wires. Clean both the coils and wires in *n*-butyl solution and flush with nitrogen gun.
- Load the samples and close the bell jar. Put the implosion guard back. Depress the air admit valve.
- Turn the lever clockwise to backing position (4) and read the pressure from vacuum gauge (6). Now the roughing pump can be engaged.
- Slowly turn the lever anti-clockwise to roughing position. A successful indicator of the roughing pump being engaged is that the crystal monitor unit moves closer to the sample when the level is turned to roughing position.
- Pour in liquid nitrogen until the funnel overflows. Allow the chamber to pump down to 6×10^{-6} mbar which takes around 2 hours.
- Select the position of LT selector switch to the appropriate coil position. Ti should be evaporated first followed by Au.
- Push the LT button (7).
- Start increasing the current through the respective coils by turning the variac control knob (8). Ti should start melting around 35 A while Au start melting at around 20 A.
- Monitor the thickness of the deposition which should increase with increase in the current flow. The rate at which the deposition is carried for Ti corresponds to a 20 nm deposition in approximately 3 minutes.
- After the desired thickness is deposited, turn the variac knob fully off and allow the coils to cool down for 5 minutes.
- Repeat the process for Au.
- Turn LT OFF.
- Open air admit valve.
- Move the lever (4) clockwise to backing position.
- Remove the implosion guard and bell jar. Clean the bell jar with Aqua regia and sodium hydroxide and hydrochloric acid solution for removing Au and Ti respectively.

- Carefully refit the clean bell jar and close the air admit valve.
- Turn the level clockwise to roughing position and then anticlockwise to backing position.

6. Following a successful metal deposition, perform lift off using acetone solution. The bell jar should be cleaned with aqua regia solution. If the metal deposition is fine, the lift off should be very quick and clean. Otherwise use ultrasonic bath to remove stubborn gold patches.
7. Cover the metal contact with resist and etch the wafers into circular mesa diodes. Aqueous citric acid solution diluted with iso-clean hydrogen peroxide and hydrochloric acid diluted with aqueous hydrogen peroxide are used to etch the InGaAs contact layers and quaternary AlGaAsSb layers respectively. The etch recipe is given as:
    - Hydrous citric acid + Hydrogen peroxide solution for etching InGaAs contact layers: Mix citric acid with *DIW* in ratio of 1:1. As a guideline, 10 ml of *DIW* and 10 g of hydrous citric acid should give approximately 12 ml of aqueous citric acid solution. This solution should then be diluted with iso-clean hydrogen peroxide in volumetric ratio of 2:1. Etch rate on InGaAs is around 50 nm/min.
    - Dilute pure hydrogen peroxide with *DIW* in volumetric ratio of 1:9. Following the dilution, the hydrogen peroxide solution should be mixed with hydrochloric acid and *DIW* (in volumetric ratio of pure hydrochloric acid: hydrogen peroxide solution: *DIW*:: 1:2:10). This recipe should have an etch rate of ~ 100 nm/min however the best approach to ensure complete etching of the quaternary layer is to observe the colour change from light green (InGaAs) to a mix of brown + green (quaternary). The colour of the sample begins to fade away from centre of the first and turns back light green when the quaternary is etched away. Care must be taken to dip the sample immediately into hydrochloric acid etchant following InGaAs etch as exposure to atmospheric conditions leads to oxidation of AlGaAsSb due to highly oxidising nature of Al.

In our work [1] we found that the etch recipe based on citric acid chemistry achieves a relative anisotropy of the wet etch process in comparison with another recipe based on sulphuric acid (H_2SO_4: diluted H_2O_2:DIW in volumetric ratio of 1:8:80). In an SEM image was taken for two pieces of the same wafer etched with the two respective

chemistries and it was observed that the citric acid based chemistry gives a less severe undercut in the etch profile. Figure 4 shows the SEM image of the coupons.

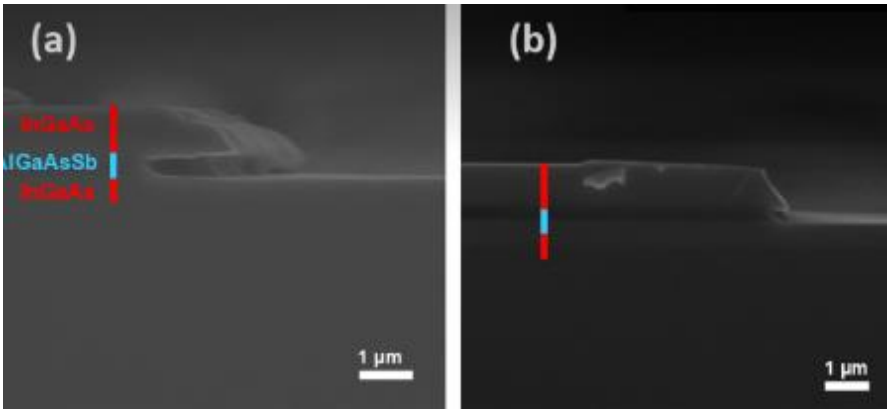

Fig.4 (a) Wafer etched with sulphuric acid (1:8:80) chemistry. The colour bar on the figure shows the various device layers. (b) wafer etched with citric acid (2:1) chemistry. Figure printed with permission of Lucas Pinel from The University of Sheffield. SEM image taken by Jonathan Petticrew from The University of Sheffield.

Following the etch process a negative resist SU-8 is used to preserve the mesa sidewalls. SU-8 is a negative permanent photoresist (contrary to non-permanent positive resists SP-350, PMGI and BPRS 220). SU-8 is used to passivate the mesa sidewalls of our diodes. Following steps should be adopted to ensure a smooth and even sidewall passivation with SU-8.

- Perform a 3-stage sample clean process i.e. dip in *n*-butyl followed by acetone and rise with IPA. Flush with a nitrogen gun.
- Bake the sample on a hot plate for 1 min at 100°C.
- Spin SU-8 at 3000 rpm on the spin coater for 30 s.
- Bake the sample for 1 min at 65°C followed by 95°C for 3 min.
- Use mask aligner, UV_300 to expose the sample for 2 s using the appropriate mask layer.
- Bake the sample for 1 min at 65°C followed by 95°C for 1 min.
- Develop SU8 in developer for 1 min and then rinse in IPA for 1 min. Flush the sample dry with a nitrogen gun.
- Expose to UV300 light from aligner (with no mask) for 240 seconds.

- SU-8/5 should result in a thickness of 5.5 μm when spun at 3000 rpm using the above procedure. SU-8/2 should result in a 1.7 μm thick profile when done using the above procedure.

8. A second round of metallisation is required to facilitate the electrical probing of the device. We use the similar process of metallisation as detailed earlier in this section. A different mask set is used for grid contact metallisation. Titanium and gold Ti/Au (20/200) nm are used as metal contacts. Au is used because it is a low resistance contact layer in connecting to external circuits. Ti is the most commonly used thin film adhesive layer for Au onto semiconductor substrates [2] and it acts as a diffusion barrier between Au and the semiconductor layer preventing Au diffusion into the semiconductor layer [3].
9. Perform lift off and test devices using a standard *I-V* characterisation to ensure devices are working. This step is also used to assess the yield of the fabrication process and suitable measures should be taken to optimise the yield. Yield of the device fabrication process can be assessed by doing standard *I-V* measurement. The ratio of number of devices exhibiting a standard *I-V* with an acceptable dark current level (to be defined) the total number of devices on wafer is quantified as microfabrication process yield. The photolithography mask facilitated fabrication of devices in unit cells, where each unit cell comprised of mesa diodes of four different diameters, 420, 220, 120 ad 75 μm. Fig. 5 shows two (2) such unit cells.

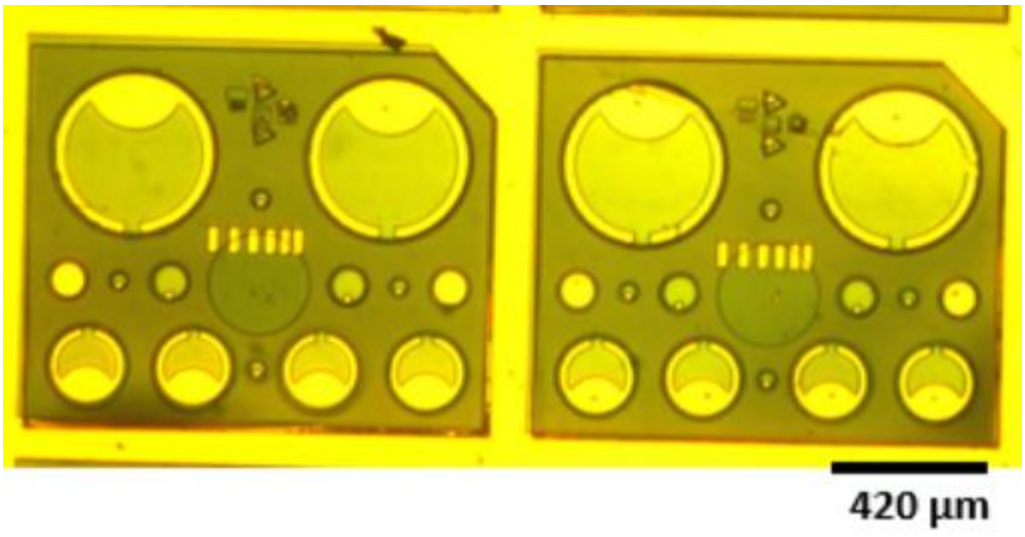

Fig.5 Snapshot of processed mesa diodes. Four unit cells can be seen. Diodes of different mesa sizes can be seen. The blackish appearance of the semiconductor surface is due to SU-8. n-type electrical contact is deposited in a grid pattern.

4.2 Fabrication of Geiger mode mesa diodes with remote bondpads

Following are the detailed steps needed to fabricate mesa diodes used for Geiger mode characterisation. Hand cleave the bare wafer by applying force gently along the crystal axis. Alternatively use a computer-controlled scriber for cleaving a small piece.

1. Clean the piece using iso-clean acetone, n-butyl and Iso Propyl Alcohol (IPA).
2. Post bake the sample on a hot plate at 373 K for 30 s.
3. Spin resist (BPRS-200/SPR-350) at 4000 rpm for 30s followed by bake at hot plate for 60 s at 373 K.
4. UV photolithography using UV-300 or UV-400 mask aligner. Lithography mask should be cleaned prior to the lithography process. IPA can be sprayed to clean the mask and if the stains/residual resist are stubborn, a rinse in Decon-90 solution and IPA is helpful.
5. Align the sample under the correct mask layer and expose for a suitable time which can be determined through trial. Alignment features on mask aid in assessing the suitability of lithography time such that under-exposure and over-exposure are best avoided.
6. Develop the sample in a suitable developer solution. MF26A and MF26A diluted with de-ionised water are used for resists BPRS-200 and SPR-350 respectively.
7. Clean the sample with De-Ionised Water (DIW). Acetone is best avoided at this stage as it washes away the developed pattern.
8. Inspect the sample for possible over or under exposure. Under exposure can be assessed by coloured pattern on the sample while over exposure is obvious from the overlapping elongated features on mask. In case of under-exposure the pattern should be washed away with acetone and the process should be started from step 3.
9. In case the pattern is developed well, proceed to the metallisation stage. Pre-clean the sample with nitrogen plasma (ashing) to remove residual photoresist. Clean for typically 3’18”.
10. Load samples to thermal evaporator (Edwards Model 360A). The chamber should be pumped down to at least 6×10^{-6} mbar which requires around 120 minutes. Carefully load Au and Ti coils into the boats/coils in the chamber and close the chamber to

ensure proper pumping. The roughing pump will not pump the chamber down if bell jar is not closed/placed properly. Start pumping down.

11. Following a successful metal deposition, perform lift off using acetone solution. The bell jar should be cleaned with aqua regia solution. If the metal deposition is fine, the lift off should be very quick and clean. Otherwise use ultrasonic bath to remove stubborn gold patches.
12. Cover the metal contact with resist and etch the wafers into circular mesa diodes. Aqueous citric acid solution diluted with iso-clean hydrogen peroxide (70% pure) and hydrochloric acid diluted with aqueous hydrogen peroxide are used to etch the InGaAs contact layers and quaternary AlGaAsSb layers respectively.
13. Following the etch process, a second round of metallisation is required to facilitate the electrical probing of the device. Use the similar process of metallisation from step.4 through step.11.
14. Perform lift off and test devices using a standard *I-V* characterisation to ensure devices are working. This step is also used to assess the yield of the fabrication process and suitable measures should be taken to optimise the yield.
15. Silicon Nitride (SiN_x) to be deposited for aiding the adhesion of remote bondpads to the semiconductor contact layers. Plasma Enhanced Chemical Vapor Deposition (PECVD) process is used to deposit the dielectric at 423 K.
16. Electrical contacts should be opened using Reactive Ion Etching (RIE) using a gaseous mixture of $CHF_3 + O_2$. To aid the etching of dielectric, HMDS adhesive is used promote adhesion of resist to dielectric surface.
17. Deposition of remote bondpads to facilitate device packaging and bonding. For the ease of packaging and wire bonding, thick Ti/Au (40/400 nm) layers should be deposited. Using the suitable mask layers, follow the steps 4 through 11 for bondpads deposition.
18. Following contacts deposition, perform lift off using a warm acetone solution followed by rinse in IPA and DIW.
19. Perform standard *I-V* measurements to ensure the devices exhibit acceptable characteristics. For the ease of cleaving isolation trenches were facilitated by the lithography mask. There are regions where no dielectric is deposited to avoid cracks in the dielectric layers during the cleaving process. Fig. 6 shows a snapshot of two fabricated devices with remote bond pads and isolation trenches between them.

Following the device cleaving, wire bonding and packaging is performed to facilitate *DCR* characterisation.

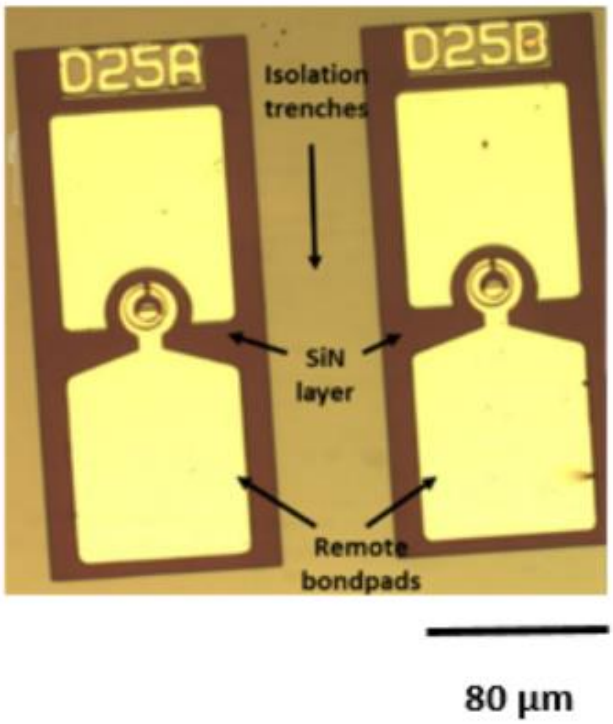

Fig.6 A snapshot of the processed device showing remote bondpads, SiN deposition and isolation trenches.

20. For packaging, cleave small piece from the processed wafer. Use gold epoxy to to mount the pieces onto a metal header in a furnace which maintains the temperature at 203 K.
21. Mount the sample on holder plate of the ball wire bonder (Kulicke & Soffa, Model 4255 manual bonder). Complete the bonds from the sample piece to leadframe and test the header for faulty electrical connection. In case of broken wire bonds, repeat the bonding process. For *DCR* characterisation, mesa diodes are packaged on metal headers using wire bonding machine, Kulicke & Soffa Model 4522 wire bonder. Following are the steps to ensure successful wire bonding.
    - Clean the metal header using *n*-butyl and flush with a nitrogen gun.
    - Clean sample with *n*-butyl followed by *DIW* and flush with nitrogen.
    - Put gold epoxy on metal header and mount the sample piece carefully and place in furnace at typically 393 K.
    - Turn the wire bonder ON. Following steps should be completed

a. Turn light-ON.
b. Turn Negative Electronic Flame-Off ON
c. Set the hot plate temperature to 373 K.

- Mount the sample on place holder in the wire bonding machine.
- Adjust the Loop (L), Search (S), Tail (T), Power (P), Time (T) and Force (F) settings. Typical values of for the parameters are
    a. Bond 1: *TPTF:* 7424
    b. Bond 2: *TPTF:* 7121

Fig. 7 shows the schematic of the packaged and bonded device.

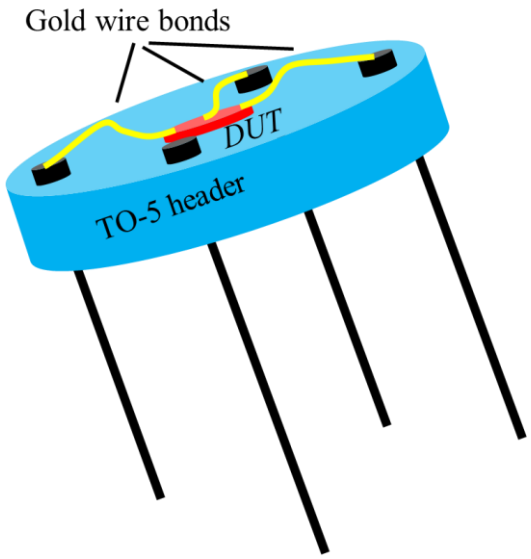

Fig. 7 Schematic drawing of a DUT mounted on a TO-5 4 pin header. The wire bonds connect the DUT to the header pins

Based on the fabrication details of small size avalanche photodiodes in this section, I have created a process flow chart covering the entire cleanroom details starting from wafer cleaving and cleaning right up to wire bonding and packaging. Fig. 8 shows the micro-fabrication process flow chart.

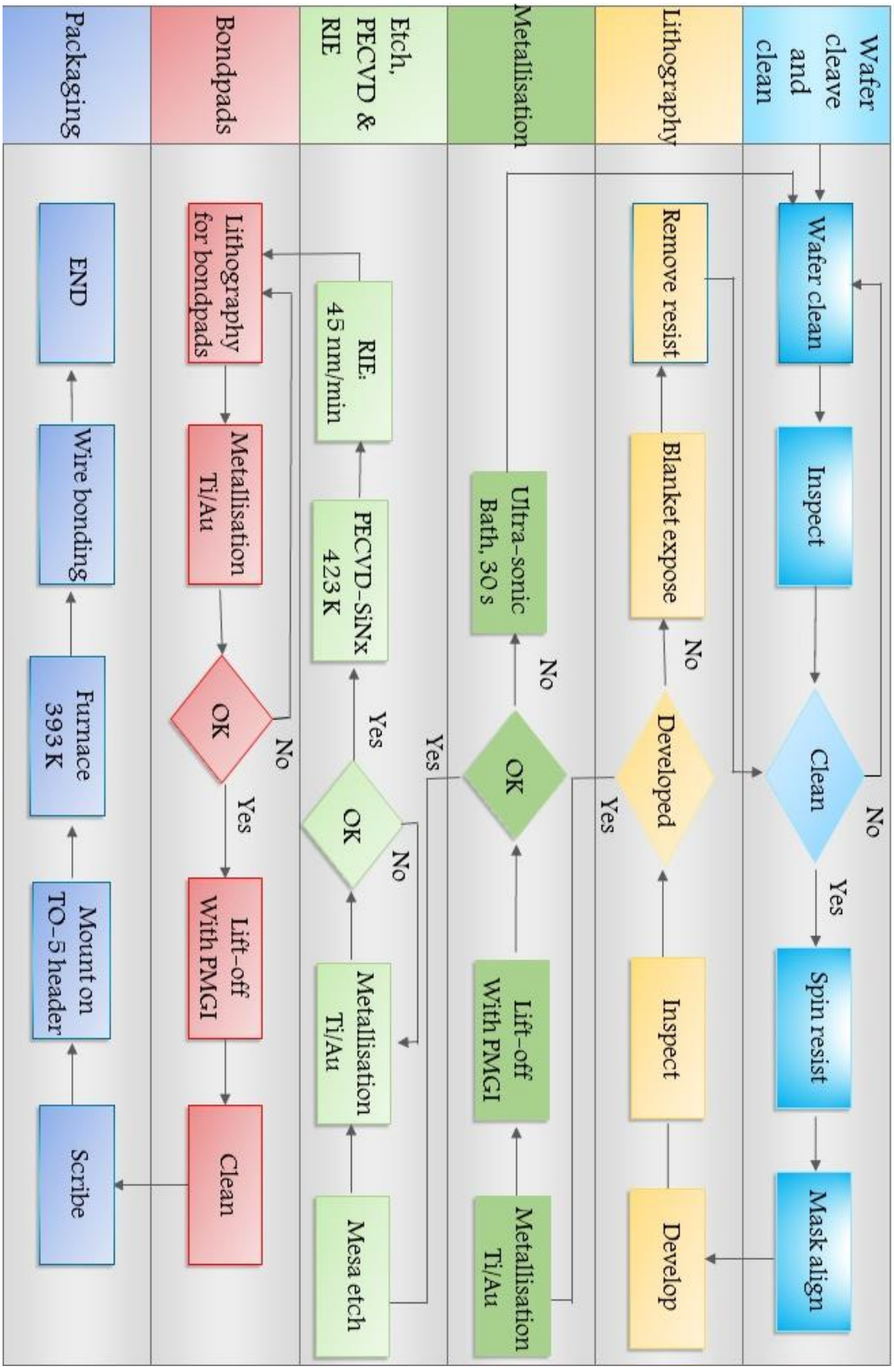

Fig. 8 Process flow for microfabrication of Geiger mode avalanche photodiodes.

References

[1] L. Pinel, J. Petticrew, X. Zhou, S. Abdullah, C.H. Tan and J.S. Ng, "*Improving wet etching of InGaAs/AlGaAsSb avalanche photodiodes*", 16th International Conference on Molecular Beam Epitaxy, Monpellier, Sep. 2016, France.

[2] Basudev Lahiri, Rafal Dylewicz, Richard M. De La Rue, and Nigel P. Johnson, "*Impact of titanium adhesion layers on the response of arrays of metallic split-ring resonators (SRRs),*" Opt. Express 18, 11202-11208 (2010).

[3] Anna Szerling, Piotr Karbownik, Adam Łaszcz, Kamil Kosiel, Maciej Bugajski, "*Low-resistance p-type ohmic contacts for high-power InGaAs/GaAs-980 nm CW semiconductor lasers*", Vacuum, 82, 977-981 (2008).

Chapter 5

Temperature and temporal stability of avalanche gain in $Al_{0.85}Ga_{0.15}As_{0.56}Sb_{0.44}$ avalanche photodiodes

Optical tomography, optical fibre communications, photon counting, autonomous driving and biomedical applications including fluorescence detection and laser distance mapping [1] are applications where APDs are used. In these applications, it is highly desirable for APDs to maintain constant gain. Commercial APDs for these applications [2] make use of temperature stabilisation or voltage compensation circuitry to maintain constant gain. From the operational perspective, it is beneficial for APDs to have a stable gain over time to minimise the dependence on external circuitry. Avalanche gain and breakdown voltages in most semiconductor materials change with temperature and the temperature stability of these parameters is one of the most crucial performance metrics of APDs. Moreover, in practical applications utilising APDs, a good temporal stability of avalanche gain is highly desirable to maintain a constant output signal for subsequent sensing and processing.

This chapter details the evaluation of temperature and temporal stability of avalanche gain in $Al_{0.85}Ga_{0.15}As_{0.56}Sb_{0.44}$ avalanche photodiodes. Device fabrication was carried out using standard wet chemical etching and UV-Photolithography as detailed in Sec.4.1 in Chapter 4. The temperature and temporal stability of $Al_{0.85}Ga_{0.15}As_{0.56}Sb_{0.44}$ APDs is investigated at temperatures of 24 to 80 °C. Avalanche gain and breakdown voltage measurements were preformed and temporal variations in gain were monitored for the temperature range specified. A comparison was then made with the state-of-the-art technology in III-V and Si APDs.

Device characterisation began with standard current-voltage (*I-V*) at room temperature under dark conditions.

5.1 Current-voltage (*I-V*) characterisation

I-V characterisation was used to assess the presence of surface leakage, uniformity of breakdown voltage and imperfections in device fabrication process. *I-V* characterisation was performed with the experimental setup described in chapter 3, section 3.1.

Forward *I-V* data was used to extract series resistance arising from possible metal adhesion issue or lack of dopant activation in the top *p*-InGaAs contact layers. Fitting from forward *I-V* data from 220 μm diameter mesa device yielded a series resistance of 15 Ω and an ideality factor, n = 1.68 indicating the presence of generation-recombination currents in the diode. Fig. 1 shows the result.

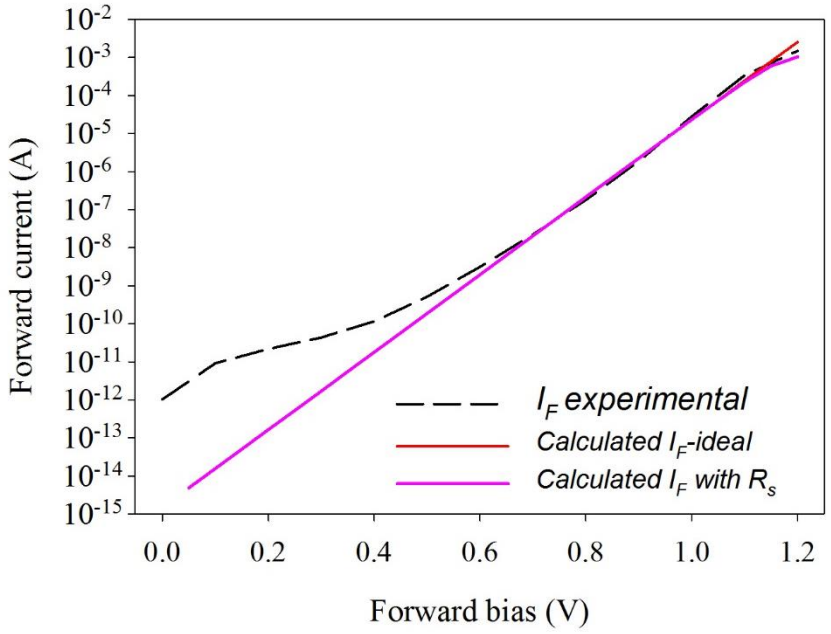

Fig.1 Forward current data for 220 um mesa device (black dashed line) fitted with Eq (1) chapter 3. Red line shows the fitted ideal forward current and pink line shows the fitted forward current with series resistance effect.

Reverse *I-V* data was used to assess device breakdown voltage, surface leakage and bulk current densities. Fig. 2 shows current densities from devices with diameters of 120, 220 and 420 μm. The current densities do not scale perfectly with device area indicating

presence of a perimeter leakage currents. The results are consistent with observations made on current densities of mesa diodes using thin avalanche layer of $Al_xGa_{1-x}As_{0.56}Sb_{0.44}$ (x = 0.05 – 0.15) [3]. The influence of series resistance R_s can be seen by comparing the calculated ideal I_F (red solid line) and calculated I_F with R_s. The forward current starts saturating at higher forward bias values and results in potential drop. Series resistance can impede the flow of current between metal-semiconductor or semiconductor-semiconductor interface. The deviation of the calculated I_F from experimental data can be explained by the presence of possible surface and bulk leakage. Surface states e.g. dangling bonds where abrupt termination of the sidewalls can induce changes to the crystal structure, can act as defect sites. Similarly bulk leakage can arise from imperfections in semiconductor bulk: possibly being caused by non-optimum growth conditions.

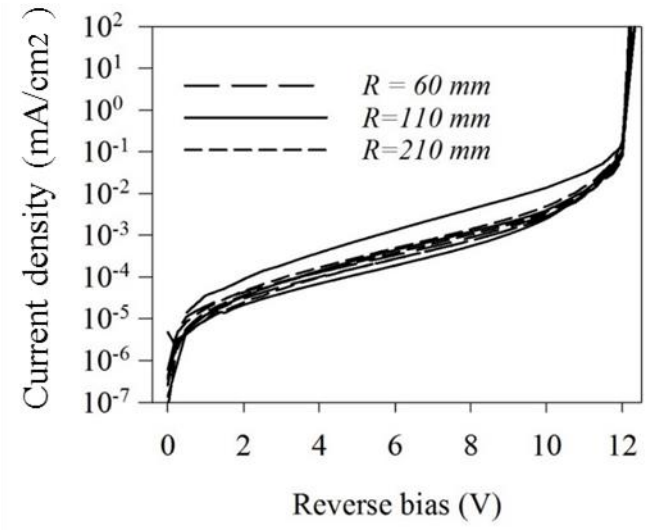

Fig.2 Dark currents normalised to bulk area for three different mesa radii shown in legend.

Uniformity in the devices across wafer was assessed by recording dark currents for a number of devices of same size selected randomly from wafer. Fig. 3 shows the results for dark currents recorded for 27 different APD samples (D = 120 um) across the wafer. The results indicate a uniform breakdown but some spread in the dark currents at lower biases for the APDs.

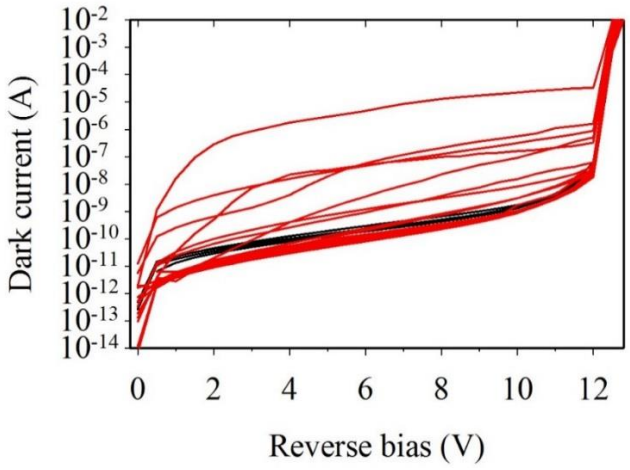

Fig. 3 Dark currents recorded for D=220um mesas. 27 different APDs were probed. Black solid lines represent the devices selected for subsequent gain and responsivity measurements.

The spread in the dark currents prior to the breakdown voltage is another indicator of surface leakage component in the devices, as discussed previously. Nonetheless the devices in Fig. 3 show uniformity in the abrupt increases in the dark currents after 12 V indicating uniform breakdown voltages. The breakdown voltage of 12.44 ± 0.01 V is deduced from Fig. 5. The standard deviation is extracted from the set of data points representing the breakdown voltages of 27 different APDs tested in Fig. 3. In mesa devices, laser spot size illuminating the sidewalls can induce the edge breakdown effect and it was therefore mandatory to investigate the edge breakdown effect and laser spot size.

5.2 Laser spot size check

The APDs were illuminated with a 633 nm He-Ne laser. Light from the laser source was mechanically chopped at a fixed frequency of 180 Hz. Using a commercial Si photodiode (BPX-65) it was verified that the laser power (46 μW for our measurements) remained stable within ±0.5% for the typical duration of measurements. Phase sensitive detection (see chapter 3 section 3.3.1) was used to minimise the influence of device dark current. The laser spot size was focussed onto the optical window of mesa APD. The photocurrent values were recorded with the phase sensitive detection technique for APDs with different diameters to evaluate the laser spot size.

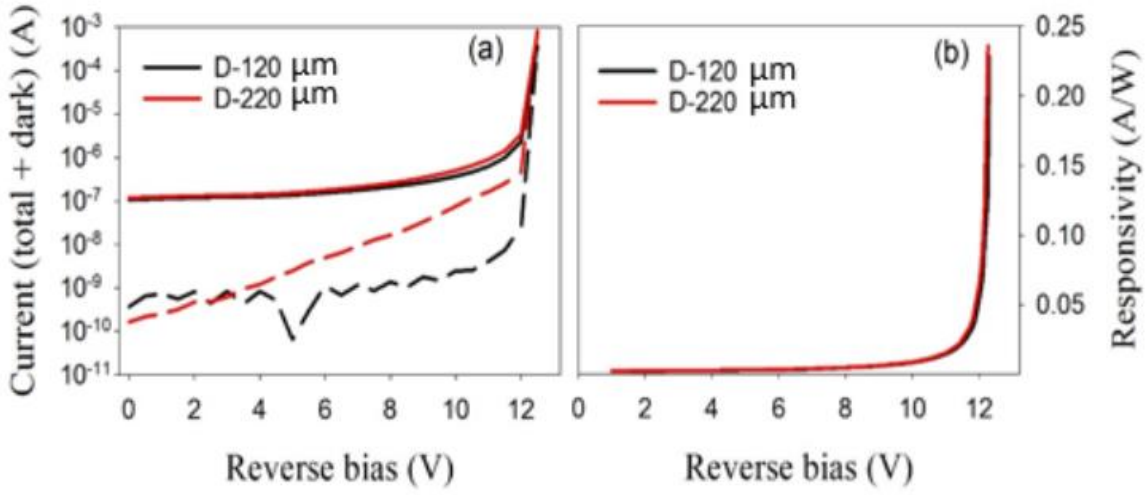

Fig.4 (a) I-V data showing dark (dashed lines) and total currents (solid lines) for 120 µm and 220 µm mesa devices. (b) Photoresponsivity data for the two mesa APDs at 633 nm.

The photocurrent and responsivity values for devices with different sizes yielded similar values as shown in Fig. 4 and the devices breakdown at similar reverse bias values. These results suggest that the laser spot size is smaller than 120 μm. To confirm that the devices did not suffer from a premature edge breakdown effect, a laser was focussed on different positions on the mesa diodes. The result and procedure for this check are shown in the following section.

5.3 Premature edge breakdown check

Micro-plasmas arising from growth imperfection or subsequent semiconductor processing can result in formation of localised ionisation hot-spots in the avalanche. These hot spots are isolated regions where high current densities can flow and can appear at well-defined reverse bias [4]. Locally enhanced electric field at these centres can result in premature edge breakdown (*PEB*) that leads to inconsistent gain between devices and non-uniform breakdown voltages. Although analyses of the dark *I-V* from Fig. 3 demonstrated uniform breakdown voltages for a number of devices ($D=220\ \mu m$), a detailed investigation of the premature edge breakdown effect would be necessary to completely rule out the effect. To rule out the *PEB* effect, a mesa diode from the set of APDs shown in Fig. 3 ($D=220\ \mu m$) was illuminated with a focussed laser beam at different positions on the optical window. Fig. 5 shows the schematic of the illumination of mesa diode with laser illumination spots in the centre and close to sidewalls.

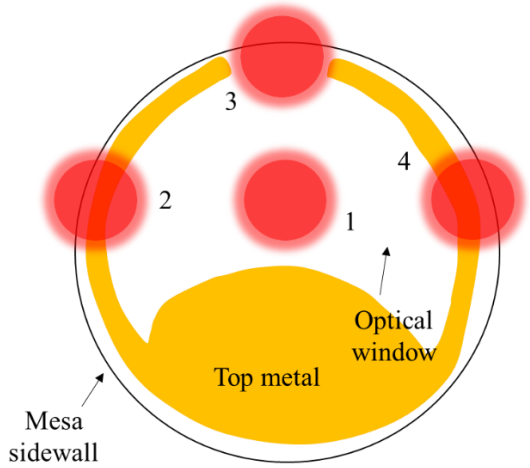

Fig. 5 Schematic of a D = 220 um mesa diode illuminated with a focussed laser beam on different points. 1: Centre of the optical window. 2, 3, 4: Close to mesa sidewalls. A laser power of 1.6 uW is used.

Using the experimental procedure described in sec. 3.3, a *DC* laser power of 1.6 μW, and a series resistor of 1kΩ (see Fig. 5 chapter 3) was used for collecting the photocurrent data from the *DUT*.

Breakdown voltage was extracted from the gain data by extrapolating reciprocal avalanche gain to zero when plotted as a function of reverse bias. The procedure was repeated for illumination points 1, 2, 3 and 4 as shown in Fig. 5. The data for multiplication gain as a function of reverse bias is shown in Fig. 6. Data in Fig. 6 show that the avalanche gain as a function of reverse bias increases rapidly when the reverse bias increases beyond 10 V. The data shows uniformity for the four different illumination points along the mesa optical window. No signs of an early breakdown is observed in any of the datasets. The reciprocal of the avalanche gain is shown in the bottom pane of the figure.

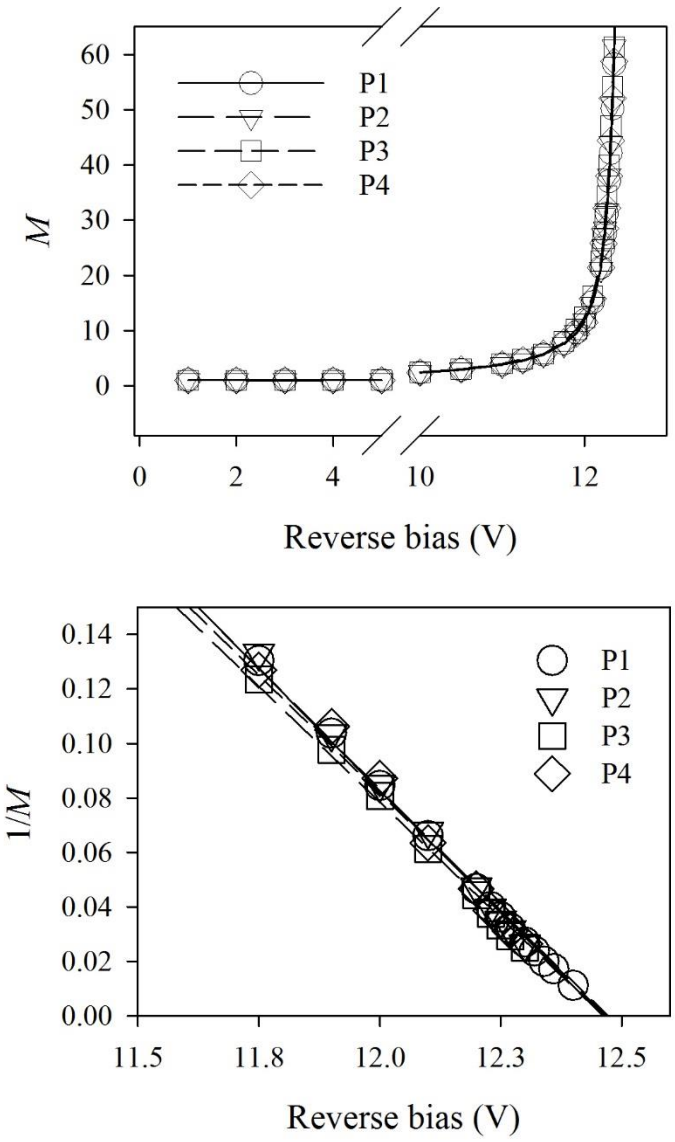

Fig. 6 (Top) Avalanche gain as function of reverse bias for 220 µm mesa diode. Legend shows the data for laser beam illuminating points 1, 2, 3 and 4 as shown in Fig. 7. Lines are shown as guide to eye (Bottom) Reciprocal of avalanche gain versus reverse bias for different datasets corresponding to laser illumination on different points along the mesa optical window and sidewalls, as demonstrated schematically in Fig. 7. Dashed lines show linear fitting.

Uniform breakdown voltage of 12.45 ± 0.02 V is extracted from the data and is within the standard deviation of breakdown voltage of 12.44 ± 0.01 V deduced earlier from *I-V* characterisation in Fig. 5. The error reported for the data sets here is extracted from the statistical standard deviation of the data sets for the breakdown voltages extracted for different *DUTs*. The data in Fig.6 supports the observation that uniform breakdown voltages observed for different device sizes of the *DUT* (as shown in Fig. 3 and 4) is free from *PEB* effect. Consequently 4 APDs of $D = 220\ \mu m$ (named APD-1 through 4)

including the one (APD-3) characterised for *PEB* effect in Fig. 5 were selected from the set of 27 APDs characterised in Fig. 3 for subsequent gain characterisation.

5.4 Temperature dependence of avalanche gain

Using the photocurrent values for APD-1 through 4, avalanche gain, *M* as a function of reverse bias was calculated from by the ratio of photocurrent to the primary photo-current. The procedure for gain calculation is detailed in chapter 3, section 3.3. Fig. 7 shows the *M* versus *V* for the four selected APDs.

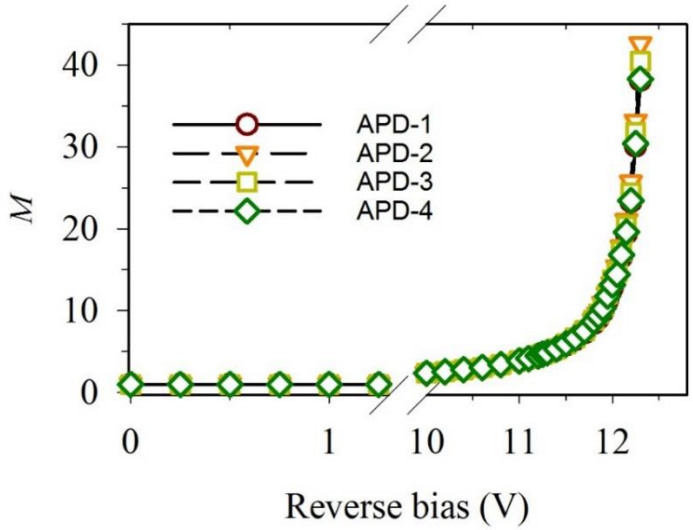

Fig. 7 M versus reverser bias for the four selected APDs at room temperatures. Lines are shown only as a guide to the eye.

Again, the devices show good uniformity in the gain curves and show an abrupt increase in the gain after 12 V. High gain was measured on all devices. For example, a gain of 42 was recorded for a reverse bias of 12.31 V for APD-3. At 11.9 V, room temperature, APD-1 through 4 show *M* values of 10.46, 10.28, 10.38 and 9.90 respectively. The breakdown voltage corresponds to the reverse bias value where the gain approaches infinity. As before, extrapolating 1/*M* as a function of reverse bias to 0 provides an accurate measure of the breakdown voltage and repeating the measurements at different temperatures can yield the temperature coefficient of avalanche breakdown C_{bd}.

5.5 Temperature dependence of breakdown voltage

The setup described in section 3.3 was used for the measurements. The measurements were carried out at temperatures ranging from 24°C to 80°C. The breakdown voltages at respective temperatures were extracted by plotting 1/*M* and extrapolating 1/*M* to zero. Fig. 8 shows the results for the four selected APDs. At 24, 40, 60 and 80°C the mean breakdown voltages for the APDs are 12.41, 12.43, 12.47 and 12.50 V (σ^2: 0.02, σ_x: 0.04) respectively. The increase in temperature increases the breakdown voltage and reduces the avalanche gain which can be explained by the reduction in the impact ionisation probability due to increased phonon scattering at higher temperatures. At higher temperatures, the phonon scattering increases energy loss leading to a smaller population of hot carriers that can initiate impact ionisation events. Subsequently high electric fields (and hence higher voltage) are needed to offset the carrier cooling induced by inelastic scattering. The temperature coefficient of avalanche breakdown C_{bd} can be calculated for each device by plotting the breakdown voltage as a function of temperature using the data in Fig. 10. A standard linear equation of the form $y = mx + c$, was used to fit the breakdown versus temperature data for each device where the breakdown voltage is the dependent variable, y and the slope of the equation, m represents the temperature C_{bd}. Fig. 8 shows the result.

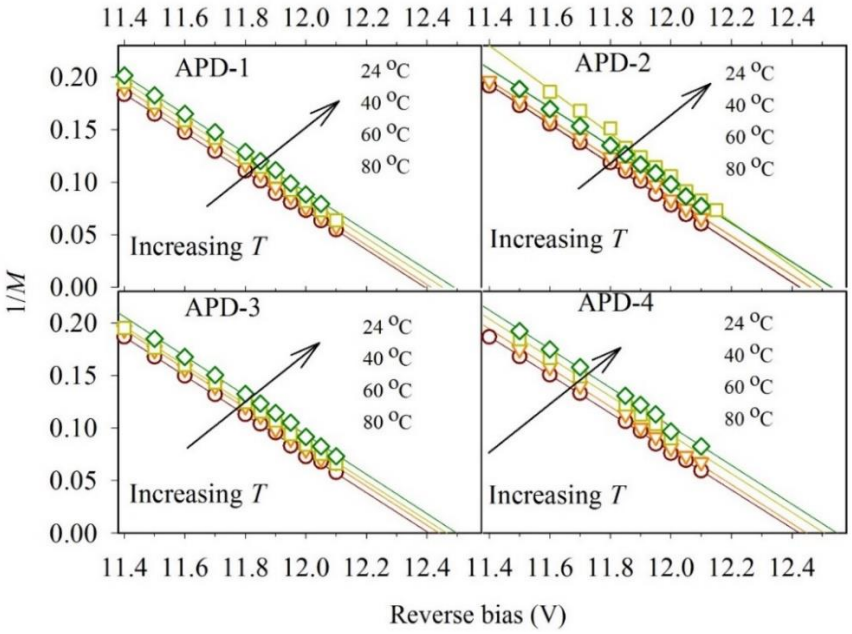

Fig. 8 1/M values for the selected APDs as function of reverse bias values. Solid lines represent linear fit to the experimental data points.

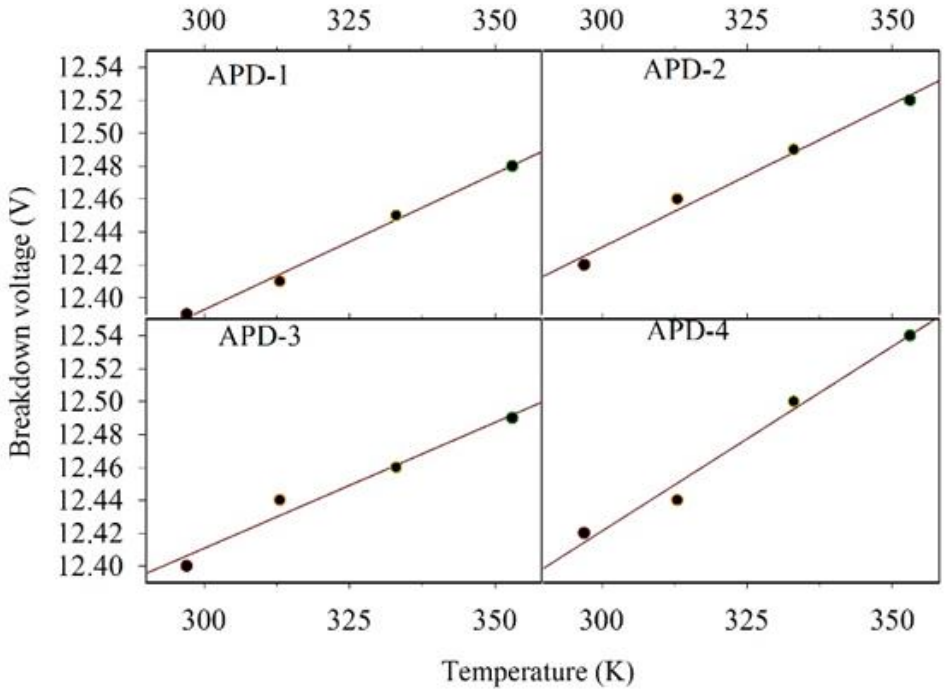

Fig.9 Breakdown voltages as a function of temperature for APD-1 through 4. Dots represent the breakdown voltages extracted from data in Fig. 10. Solid line: linear fit to the experimental data.

Fig. 9 shows that the temperature coefficient of avalanche breakdown, C_{bd} for APD-1 through 4 is 1.59, 1.71, 1.59 and 1.9 mV/K giving a mean C_{bd} of 1.69 ± 0.146 mV/K. The error in the C_{bd} is calculated from the statistical standard deviation of the data set for the 4 *DUTs* considered in Fig. 9. The reduced temperature dependence of avalanche breakdown and can be explained by the following:

- Influence of alloy scattering effect.
- Reduced phonon scattering for thin multiplication layers at high electric field.
- Possibly a large phonon energy can also lead to a reduced temperature dependence of phonon scattering.

Perturbation of crystal potential resulting from random positioning of substituting atomic species in relevant crystal sub-lattice is known as alloy scattering. This can only happen in compound ternary or quaternary alloys (such as $Al_{0.85}Ga_{0.15}As_{0.56}Sb_{0.44}$ of this work) as their structure is formed by replacing some atoms in one of the crystal sub-lattices. Analysis of alloy disorder potential by Ong et al [9] has indicated that a significant alloy scattering in ternary alloy of $AlAs_{0.56}Sb_{0.44}$ (because of the difference in covalent radii of Sb and As atoms) could have been responsible for the reduced C_{bd} of *p-i-n* APD based on

this alloy. The ratio between As and Sb is same in $AlAs_{0.56}Sb_{0.44}$ and $Al_{0.85}Ga_{0.15}As_{0.56}Sb_{0.44}$ [12] diodes of this work and therefore a reduced C_{bd} is not surprising for diodes in this work. Binary alloys such as InP do not have the alloy scattering potential and therefore they tend to have higher C_{bd} values compared to similar thicknesses of ternary or quaternary alloys with dominant alloy scattering (for an optimum molar composition).

High electric fields are typical for thin avalanche layers and carriers can gain energy more rapidly from the high electric fields while undergoing less phonon scattering before impact ionising. As carriers cross the multiplication region, they continuously gain energy from electric field and lose energy by various phonon scattering mechanisms. At very high electric fields however, the number of phonon scattering events prior to impact ionisation reduce [5]. This phenomenon makes the breakdown voltage in thin avalanche layers less temperature sensitive. Phonon scattering can be quantified in terms of phonon occupation number, n_p which can be related to the phonon energy, E_p and temperature as

$$n_p = \frac{1}{\exp(\frac{E_p}{k_B T} - 1)} \quad (1)$$

Where a larger phonon energy can possibly explain the reduced temperature dependence of phonon scattering rate. For instance, $Al_{0.8}Ga_{0.2}As$ [6] with 300 K phonon energy of 46 meV (cf. $36.25 + 1.83x + 17.12x^2 - 5.11x^3$ [7] where x is Al composition) demonstrates a reduced C_{bd} for a range of avalanche layer thicknesses (200 nm – 1 μm) in comparison with similar thickness of InP which shows a room temperature phonon energy of 43 meV [7].

In summary the combination of dominant alloy scattering and reduced phonon scattering at high electric fields for thin layers are likely the effects are believed to be responsible for the reduced temperature dependence of avalanche breakdown and multiplication gain. A larger phonon energy can also possibly explain the suppressed temperature dependence of avalanche breakdown in thin avalanche layers of $Al_{0.85}Ga_{0.15}As_{0.56}Sb_{0.44}$.

5.6 Comparison with literature

Temperature dependence of V_{bd} has been reported for ternary alloys $Al_xGa_{1-x}As$ [8], $Al_{0.52}In_{0.48}P$ [9], $AlAs_{0.56}Sb_{0.44}$ [11] and quaternary AlInAsSb [13]. $Al_{0.52}In_{0.48}P$ was found to have a C_{bd} value even smaller than AlGaAs and the variation in C_{bd} values for different

semiconductor systems reviewed by Ong et al [9] (and references therein) were attributed to the difference in the alloy scattering between the materials studied. For instance, InP (w = 130 nm) was reported to have a C_{bd} value higher than InAlAs (w = 110 nm) [10] by a factor of 2.4 due to the absence of alloy scattering in InP alloy. Recently $AlAs_{0.56}Sb_{0.44}$ [11] was found to have the lowest C_{bd} value (0.95 mV/K and 1.47 mV/K for 80 nm and 230 nm thick layers respectively) compared to previously reported III-V semiconductors of similar thicknesses. The works mentioned here attribute the reduced C_{bd} value to the dominance of temperature independent alloy scattering effect.

Zhou et al [12] reported a C_{bd} of 0.86 - 0.91 mV/K for 100 nm thick $Al_{0.85}Ga_{0.15}As_{0.56}Sb_{0.44}$ layer in the temperature ranges of 77 K – 297 K. Recently $Al_{0.6}In_{0.4}As_xSb_{1-x}$ *p-i-n* diodes grown on GaSb substrates [13] have been reported with low values of C_{bd} of 2.5 mV/K (890 nm thick multiplication layer). Grezsik et al [14] have reported a high C_{bd} of 30 mV/K for 700 nm thick avalanche layer of $Al_xGa_{1-x}As_ySb_{1-y}$ (x= 0.40) lattice matched to GaSb substrate. Table 4.1 lists the comparison of C_{bd} values reported for III-V materials recently.

Table 1: Comparison of temperature coefficient of avalanche breakdown for different semiconductor material systems

Device	***W*** **(nm)**	**Substrate**	C_{bd} **(mV/K)**	**Reference**
$Al_{0.6}In_{0.4}As_xSb_{1-x}$ *p-i-n*	890	GaSb	2.5	[13]
InP *p-i-n*	130	InP	6	[10]
InAlAs *p-i-n*	100	InP	2.5	[10]
$AlAs_{0.56}Sb_{0.44}$ *p-i-n*	80 – 230	InP	0.95 – 1.47	[11]
$Al_{0.85}Ga_{0.15}As_{0.56}Sb_{0.44}$ *p-i-n*	110	InP	0.86 – 0.91	[12]
$Al_{0.85}Ga_{0.15}As_{0.56}Sb_{0.44}$ *p-i-n*	110	InP	1.60	This work
$Al_{0.40}Ga_{0.60}As_xSb_{1-x}$ *p-i-n*	700	GaSb	30	[14]

Though the work of Zhou et al [12] reported on the lowest C_{bd} so far, it is relevant to mention here that the temperature range studied by Zhou et al (77 – 296 K) was lower than our studied range. At lower temperature, the phonon occupation number drops and hence the phonon energy. The dependence of phonon occupation energy on temperature and its influence on the temperature coefficient of avalanche breakdown is however not

the aim of this research. Nonetheless we confirm that low C_{bd} can be consistently obtained in $Al_{0.85}Ga_{0.15}As_{0.56}Sb_{0.44}$ APDs at higher temperature ranges (296 – 353 K). Reduced temperature sensitivity of avalanche breakdown is desirable in APDs as it ensures a steady avalanche signal and hence electrical output is maintained which is critical for APD applications such as laser range finding, distance mapping, autonomous vehicle and fluorescence imaging. This reduced temperature sensitivity of avalanche breakdown in $Al_{0.85}Ga_{0.15}As_{0.56}Sb_{0.44}$ is important for practical applications where a temperature stability of avalanche gain is highly desirable to operate the device in rugged conditions. For example, commercial APDs make use of a complex temperature stabilisation circuitry to maintain a constant gain [15]. The temperature insensitivity of $Al_{0.85}Ga_{0.15}As_{0.56}Sb_{0.44}$ APDs highlight their potential applications in simplifying the operational complexity of APD circuitry.

Using the gain data from the four $Al_{0.85}Ga_{0.15}As_{0.56}Sb_{0.44}$ APDs at 11.9 V, a comparison is made with two commercial Si APDs (S-5345, S-6045). The data for the Si APDs was extracted from their data sheets and is presented in Fig. 10. As temperature increases, gain reduces in all six APDs with a smaller reduction in M for the four $Al_{0.85}Ga_{0.15}As_{0.56}Sb_{0.44}$ APDs compared to S-5345 and S-6045.

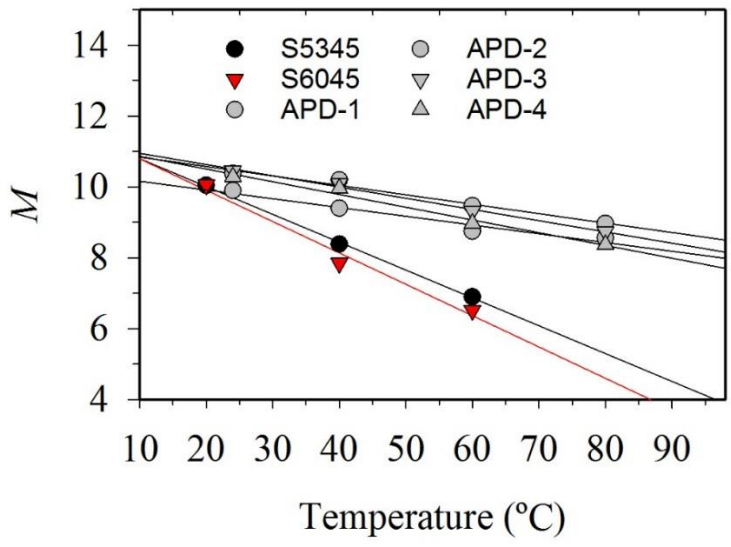

Fig. 10 Comparison of M vs T for AlGaAsSb APDs and commercial Si APDs. Solid lines are linear fitting to experimental data. The M values for the commercial devices are extracted from their data sheets.

A reduction in *M* for S5345, S6045 and $Al_{0.85}Ga_{0.15}As_{0.56}Sb_{0.44}$ APDs by 45, 52 and 15% respectively was observed when the temperature is increased from 24 to 80 °C. For most wide bandgap III-V semiconductors such as GaAs, InP, AlGaAs increasing the temperature leads to an increased inelastic scattering between carriers and lattice vibrations which reduces the energy gained by the carriers from external electric field for their impact ionisation. Subsequently the impact ionisation coefficients and hence the avalanche gain reduces with increasing temperature. With such a minimal reduction in gain, there is a potential in simplifying the APD operational circuitry if using the $Al_{0.85}Ga_{0.15}As_{0.56}Sb_{0.44}$ APDs. Since these devices are grown on InP substrates, they have the potential to replace InP and InAlAs as avalanche material for APDs operating at 1550 nm telecom window (if InGaAs is used as absorber). In practical applications, a temporally stable avalanche gain is necessary to yield constant avalanche gain signal. The temporal stability of avalanche gain is also therefore an important metric for assessing the robustness of our APDs.

5.7 Temporal stability of avalanche gain

For the temporal stability measurement of avalanche gain the four selected APDs were reverse biased at 11.9 V (*M* = 10 at room temperature) and the gain values were collected over 12.5 minutes at 24°C, 40°C, 60°C and 80°C. The data was recorded using experimental setup for recording *LIA* values over time described in chapter 3. The measured data as shown in Fig. 11 is presented as percentage fluctuations compared to mean *M* at corresponding temperatures at a reverse bias of 11.9 V. For each device, two sets of data were recorded at each temperature. Over the studied temperature ranges, no clear drift in the avalanche gain was observed for any device. The maximum fluctuations in *M* at room temperature is ± 0.5%. This level of fluctuation was similar to that of a commercial Si photodiode indicating a fluctuation of ± 0.5% in the setup. As the temperature is raised, the fluctuations remain within ± 1.1% for all devices over the temperature range studied in this work. APD-1 remains an exception with maximum fluctuation of +1.33% at 80°C.

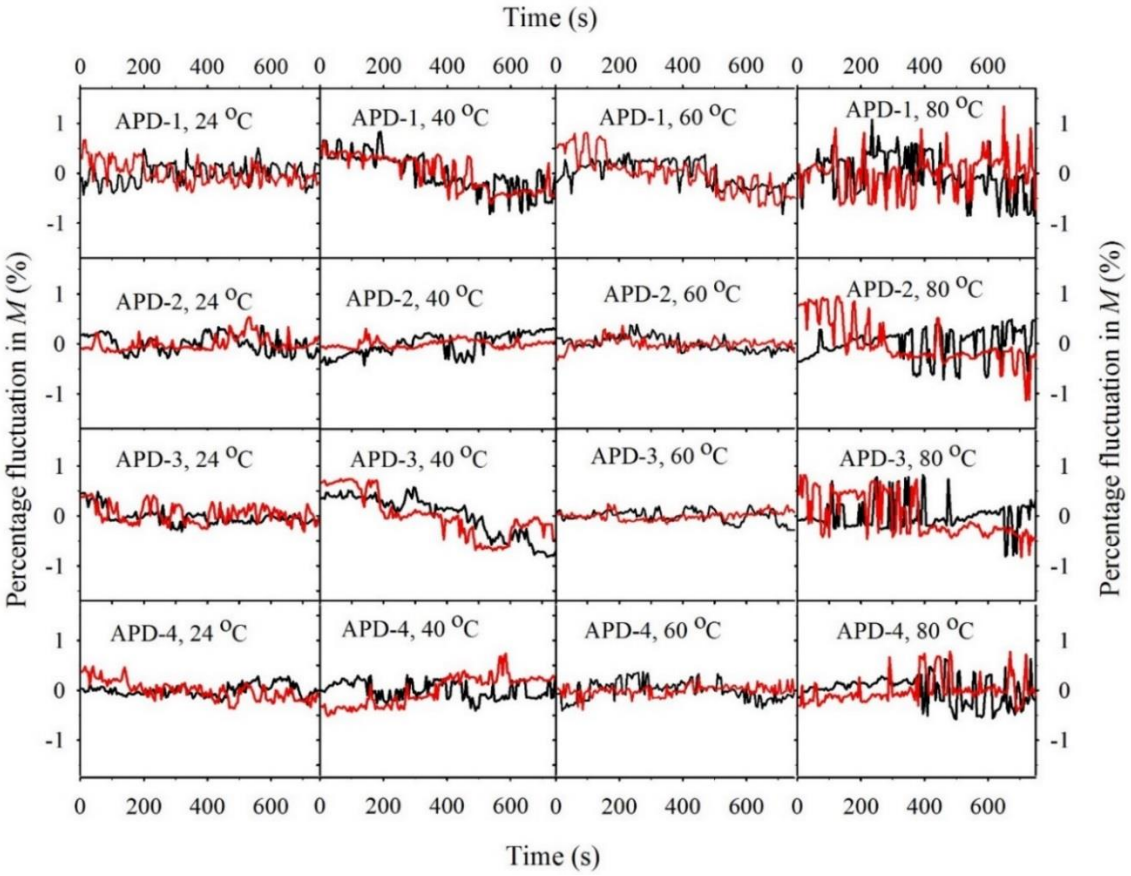

Fig. 11 Percentage fluctuations in M versus time for APD-1 through 4 with reference to mean gain at 11.9 V at temperatures of 24°C, 40°C, 60°C and 80°C. Two data sets were recorded for each device.

Ren [16] and Jones [13] have reported on room temperature temporal stability of multiplication gain for $Al_xIn_{1-x}AsSb$ (x = 0.6, 0.7) avalanche photodiodes grown on *n*-GaSb substrates. They have studied *p-i-n* and separate absorption and multiplication type structures based on AlInAsSb avalanche and absorption layers. As a comparison with our work Ren and Jones reported a maximum error in *M* of 1.7% for $Al_xIn_{1-x}AsSb$ (x = 0.6) and 5.1% for $Al_xIn_{1-x}AsSb$ (x = 0.7) *p-i-n* APDs over a time duration of 2 hours. In a similar test, Jones et al demonstrated a maximum gain error of 7.4% for the separate absorption and multiplication type APD when the device was biased at a reverse bias corresponding to *M* = 13 at 300 K. No clear drift has been observed by Ren and Jones in their studies.

5.8 Dark currents in $Al_{0.85}Ga_{0.15}As_{0.56}Sb_{0.44}$

The studies on temporal stability reported in the previous section were conducted over a varied range of temperatures. The devices have gone through significant number of

measurements including the typically 12.5 minutes for each set of gain measurement. Hence each device was subjected to a measurement time of 100 minutes for temporal stability. Fig. 12 shows the *I-V* data for the four selected APDs before and after the high temperature and gain measurements. No significant thermal degradation was observed in the dark currents of the devices. The data shows the robustness of the dark currents of $Al_{0.85}Ga_{0.15}As_{0.56}Sb_{0.44}$ mesa APDs. This observation suggests the potential of $Al_{0.85}Ga_{0.15}As_{0.56}Sb_{0.44}$ APDs for operation in rugged conditions with superior immunity to temperature variations which is crucial for optical receivers.

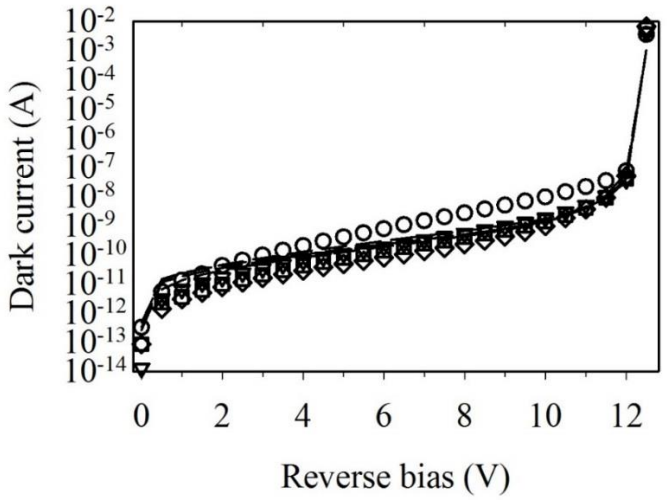

Fig. 12 Dark currents for the four selected AlGaAsSb APDs before (lines) and after (symbols) temperature dependence measurements.

5.9 Summary

In summary we have fabricated avalanche photodiodes based on 100 nm thick avalanche layers of $Al_{0.85}Ga_{0.15}As_{0.56}Sb_{0.44}$. The *I-V* data of *DUTs* from different mesa radii did not scale perfectly with device area indicating a presence of surface leakage currents in the dark currents. Premature edge breakdown effect was not an issue for the device sizes characterised. The average temperature coefficient of avalanche breakdown is 1.6 mV/K which is the smaller than similar thickness of InP and InAlAs by a factor of 3.75 and 1.5 respectively. A superior temperature stability of avalanche gain is demonstrated in comparison with commercial Si APDs. When the temperature is increased from 24 °C to 80 °C, $Al_{0.85}Ga_{0.15}As_{0.56}Sb_{0.44}$ APDs show a reduction in gain of 15% compared to 45%

and 52% for Hamamatsu-S5345 and Hamamatsu-S6045 Si APDs respectively. A good temporal stability of avalanche gain is reported for temperature ranges of 24 °C to 80 °C. A maximum fluctuation in room temperature mean gain (M = 10) of ± 0.5% has been reported at a reverse bias of 11.9V over a time duration of 12.5 minutes. As the temperature is increased the fluctuations remain within ± 1.1% and a maximum fluctuation of 1.33% in mean avalanche gain has been recorded at 80 °C. No temporal drift has been observed in M for any device characterised. No thermal degradation in dark currents has been observed in the devices after gain measurements at elevated temperatures.

References

[1] Application note, Excelitas Technology, Avalanche photodiodes

[2] Application note on single photon detector, "ID220 NIR free-running SPAD," *ID Quantique*., Geneva.

[3] X. Zhou, S. Zhang, J. P. R. David, J. S. Ng, and C. H. Tan, "Avalanche Breakdown Characteristics of $Al_{1-x}Ga_xAs_{0.56}Sb_{0.44}$ Quaternary Alloys," *IEEE Photonics Technology Letters*, vol. 28, no. 22, pp. 2495–2498, Nov. 2016.

[4] D. Decoster and J. Harari, *Optoelectronic Sensors*. John Wiley & Sons, 2013.

[5] D. S. Ong, K. F. Li, S. A. Plimmer, G. J. Rees, J. P. R. David, and P. N. Robson, "Full band Monte Carlo modeling of impact ionization, avalanche multiplication, and noise in submicron GaAs p+-i-n- diodes," *Journal of Applied Physics*, 87,7885, June, 2000.

[6] C. Groves, C. N. Harrison, J. P. R. David, and G. J. Rees, "Temperature dependence of breakdown voltage in $Al_xGa_{1-x}As$," *Journal of Applied Physics*, vol. 96, no. 9, pp. 5017–5019, Oct. 2004.

[7] Ioffe Institute database, Basic properties of AlGaAs at 300 K, http://www.ioffe.ru/SVA/NSM/Semicond/AlGaAs/basic.html

[8] F. Ma, G. Karve, X. Zheng, X. Sun, A. L. Holmes, and J. C. Campbell, "Low-temperature breakdown properties of $Al_xGa_{1-x}As$ avalanche photodiodes," *Applied Physics Letters*, vol. 81, no. 10, pp. 1908–1910, Sep. 2002.

[9] J. S. L. Ong, J. S. Ng, A. B. Krysa, and J. P. R. David, "Temperature dependence of avalanche multiplication and breakdown voltage in $Al_{0.52}In_{0.48}P$," *Journal of Applied Physics*, vol. 115, no. 6, p. 064507, Feb. 2014.

[10] L. J. J. Tan, D. S. G. Ong., J. S. Ng., C. H. Tan, S. K. Jones, Y. Quan, J. P. R. David, "Temperature Dependence of Avalanche Breakdown in InP and InAlAs," *IEEE Journal of Quantum Electronics*, vol. 46, no. 8, pp. 1153–1157, Aug. 2010.

[11] S. Xie and C. H. Tan, "AlAsSb Avalanche Photodiodes With a Sub-mV/K Temperature Coefficient of Breakdown Voltage," *IEEE Journal of Quantum Electronics*, vol. 47, no. 11, pp. 1391–1395, Nov. 2011.

[12] X. Zhou, C.H. Tan, S. Zhang, M. Moreno, S. Xie, S. Abdullah & J.S. Ng, (2017). Thin $Al_{1-x}Ga_xAs_{0.56}Sb_{0.44}$ diodes with extremely weak temperature dependence of avalanche breakdown. *Royal Society Open Science*, *4*(5), 170071. http://doi.org/10.1098/rsos.170071

[13] A. H. Jones, Y. Yuan, M. Ren, S. J. Maddox, S. R. Bank, and J. C. Campbell, "$Al_xIn_{1-x}As_ySb_{1-y}$ photodiodes with low avalanche breakdown temperature dependence," *Optics Express*, vol. 25, no. 20, p. 24340, Oct. 2017.

[14] M. Grzesik, J. Donnelly, E. Duerr, M. Manfra, M. Diagne, R. Bailey, G. Turner, and W. Goodhue, "Impact ionization in $Al_xGa_{1-x}As_ySb_{1-y}$ avalanche photodiodes", *Applied Physics Letters*, vol. 104, p. 162103, Apr. 2014. 14, 15

[15] Silicon avalanche photodiodes, Hamamatsu, 6045 Si APD Datasheet

[16] M. Ren, Y. Yuan, A. H. Jones, S. J. Maddox, M. E. Woodson, S. R. Bank, J. C. Campbell, "Operation stability study of AlInAsSb avalanche photodiodes," in *2017 IEEE Photonics Conference (IPC)*, 2017, pp. 159–160.

Chapter 6

Dark count rate characterisation of $Al_{0.85}Ga_{0.15}As_{0.56}Sb_{0.4}$ Geiger mode avalanche photodiodes

InP and $In_{0.52}Al_{0.48}As$ Geiger mode APDs are currently being used for both commercial and R&D applications however they suffer from band-to-band tunnelling currents [1, 2]. Tunnelling currents can be mitigated by using a wider bandgap material as avalanche layer. $Al_{0.85}Ga_{0.15}As_{0.56}Sb_{0.44}$ has a wider indirect-bandgap of 1.59 eV compared to 1.34 eV and 1.43 eV for InP and InAlAs respectively. It is lattice matched to InP substrate ensuring its compatibility with telecom wavelength for fibre optic telecommunication applications and its wider bandgap makes it less susceptible to tunnelling currents resulting from high electric fields in Geiger mode. This chapter details investigation of *DCR* as a function of overbias, pulse repetition frequency and reports on the temporal stability of *DCR.* In the following section, fabrication of AlGaAsSb mesa *p-i-n* devices is provided.

Terminology convention in this chapter

Throughout this chapter the term *DCR* refers to *N* i.e. dark counts (C_D) normalised to duty cycle *ft* unless specified otherwise. *f* is pulse repetition frequency and *t* is the pulse duration. *N* and C_D had been defined earlier in Eq. 11 and 12 in chapter 2.

The small size (dia: 25 – 40 μm) devices fabricated and characterised in this chapter are different than mesa devices characterised in the previous chapter (dia: 75 – 420 μm) and the detailed fabrication procedure is given in Sec. 4.2 in Chapter 4.

6.1 Dark count rate measurement as function of overbias

Dark count rate (*DCR*) for a 100 nm thick avalanche layer (wafer number M4339) was carried out using the capacitive quenching scheme discussed in experimental setup shown in chapter 3. A 25 µm mesa *p-i-n* diode with remote bond pads was packaged onto a TO-5 header with 4 pins. Standard *I-V* measurements were carried out to obtain the device breakdown voltages and contact resistance. The result is shown in Fig. 1. The forward *I-V* data for a representative packaged device show an ideality factor of 2.0 and a series resistance value in the range of 1.6-1.8 kΩ using the fitting procedure discussed in chapter 3. A higher series resistance can limit the high frequency operation of a SPAD by imposing a longer recovery time as explained in Fig. 9 chapter 3.

The *DUT* capacitance is measured to be 1.1 pF at 0 V reverse bias and is expected to be even smaller at breakdown voltage due to increase in the depletion layer width. The blocking diode used in our experiments is 15 pF and based on the *DUT* capacitance, blocking diode capacitance, series resistance of the *DUT* and the protection resistance of 1 kΩ, a recovery time of 210 ns is estimated based on 5 times *RC* constant. This places an upper limit of 4.7 MHz on pulse repetition frequency for *DCR* characterisation. The influence of protection resistance can be annulled by removing it from the circuitry to ensure a faster recovery however this will expose the *DUT* to damage from accidental *DC* bias. It is relevant to mention here that the purpose of work carried out in this chapter is to ensure that the overbias pulse shape is clean and stable [8] and we do not carry out high frequency characterisation (GHz range) of *DCR.* For higher frequency biasing schemes such as sine wave gating [5] the pulse shape is not perfectly square and this can lead to non-uniform breakdown probability along the overbias pulse. The ideality factor indicates dominance of recombination currents in the junction. Fig. 1 also compares the forward *I-V* data for the 420 μm mesa device (on-wafer) with the device under study in this chapter.

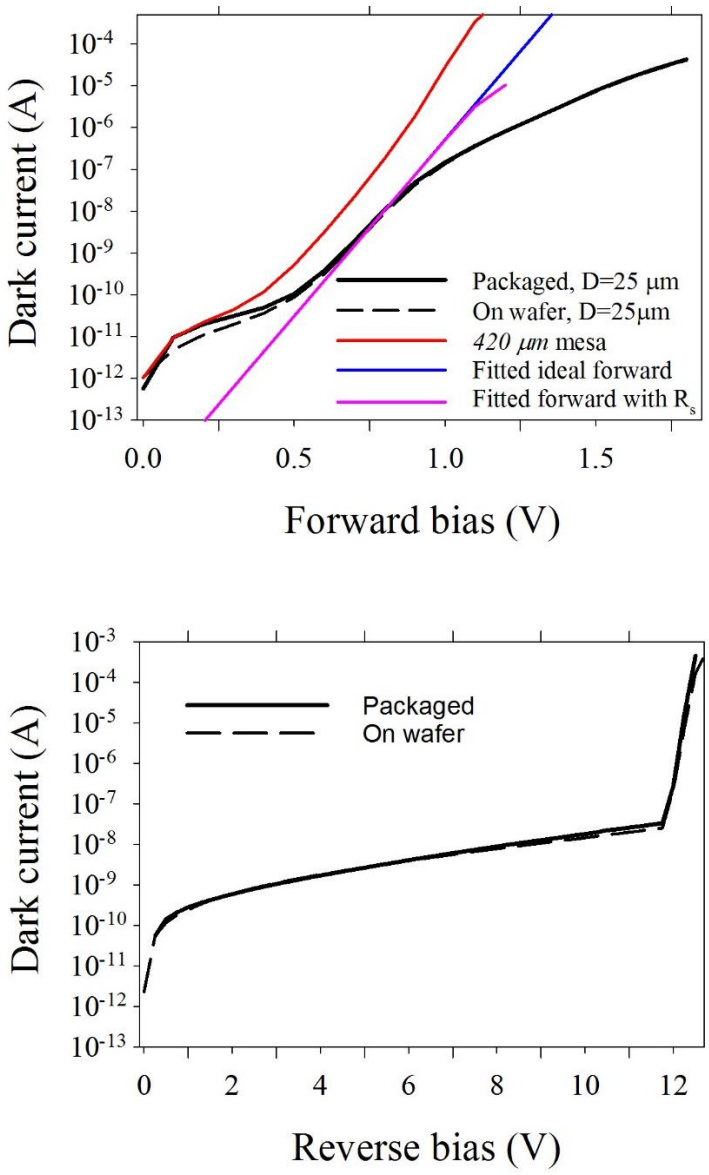

Fig. 1 (Top) Forward I-V data for 25and 420 um diodes. The I-V data for the 25 um packaged diode is fitted with forward current equation (chapter 3). (Bottom) Reverse I-V for 25 um diode before and after packaging.

Owing to the bigger contact size, a smaller contact resistance (80 Ω) is recorded for bigger mesa devices whereas the device under study in this chapter show a contact resistance in the range of 1.6 - 1.8 kΩ. The contact area for the Geiger mode APD bond-pad is 8.8×10^3 μm^2 whereas the contact area of the 420 μm mesa APD is estimated to be 3.4×10^4 μm^2. No rapid thermal annealing was used. A room temperature breakdown voltage of 12.51 V was observed for the packaged device. Analysis of the reverse *I-V* data for the packaged device shows no degradation in dark currents from the wire bonding and packaging process.

The packaged devices under test (*DUT*) were subsequently mounted onto the capacitive quenching circuitry (CQC) board (designed by Dr. Simon Dimler at The University of Sheffield) for *DCR* measurements in gated mode. The *DCR* characterisation was performed using experimental setup in chapter 3, sec. 3.4.1. An *AC* overbias pulse with amplitude of 2.00 V was applied to the cathode of the *DUT*. Typical pulse duration in our experiment is 200 ns. Overbias pulse rise times are fixed at 4.5 ns and a pulse repetition rate of 100 kHz is used. No temperature stabilisation or Peltier cooler was used. The percentage overbias is calculated as $\frac{V_{dc}+V_{ac}}{V_{bd}}$, where the V_{dc}, V_{ac}, and V_{bd} are *DC* bias, *AC* bias and breakdown voltage respectively. The *DCR* characterisation relies on detecting an avalanche signal detected by the sensitive discriminator when the threshold level is set at a certain level. Using the experimental procedure described in sec. 3.4.4, a threshold level of 2.4 mV was set at the discriminator. Fig. 3 shows an avalanche current signal using an *AC* overbias of 2 V and a *DC* bias level of 11.45 V with an *AC* overbias pulse duration of 200 ns. The avalanche pulse is detected as soon as the detection threshold crosses 2.4 mV which corresponds to a latching current of 48 μA across the 50 Ω resistor connected in series with the SPAD.

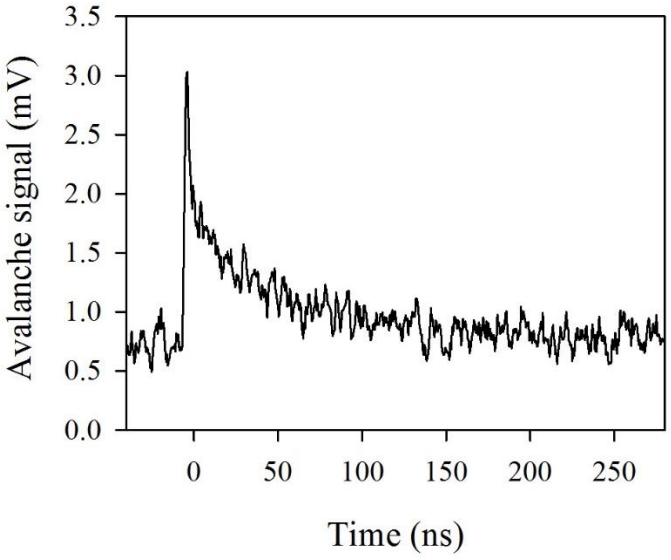

Fig.2 Avalanche current signal from the Geiger mode APD using an overbias pulse amplitude of 2 V and 11.45 V DC at room temperature using an overbias pulse duration of 200 ns.

The data in Fig.2 suggests that avalanche is quenched well within the overbias pulse duration of 200 ns. An added advantage of the capacitive quenching scheme is that the falling edge of the overbias pulse quenches the avalanche [8]. We did not observe any

instantaneous avalanche and subsequent self-quenching due to possible series resistance effect [3]. Moreover, as discussed earlier in Sec. 5.2, we are not operating the GM-APD in a high frequency regime (> 1 GHz) the overbias pulse shape did not show any degradation (for longer overbias pulses of 200 ns and down to 15 ns). We can therefore comment that the overall performance in terms of overbias pulse shape and avalanche quenching are not affected by the magnitude of series resistance reported.

Detection of avalanche signal facilitates *DCR* characterisation where a *NIM* pulse is triggered for detection of an avalanche signal (as the one shown in Fig. 3) in every overbias pulse. Fig. 3 shows the *DCR* as a function of applied overbias above the breakdown.

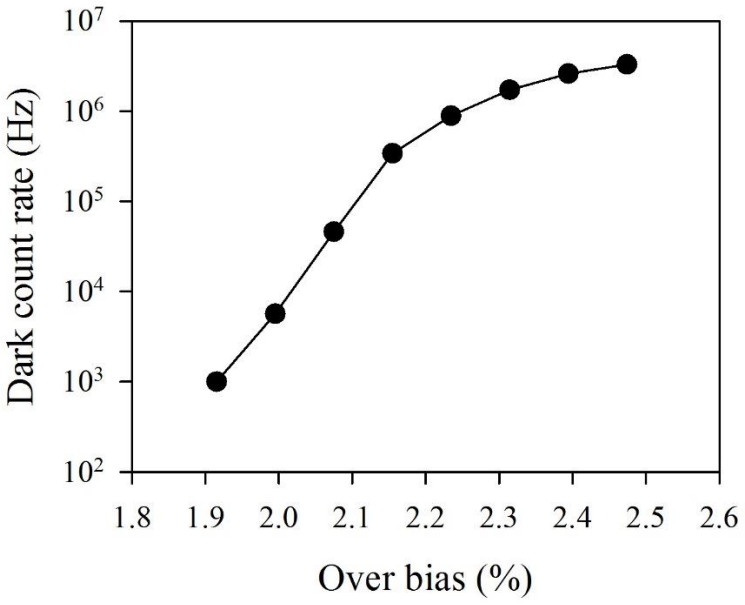

Fig. 3 Dark count rate as a function of overbias for 100 nm thick AlGaAsSb p-i-n diode, D=25 µm, for a gate duration, T_{gate} = 200 ns and an AC pulse amplitude of 2.0 V. breakdown voltage is 12.51 V at room temperature.

The *DCR* measures 1 kHz at 1.93% overbias and reaches 3.31 MHz at 2.5% overbias where the raw dark count value (C_D in Eq. 12 chapter 2) approaches the pulse repetition rate, 100 kHz which sets the maximum limit on the *DCR* of 5 MHz. Recalling Eq. 12 from chapter 2, 100 kHz of repetition rate for a 200 ns overbias pulse duration equates to a *DCR* of 5 MHz provided that a dark count is registered in every overbias pulse. The increase in *DCR* as a function of overbias is due to increase in the avalanche triggering probability by dark carriers [4] as a result of increase in the electric field. In comparison

with InGaAs/InP [5] and InGaAs/InAlAs III-V SPADs [6], maximum overbias values in the range of 10 % – 22% at room temperature can be applied. The device design involves separate absorption and multiplication layers using *i*-InAlGaAs grading and *p*-InAlAs charge sheet. In these devices the electric field develops across the multiplication layer relatively slowly compared to *p-i-n* structure where it is completely confined across the multiplication layer. Fig. 4 compares the calculated electric field profile for $Al_{0.85}Ga_{0.15}As_{0.56}Sb_{0.44}$ Geiger mode APD and the InGaAs/InAlAs Geiger mode APD from ref. [6] for breakdown voltages of V_{bd} and 2.5% above the breakdown. The breakdown voltages InAlAs and AlGaAsSb Geiger mode APD are 69 and 12.51 V at room temperature and 2.5% overbias correspond to 70.7 and 12.8 V respectively. The electric field profile has been simulated using Poisson solver the details of which are listed in Appendix. A. The electric field modelling is used to calculate the electric field in multiplication layer for the *DUT* and the InAlAs Geiger mode APDs in an attempt to provide possible explanation for the sharp rise in *DCR* for our *DUT*.

Parameters used for the calculation of electric field profiles for $Al_{0.85}Ga_{0.15}As_{0.56}Sb_{0.44}$ Geiger mode APD are based on the doping and thickness given in Fig. 1 chapter 4 with an doping level of 1×10^{15} cm^{-3} in the avalanche layer and a breakdown voltage of 12.51 V at 294 K has been used. For the InGaAs/InAlAs Geiger mode APD from ref. [6], doping levels of 5.2×10^{14} cm^{-3}, 1.5×10^{15} cm^{-3} and 3.78×10^{17} cm^{-3} have been used for InGaAs absorber, InAlAs avalanche layer and InAlAs charge sheet respectively. In the same order, thickness of the layers used in the simulation are 1850nm, 980nm and 69 nm respectively. For $Al_{0.85}Ga_{0.15}As_{0.56}Sb_{0.44}$ Geiger mode APD of this work thickness of *p, i* and *n* $Al_{0.85}Ga_{0.15}As_{0.56}Sb_{0.44}$ layers are 300 100 and 100 nm and doping levels of 2×10^{18} cm^{-3}, 1.0×10^{15} cm^{-3} and 2×10^{18} cm^{-3} respectively.

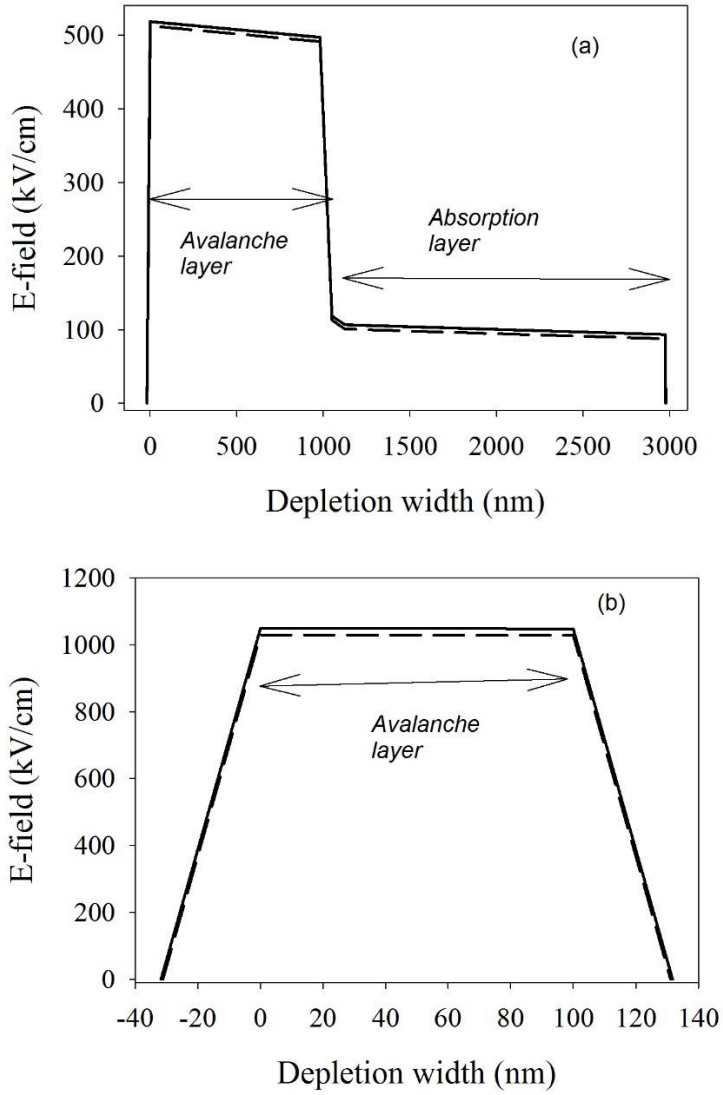

Fig. 4 Calculated electric field profile as a function of depletion width for (a) InGaAs/InAlAs Geiger mode APD from ref. [6]. Breakdown voltage for the device is 69 V (b) AlGaAsSb p-i-n Geiger mode APD of this work. Breakdown voltage is 12.51 V. Both the profiles have been calculated at an overbias of 2.5%. Solid line: Electric field at breakdown, Dashed line: Electric field at 2.5% overbias for each device.

Data in Fig. 4 show that for the $Al_{0.85}Ga_{0.15}As_{0.56}Sb_{0.44}$ Geiger mode APD of this work, the electric field is confined to the multiplication layer and increased from 1030 kV/cm at breakdown voltage to 1050 kV/cm at 2.5% overbias. For the InAlAs GM-APD of ref. [6] the electric field changes from 512 kV/cm at breakdown voltage to 518 kV/cm at 2.5% overbias. Since a higher electric field would impart a greater kinetic energy to Impact Ionising carriers in the multiplication region, a reduced mean free path between the Impact events and a higher Impact Ionisation coefficient is obvious and therefore possibly

a high electric field in the multiplication layer the for *p-i-n* structure can possibly explain why the *DCR* of $Al_{0.85}Ga_{0.15}As_{0.56}Sb_{0.44}$ Geiger mode APD is limited to smaller overbias values in comparison with InGaAs/InAlAs device cited above where overbias values are in the order of 10 – 18%. In $Al_{0.85}Ga_{0.15}As_{0.56}Sb_{0.44}$ Geiger mode APDs in this thesis, there is no InGaAs absorber incorporated in the device structure and therefore a straight forward comparison in terms of the overbias dependent *DCR* with state-of-the-art devices is not be possible. The avalanche detection at low excess bias is possible thanks to excellent transient cancellation owing to small device capacitance (1.2 pF at 0 V reverse bias). The variable capacitor [7] in the *CQC* circuit can easily cancel out possible capacitive transients arising from the device. The capacitive transients due to device are diminished at high reverse bias (close to or above breakdown) as the capacitance decreases owing to increase the depletion width and therefore transient cancellation has not been an issue in our measurements.

For InGaAs/InAlAs SPADs [6] overbias pulse amplitudes of up to 20 V have been applied resulting in strong voltage transients. A direct implication of strong voltage transient is that the threshold level has to be adjusted higher thus inadvertently discarding avalanche signals comparable to or smaller than transients. Study of Meng et al [6] reports no *DCR* below 10% overbias.

6.2 Influence of varying AC and DC level on DCR

For Geiger mode operation SPADs are biased at a *DC* level slightly below breakdown voltage and subsequently an *AC* overbias pulse is imposed on the *DC* level. While the maximum overbias is limited by the device design as discussed in previous section, varying *AC* and *DC* level combination while keeping total overbias constant can help in assessing the severity of capacitive transient signals.

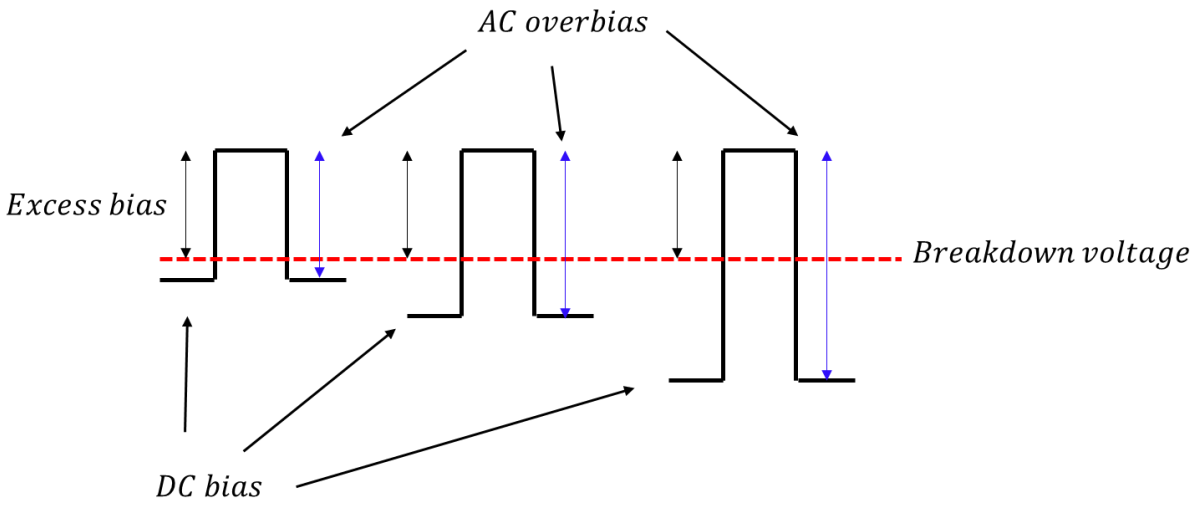

Fig. 5 Schematic illustration of varying AC and DC bias levels while keeping a constant excess bias. Red dashed line represents the breakdown voltage.

As illustrated in Fig. 5, the varying AC and DC bias levels can influence the *DCR* in the following manner:

- High DC bias during the gate-off time can increase the *DCR*
- High AC bias can result in strong voltage transient and avalanche signals smaller than voltage transients are inevitably discarded from counting.

To ascertain the influence of bias levels, we recorded the *DCR* as a function of overbias for AC overbias pulse amplitudes of 2, 4 and 6 V and adjusted the DC bias such that the total overbias remains unaffected. For 2, 4 and 6 V *AC* overbias, 11.44 V, 10.40 V and 9.39 V DC corresponded to 1.83% overbias. Similarly, 11.53 V, 10.49 V and 9.47 V DC corresponded to 2.5% overbias. The result in Fig. 7 shows that avalanche breakdown events are registered for overbias values of 1.83% irrespective of the *AC* overbias pulse amplitude which suggests that transient cancellation is not an issue. The highest DC bias level (2.0 V AC data) does not exacerbate the count rate suggesting the macroscopic avalanche current is properly quenched.

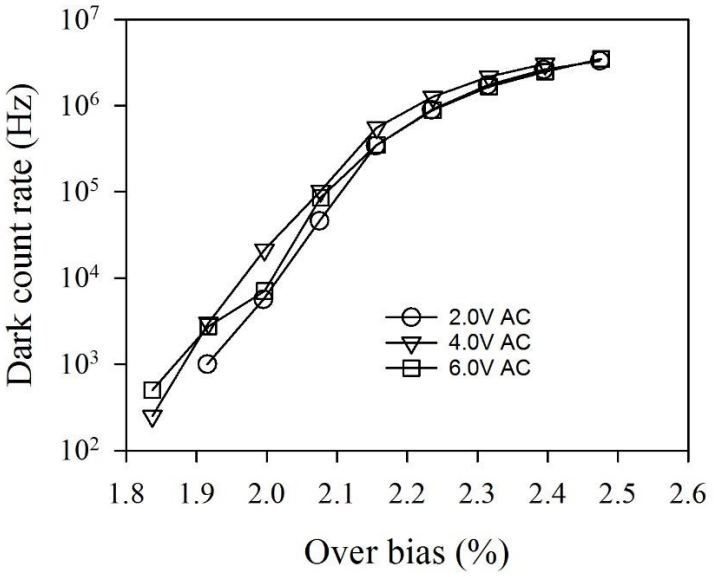

Fig.6 DCR as a function of applied overbias for different AC overbias pulse amplitudes. The total applied overbias is kept constant. Overbias pulse duration is fixed at 200 ns. Lines are shown as guide to the eye.

For the measurements carried out in Fig.6, transient cancellation was not an issue.

6.3 Investigation of dark count rate as a function of repetition frequency

DCR as a function of pulse repetition frequency can be characterised to investigate the presence of afterpulsing effect. Afterpulsing is a secondary source of noise in Geiger mode APDs which increases the *DCR* through material defects in the multiplication region. Such defects act as charge trapping centres and can trap charge carriers during avalanche process. These defect centres have a finite life time following which the carriers can be released. Upon their release, the carriers initiate unwanted avalanche signals thus increasing the *DCR.* In gated mode the total charge and therefore the afterpulsing is limited by applying narrow overbias pulses (typically 15 ns for our devices). Fig. 7 shows the dark count rate as a function of overbias for a 15 ns overbias pulse duration. An *AC* overbias pulse of 2.0 V is used and a pulse repetition rate of 100 kHz is used.

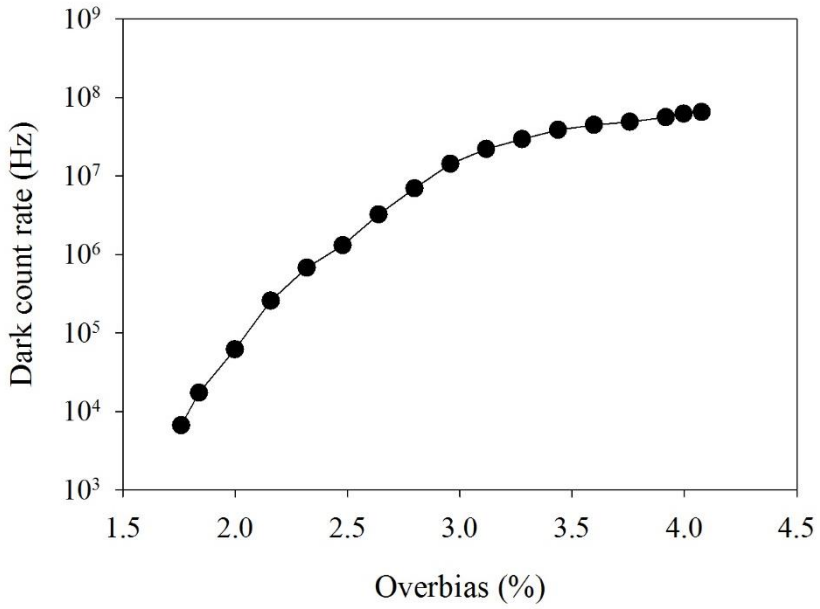

Fig. 7 Room temperature DCR as a function of overbias for a 15 ns pulse duration. AC overbias pulse of 2 V is used. The DC bias values corresponding to the minimum and maximum DCR values are 11.32 V and 11.57 V. Line is shown as a guide to eye.

A larger overbias up to 4.07% was applied and a lower dark count is recorded for 15 ns pulse in comparison with 200 ns pulse duration (Fig. 7). This behaviour can be possibly explained by the imperfect pulse shape for smaller overbias pulses where the rise and fall times become significant in comparison with the overall pulse duration. The mathematical expression for dark counts (C_D) as a function of pulse duration (Eq. 12 chapter 2) predicts a linear dependence of dark counts on pulse duration, assuming a perfect rectangular pulse. However for shorter overbias pulses there can be a deviation from this behaviour. A 15 ns pulse with a rise and fall time of 4.5 ns each, approaches a triangular shape unlike a 200 ns pulse which is relatively close to a rectangular pulse shape. Using a similar capacitive quenching scheme for a Perkin-Elmer Si Geiger mode APD, Dimler et al [8] have observed a deviation of the dark counts from the ideal linear relationship as a function of pulse width for overbias pulse durations less than 50 ns. An imperfect overbias pulse shape was attributed to the reduction of dark counts for shorter overbias pulse by Dimler et al in their study.

Increasing the pulse repetition frequency leads to a reduced pulse separation which can increase the total counts if the pulse separation approaches the trap life time. In the capacitive quenching scheme for *DCR* measurement in this thesis, the maximum pulse

repetition frequency is limited by series resistance and the biasing capacitance in the *CQC* core circuitry as explained earlier in sec. 3.4.2. Using the series resistance of the packaged *DUT* of 1.8 kΩ, a protection resistance of 1 kΩ and biasing capacitance C_B = 15 pF the 5× recharge time constant is 210 ns which corresponds to a pulse repetition frequency of 4.7 MHz.

Fig. 8 shows the *DCR* as a function of pulse repetition frequency at room temperature without using any temperature stabilisation/ Peltier cooler. *DCR* data is shown for 3.39% overbias in Fig.9. The analyses of the *DCR* is facilitated by considering 3 frequency ranges as i.e. 100 kHz – 800 kHz (red line), 800 kHz – 2 MHz (blue line) and 2 MHz – 4.4 MHz. The *DCR* increases by 0.3% from 42.15 MHz to 42.3 MHz when the pulse repetition frequency is increased from 100 kHz to 800 kHz. This shows that *DCR* does not undergo a significant increase. However, when the pulse repetition frequency is increased from 800 kHz to 2.0 MHz, the *DCR* increases 32.15% from 42.3 MHz to 55.9 MHz. Increasing the pulse repetition frequency from 2.0 MHz to 4.4 MHz increases the *DCR* from 55.9 MHz to 63.9 MHz, an increase of 14.3%.

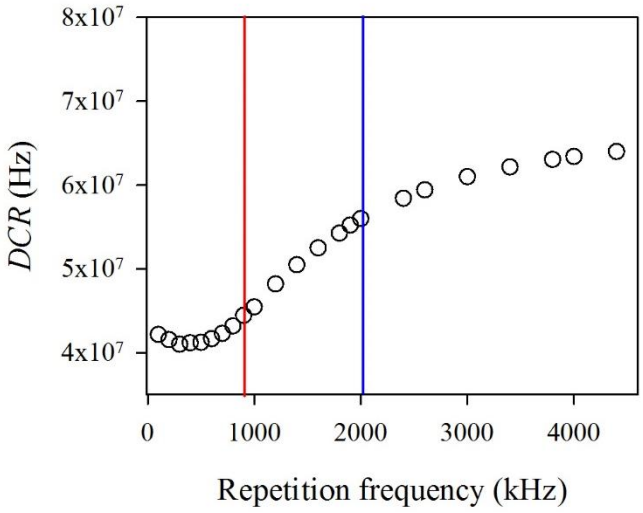

Fig.8 DCR as a function of pulse repetition frequency at an overbias of 3.39%. Overbias pulse duration is 15 ns with an overbias pulse height of 2.00 V. The vertical blue and red lines aid analysis of DCR in 3 frequency ranges (100 – 800 kHz, 800 kHz – 2 MHz, 2 MHz – 4.4 MHz)

The increase in the *DCR* reported here is relatively slow in comparison with InP GM-APDs [9] where an increase the *DCR* increased by 5, 3 and 1 orders of magnitude for 100 K, 150 K and 200 K respectively using an overbias pulse of 100 ns for pulse repetition rates higher than 50 kHz. In this work the afterpulsing becomes more severe due to

increase in the carrier trap release life time at reduced temperature. In comparison with InP the C_{bd} for $Al_{0.85}Ga_{0.15}As_{0.56}Sb_{0.44}$ is smaller by a factor of 3.75 for comparable thicknesses of avalanche layer. Due to the small C_{bd} the breakdown voltage is not expected to change much, heating in the avalanche region at high repetition rates can be a possible reason for the increase of *DCR* in Fig. 9 when the pulse repetition rates are increased beyond 800 kHz at room temperature. In this regard the temperature dependence of the *DCR* study a function of the pulse repetition frequency is needed to confirm the presence of afterpulsing and thermal generation effects.

Presently the temperature dependent study of the *DCR* is not feasible as the physical dimensions of the *CQC* circuitry and the low temperature chamber of the Janis probe-pump station are not compatible. In regards to afterpulsing phenomenon, a straight forward comparison with current Geiger mode APDs cannot be drawn for two reasons:

- The photon detection efficiency is not known for our devices. The standard analyses of afterpulsing is usually carried out at a certain photon detection efficiency. Higher overbias leads to a higher *PDE* but at the same time results in a higher afterpulsing probability which consequently degrades the total *PDE*.
- Standard approach to quantify the afterpulsing effect uses the so-called "double pulse" method where a laser pulse is fired followed by a dark pulse. Consequently, the time between these pulses is varied and a time histogram of the dark events recorded in the second pulse is analysed as a function of the varying time between the pulses. This time is called as dead time. Such a characterisation is not possible at our facilities for the moment and we have no means to measure the breakdown events in the second pulse of the double pulse train only. However we use a similar method with no light and we record the *DCR* as a function of the varying "dead time" for both the first and second pulses.

6.4 DCR as function of double pulse delay/Dead-time

A double pulse output mode from the function generator is used to create double gates with a certain fixed frequency and the double pulse delay can be adjusted. This method is useful since it avoids heating due to higher repetition rates and used the double pulse

delay as a dead time to investigate possible afterpulsing. Schematic illustration of the double pulse method is shown in Fig. 9.

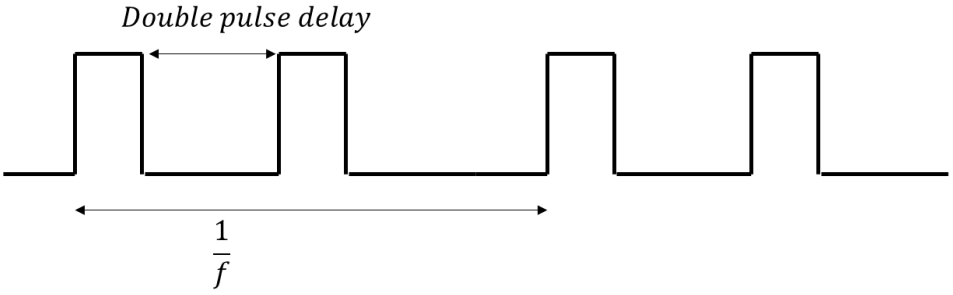

Fig. 9 Schematic illustration of double pulse method. The pulse repetition frequency determines the time lapse between the rising edge of the first pulse. The double pulse delay is adjustable.

The double pulse delay is varied, and the raw dark counts from the Geiger mode APD is recorded. Using the standard way of double pulse characterisation [10], we present the dark counts C_D (defined in chapter 2) as a function of pulse separation or "dead-time" for an overbias pulse duration of 200 ns for 2.25% overbias. The minimum dead time is set at 210 ns due to the device recharge time constant from the biasing capacitance and series resistance, as explained earlier.

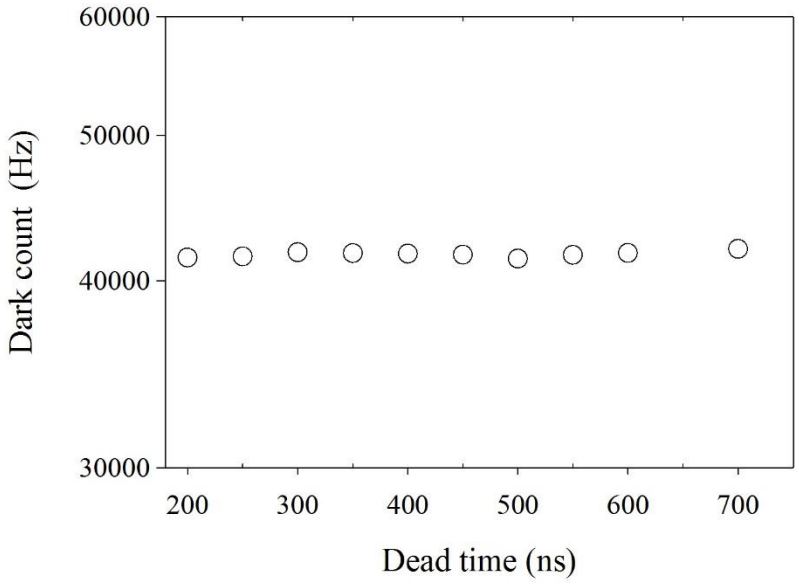

Fig. 10 Dark counts as a function of dead time using the double pulse method for overbias of 2.35% using a 200 ns pulse. AC overbias pulse amplitude is 2 V.

The dark count is recorded at 41.99 kHz at dead time of 700 ns and stays relatively flat with no clear trend of a drift. The dark count is measured at 41.39 kHz at dead time of 10 ns, the minimum possible with the function generator Agilent 81101. The overall fluctuation in the average dark count is ±0.95%. The minimal fluctuation can be the larger pulse duration which is greater than 100 ns, the time duration over which the majority of avalanche events are recorded Therefore decreasing the dead time even down to 10 ns for two consecutive pulses 200 ns each, does not influence the total count. Another observation is that for the device approaches a breakdown in every overbias pulse for the entire range of dead time considered in Fig. 10 and this could also explain why the total counts does not change significantly between the maximum and the minimum dead time. Based on the observation in Fig. 10, we select narrow overbias pulses for the dark count rate characterisation as a function of dead time.

Fig. 11 shows the dark count values as a function of dead time for overbias values of 2.95 and 3.27% using a 2 V *AC* overbias pulse and a pulse duration of 15 ns. Analyses of the data in Fig. 12 shows that dark count values show no significant change at given overbias values when the dead time is decreased from 980 ns to 700 ns. At 3.27% overbias, the dark count changes from 41.8 kHz to 40.76 kHz when the dead time is decreased from 980 ns to 700 ns. A mean dark count of 41.24 kHz (red line in Fig. 11 (a)) is recorded for this range and overbias. Similarly, at 2.95% overbias, the dark count fluctuates between 29.30 kHz and 29.58 kHz when the dead time is decreased from 980 ns to 700 ns. An average dark count of 29.5 kHz (blue line in figure) is recorded for this range and overbias. No clear trend of a drift is observed at any overbias value. In the bottom pane of the figure, the increase in the dark count is shown relative to the average dark count value for the range of dead times between 700 ns and 980 ns as the dark count shows no significant change in this range for all overbias values. The dark count shows an increase of 9.7% and 5.6% when the dead time is decreased from 700 ns to 200 ns for 3.27% and 2.95% overbias respectively. From the data no trend of a dead time as a function of overbias can be observed.

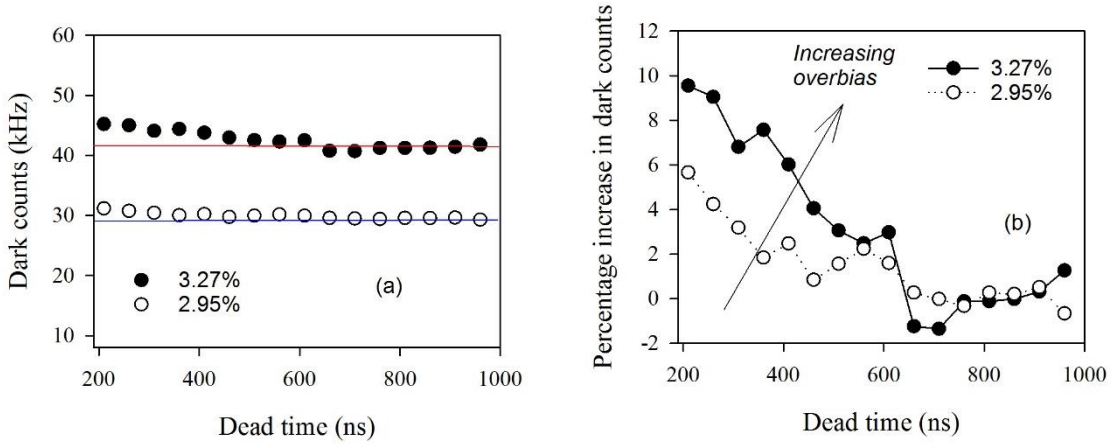

Fig. 11 (a) Dark count (C_D in Eq. 12, chapter 2) as a function of dead time for 3.27 and 2.95% overbias. Solid red and blue lines show the average of the dark count values for the range of dead times between 700 and 980 ns. (Bottom) Percentage increase in the dark count at respective overbias values relative to average dark count values of 41.24 kHz and 29.5 kHz at 3.27 and 2.95% overbias respectively.

The data in Fig. 11 is a possible indication of afterpulsing. An observation from the data is that the dead time should be greater than 700 ns to avoid any possible increase from afterpulsing phenomenon.

6.4.1 Comparison with other works

Korzh et al [11] have studied afterpulsing phenomenon in InGaAs/InP Geiger mode APDs and have reported on the presence of several trap families with trap activation energies in the range of 0.05-0.20 eV. Total afterpulsing probability was found to increase from 0.1% to 2.2% at dead time of 2000 ns when the temperature was decreased from 223 K to 160 K. Such temperature dependent studies of the dark count as function of dead time are used as a standard approach to find the activation energies of the traps. Material defects and impurities in growth were attributed to the afterpulsing phenomenon in this study. Krainak et al proposed the use of sub-bandgap lasers which only depopulate the afterpulsing traps without exciting carriers from valence band to the conduction band, such that traps are emptied without triggering further dark counts [12]. The method involved coupling the trap-emptying light simultaneously onto a commercial InGaAs/InP APD (Adtech model AP1050B InGaAs/InP Geiger mode APD).

Using the trap clearing laser, Krainak reduced afterpulsing by a factor of ×5 for a dead time of 300 ns using a 100 mW/cm^2 laser intensity. Following the work of Krainak, several groups have attempted to reduce the afterpulsig using this technique however no

results in scientific literature have been reported so far to the best of our knowledge. Ren et al [13] have carried out a standard double pulse characterisation of afterpulsing in a Geiger mode $Al_{0.8}Ga_{0.2}As$ APD grown on GaSb substrate based on a 1000 nm thick $Al_{0.8}Ga_{0.2}As$ avalanche layer. An afterpulsing probability of 33% was observed at 170 K for a 1000 ns dead time. The afterpulsing decreased to 24% when the temperature was increased to 290 K. Meng et al [6] have carried out an afterpulsing study of an InGaAs/InAlAs Geiger mode APD at 210 K for pulse repetition rates of 1 – 100 kHz for *PDE* values in the range of 45 – 55% and observed negligible afterpulsing which was attributed to a small duty cycle of the pulse train.

6.5 Temporal stability of DCR without temperature stabilisation

Due to reduced temperature coefficient of avalanche breakdown, thin avalanching layers of $Al_{0.85}Ga_{0.15}As_{0.56}Sb_{0.44}$ offer a higher immunity of breakdown voltage to temperature fluctuations which can be helpful in maintaining a uniform breakdown voltage. It is useful at this point to carry out the analyses of temporal stability of *DCR* for Geiger mode $Al_{0.85}Ga_{0.15}As_{0.56}Sb_{0.44}$ APDs without the use of temperature stabilisation.

Once the measurement conditions are determined, temporal stability of *DCR* is monitored over typical duration of our measurements i.e. about 10 minutes. The device is biased at 3.39% overbias corresponding to a room temperature *DCR* of 30.23 MHz for an overbias pulse duration of 15 ns and a pulse repetition rate of 100 kHz. No temperature stabilisation is used and a threshold level of 2.4 mV is set according to the procedure described in sec. 3.4.4.

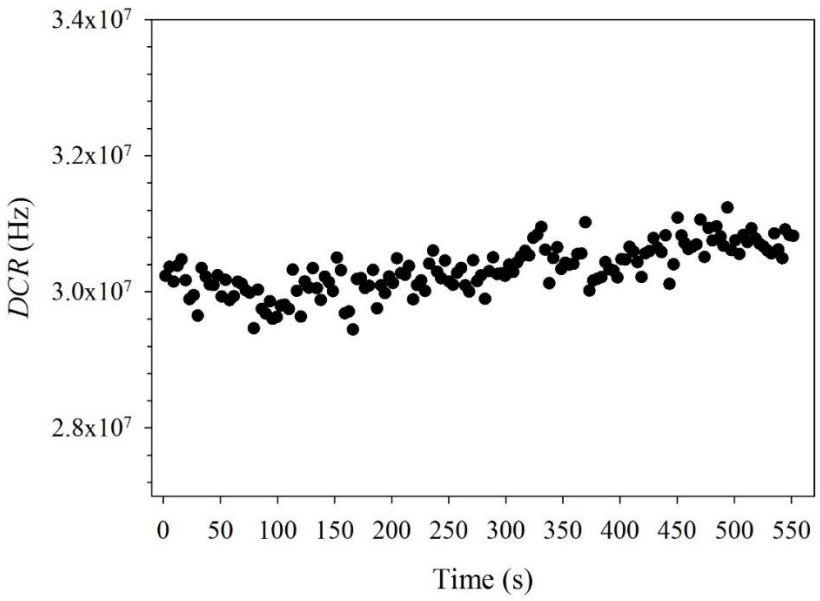

Fig. 12 Room temperature DCR as a function of time for a 100 kHz pulse repetition rate. Overbias of 3.39% is used corresponding to a DCR of 30.23 MHz at t = 0. Overbias pulse duration is 15 ns.

Fig. 12 shows that the *DCR* increases from 30.23 MHz at $t = 0$ to 30.82 MHz at t = 550 s, showing an increase of 1.95%. This increase can be attributed to the variation in the threshold level as shown in Fig. 13 which was recorded simultaneously with the *DCR*. The threshold level decreases from 2.47 mV to 2.29 mV over 550 s which results in the increase in the *DCR* level due to a lower discrimination threshold level for avalanche detection. For the state-of-the-art Geiger mode APDs there exists no such report on the temporal stability of the *DCR* since higher C_{bd} values for these devices would result in a variation of the breakdown voltage if no temperature stabilisation is used. The variation in breakdown voltage in Geiger mode could result in reduction of the *DCR*. To test this hypothesis, the temporal stability of a commercial Si Geiger mode APD (C-30902-SH) is recorded. C-30902SH is a Si reach-through structure APD with a room temperature breakdown voltage of 225 V. It is hermetically sealed behind a flat glass window on a TO-18 header with two pins. The device is mounted onto the *CQC* board for *DCR* characterisation. The next section details the method and results.

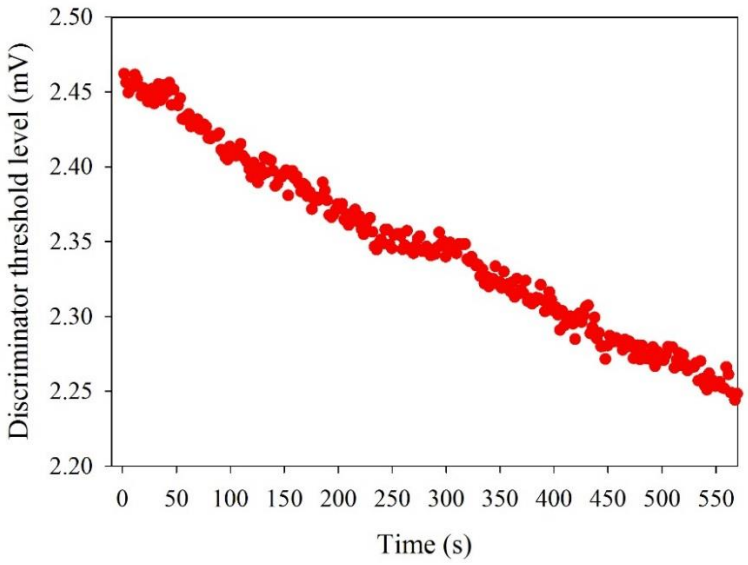

Fig. 13 Discriminator threshold level recorded over the typical measurement duration. The threshold level changes from 2.47 mV to 2.25 mV over 550 s.

6.5.1 Comparison with commercial Si Geiger mode APD

DCR as a function of time was monitored without using any temperature stabilisation for both the $Al_{0.85}Ga_{0.15}As_{0.56}Sb_{0.44}$ Geiger mode APD and a commercial Si SPAD (C30902-SH). A 2V AC overbias pulse is applied to the SPAD and a DC bias of 226 V is used which corresponds to a *DCR* of 27.9 MHz for an overbias pulse duration of 15 ns at a pulse repetition frequency of 100 kHz. The temporal evolution of the *DCR* (data from Fig.13) is then expressed as percentage change relative to *DCR* at $t = 0$, for APD for two different pulse repetition frequencies, 100 kHz. The *DCR* is monitored over time with a value of 30.23 MHz and 28.9 MHz for $Al_{0.85}Ga_{0.15}As_{0.56}Sb_{0.44}$ and the Si Geiger mode respectively at $t = 0$. The data is recorded for two pulse repetition frequencies of 100 kHz and 1 MHz. Fig. 14 shows the result.

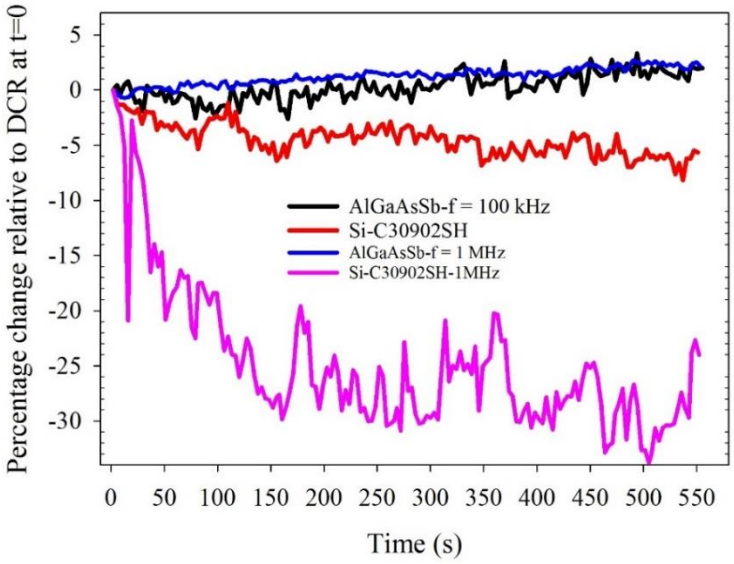

Fig. 14 Percentage change in DCR as function of time for AlGaAsSb Geiger mode APD and Si SPAD for pulse repetition frequency of 100 kHz and 1 MHz.

The commercial Si SPAD shows a percentage decrease in *DCR* of 8% and 30% over 550 s at pulse repetition frequencies of 100 kHz and 1 MHz respectively. The *DCR* of AlGaAsSb Geiger mode APD shows an increase of 1.94% and 2.23% for pulse repetition rates of 100 kHz and 1 MHz respectively over 550 s. As explained in Fig.13, the increase in the *DCR* of $Al_{0.85}Ga_{0.15}As_{0.56}Sb_{0.44}$ Geiger mode APD (Fig. 12 and Fig. 14) can be explained by the variation in the threshold level. The decrease in the *DCR* of Si SPAD becomes pronounced at higher pulse repetition frequency. This decrease can be explained by the increase in the breakdown voltage since the temperature coefficient of avalanche breakdown for Si SPAD is 0.7 V/K compared to 1.60 mV/K for AlGaAsSb Geiger mode APD. This observation points to possible self-heating in Si Geiger mode APD which is pronounced at higher pulse repetition frequency. It is worthwhile to emphasise that the results in Fig. 15 do not put AlGaAsSb at an advantage over Silicon SPADs since the Si SPAD has a thicker avalanche layer and hence a higher temperature coefficient of avalanche breakdown is expected. Nonetheless the results in Fig. 15 show that the $Al_{0.85}Ga_{0.15}As_{0.56}Sb_{0.44}$ avalanche layer is capable to maintain a stable *DCR* without temperature stabilisation mechanisms.

6.6 Temporal distribution of *DCR*

Information on time distribution of the *DCR* can be helpful in optimising the pulse duration and pulse repetition frequencies for Geiger mode operation and understanding the timing characteristics of avalanche breakdown. We are interested in investigating the possibility of any inherent time distribution in the *DCR* of $Al_{0.85}Ga_{0.15}As_{0.56}Sb_{0.44}$ Geiger mode APDs. To accomplish this, we carry out the time distribution measurement of *DCR* using the multi-channel analyser measurement technique detailed in sec. 3.5 in chapter 3. We record the temporal distribution of *DCR* for overbias values of 1.93, 2.07, 2.23 and 2.49% for overbias pulse duration of 200 ns using a pulse repetition rates of 100 kHz, a threshold level of 2.4 mV at room temperature. The time distribution of *DCR* is acquired over 132.3 s, 142.5 s, 159.31 s and 109.15 s respectively in the order of increasing overbias values mentioned. The applied overbias pulse and the temporal distribution of the *DCR* for different overbias values are recorded simultaneously. Fig. 15 shows the result. The breakdown events for all the overbias values are registered close to the rising edge of the overbias pulse. Majority of the breakdown events are recorded within a well-defined duration. In this case, majority of the breakdown events are registered within time duration of less than 100 nsec.

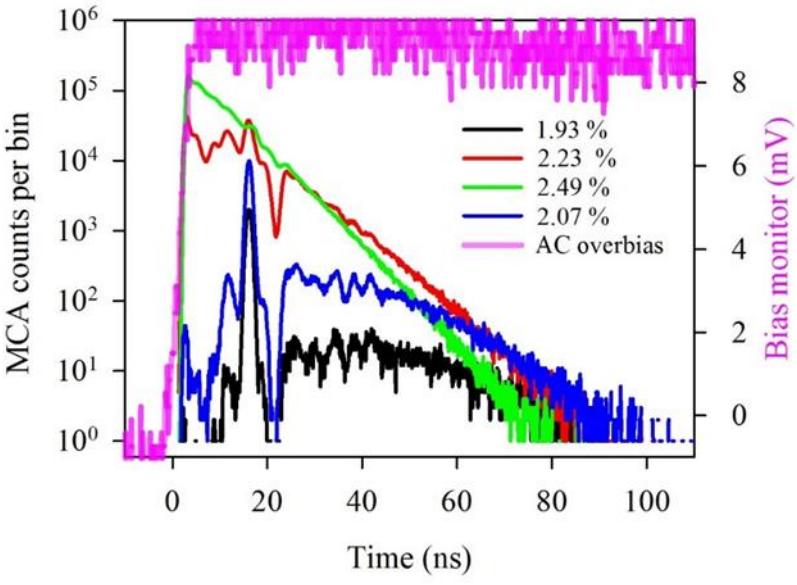

Fig. 15 Time distribution of DCR for Geiger mode AlGaAsSb APD for an overbias pulse duration of 200 ns, pulse repetition frequency of 100 kHz at room temperature. Overbias pulse (pink) is recorded from oscilloscope. Different lines (black, blue, red, green) indicate the time distribution of DCR for different overbias values.

The temporal distribution of the *DCR* shows an exponential decay for higher overbias values while distinct multiple peaks can be observed for smaller overbias values. The origin of multiple peaks in the time distribution of the *DCR* is not known. As a sanity check to rule out any systematic error in recording the time distribution, a MATLAB script was developed by Dr. Simon Dimler from the Impact Ionisation group at The University of Sheffield to acquire avalanche signals directly from the GM-APD. An oscilloscope was used to capture avalanche signals continuously from the GM-APD when the device was biased at 2.1% overbias using an overbias pulse of 200 ns. A MATLAB script was used to process the captured waveforms and the multiple peaks in the time distribution were confirmed indicating that there was no systematic error from the *MCA* system.

At low overbias values the device breakdown at different time instants as soon as the overbias pulse is applied. At higher overbias however the device breakdown demonstrates a more deterministic behaviour where majority of the break down events are registered close to the rising edge of overbias pulse. Afterwards, the time distribution shows a pronounced exponential decay. The decay of time distribution at high overbias can be possibly explained by the probability distribution function of ionisation path length of impact ionising carriers. Studies on time distribution of the *DCR* for commercial Si Geiger mode APD [14, 15, 16] using overbias pulse durations in the range of 10 – 200 ns, an overbias up-to 30% and pulse repetition frequency in the range of 100 kHz – 1 MHz have been conducted. The studies have reported that the time distribution of the *DCR* follows the overbias pulse shape indicating that the devices breakdown along every point of the overbias pulse.

The information on the time distribution of *DCR* can be instrumental in optimising the pulse duration. The pulse duration in Fig.15 can be reduced by 100% doubling the pulse repetition frequency thus supporting maximum count rate applications of the Geiger mode APD while preserving the timing characteristics of *DCR.*

Using the procedure described in sec.5.5 the time distribution of the *DCR* was recorded for very short pulse durations. Short gates limit the amount of charge flow through the active regions and thus reduced the *DCR.* Using an overbias pulse amplitude of 2 V, pulse duration of 15 ns and a pulse repetition rate of 100 kHz. The temporal distribution of *DCR*

was recorded at an overbias of 2.08% corresponding to a room temperature *DCR* of 100 Hz. The result is shown in Fig. 16.

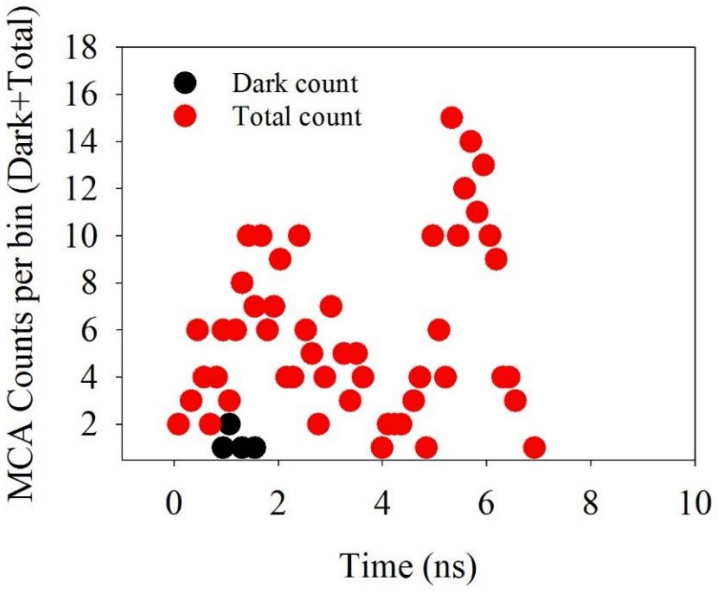

Fig.16. Dark counts (black circles) and total counts (dark +photon) for Geiger mode AlGaAsSb photodiode at room temperature for overbias pulse duration of 15 ns and pulse repetition rate of 100 kHz at an overbias of 2.05%.

According to Fig. 16, as the pulse duration is restricted to 15 ns and a white light is shone over the device, a burst of photon counts is registered. When the device is kept in dark, very few counts are registered. The significance of results in Fig.16 is that $Al_{0.85}Ga_{0.15}As_{0.56}Sb_{0.44}$ GM-APDs hold the potential for room temperature photon detection with lower *DCR*. It is yet to be determined how efficiently the photons are detected i.e. through Single Photon Detection Efficiency (SPDE) measurement. Since the white light source was not calibrated, we cannot calculate single photon detection efficiency of our devices at a particular wavelength at the moment. Nonetheless it is suggested as a future work to calibrate the *PDE* of these devices and assess their dependence on overbias percentage. A calibrated laser source with a known mean photons number per pulse and a temperature controlled operation would be needed to ensure the *DCR* does not increase due to possible thermal generation in the avalanche layer.

6.7 Summary

$Al_{0.85}Ga_{0.15}As_{0.56}Sb_{0.44}$ Geiger mode *p-i-n* APDs were fabricated using standard photolithography and wet chemical etching. Remote bondpads were used for device packaging and subsequent dark count rate characterisation in Geiger mode. The devices showed a significant series resistance. The excess bias dependent *DCR* characterisation showed that the maximum overbias is limited to 2.5% which is due to the *p-i-n* device design which results in electric field confinement in the undoped quaternary layer. Thanks to the small device capacitance the transient cancellation was not a problem and weak avalanche signals were discriminated. *DCR* as a function of pulse repetition frequency and dead time was investigated. The *DCR* increases by 0.3% from 42.15 MHz to 42.3 MHz when the pulse repetition frequency is increased from 100 kHz to 800 kHz. A maximum increase in the *DCR* of 32.15% was recorded when the pulse repetition frequency was increased from 800 kHz to 2.0 MHz.

DCR was recorded as a function of dead time and an increase in the *DCR* was observed when the dead time was less than 700 ns. *DCR* was stable over time duration of 550 s without using any temperature stabilisation. In comparison with commercial Si Geiger mode APD which showed a decrease in *DCR* of -30% over 550 s, the *DCR* of $Al_{0.85}Ga_{0.15}As_{0.56}Sb_{0.44}$ Geiger mode APD showed a maximum increase of +2.23% due to variations in threshold level. The breakdown events of $Al_{0.85}Ga_{0.15}As_{0.56}Sb_{0.44}$ Geiger mode APD shows an exponential distribution in time where majority of breakdown events are registered close to the rising edge of the overbias pulse and happen within a well-defined time duration. $Al_{0.85}Ga_{0.15}As_{0.56}Sb_{0.44}$ Geiger mode APD demonstrated a potential for room temperature photon detection when illuminated with white light.

References

[1] X. Meng, C. H. Tan, S. Dimler, J. P. R. David, and J. S. Ng, “1550 nm InGaAs/InAlAs single photon avalanche diode at room temperature,” *Opt. Express, OE*, vol. 22, no. 19, pp. 22608–22615, Sep. 2014.

[2] A. Tosi, A. Dalla Mora, F. Zappa, S. Cova, M. A. Itzler, and X. Jiang, “InGaAs/InP single-photon avalanche diodes show low dark counts and require moderate cooling,” presented at the SPIE OPTO: Integrated Optoelectronic Devices, San Jose, CA, 2009, p. 72221G.

[3] S. Cova, M. Ghioni, A. Lacaita, C. Samori, and F. Zappa, "Avalanche photodiodes and quenching circuits for single-photon detection," Appl. Opt.35, 1956-1976 (1996).

[4] S. Cova, M. Ghioni, A. Lotito, I. Rech, and F. Zappa, “Evolution and prospects for single-photon avalanche diodes and quenching circuits,” *Journal of Modern Optics*, vol. 51, no. 9–10, pp. 1267–1288, Jun. 2004.

[5] J. Zhang, M. A. Itzler, H. Zbinden, and J.-W. Pan, “Advances in InGaAs/InP single-photon detector systems for quantum communication,” *Light: Science & Applications*, vol. 4, no. 5, p. e286, May 2015.

[6] X. Meng, S. Xie, X. Zhou, N. Calandri, M. Sanzaro, A. Tosi, C.H. Tan, J.S. Ng, (2016). InGaAs/InAlAs single photon avalanche diode for 1550 nm photons. *Royal Society Open Science*, *3*(3), 150584. http://doi.org/10.1098/rsos.150584.

[7] TZC3Z060A110B00 - Trimmer Capacitor, 2 pF to 6 pF, onecall variable capacitor

[8] S. J. Dimler, J. S. Ng, R. C. Tozer, G. J. Rees, and J. P. R. David, “Capacitive Quenching Measurement Circuit for Geiger-Mode Avalanche Photodiodes,” *IEEE Journal of Selected Topics in Quantum Electronics*, vol. 13, no. 4, pp. 919–925, Jul. 2007.

[9] S. Pellegrini, R.E. Warburton, L. J. J. Tan, J.S. Ng, A. B. Krysa, K. Groom, J. P. David, S. Cova, M. Robertson, G. S. Buller, "Design and performance of an InGaAs-InP single-photon avalanche diode detector," in *IEEE Journal of Quantum Electronics*, vol. 42, no. 4, pp. 397-403, April 2006.

[10] A. Restelli, J. C. Bienfang, and A. L. Migdall, “Time-domain measurements of afterpulsing in InGaAs/InP SPAD gated with sub-nanosecond pulses,” *Journal of Modern Optics*, vol. 59, no. 17, pp. 1465–1471, Oct. 2012.

[11] B. Korzh, T. Lunghi, K. Kuzmenko, G. Boso & H. Zbinden, “Afterpulsing studies of low-noise InGaAs/InP single-photon negative-feedback avalanche diodes”. *Journal of Modern Optics* **62,** 1151–1157 (2015).

[12] M. Krainak, “Photoionization of trapped carriers in avalanche photodiodes to reduce afterpulsing during Geiger-mode photon counting”, *(CLEO). Conference on Lasers and Electro-Optics, 2005.* 588-590 Vol. 1 (IEEE, 2005). doi:10.1109/CLEO.2005.201856

[13] M. Ren, X. Zheng, Y. Chen, X. J. Chen, E. B. Johnson, J. F. Christian, J. C. Campbell, "Al0.8Ga0.2As Avalanche Photodiodes for Single-Photon Detection", *Quantum Electronics IEEE Journal of*, vol. 51, no. 11, pp. 1-6, 2015.

[14] DCR as function of time for C30902SH for overbias pulse duration of 200 ns, S. Dimler, Ph.D Thesis, University of Sheffield, 2010.

[15] G. Boso, A. Dalla Mora, A. Della Frera & A. Tosi, “Fast-gating of single-photon avalanche diodes with 200ps transitions and 30ps timing jitter”. *Sensors and Actuators A: Physical* **191,** 61–67 (2013).

[16] A. Gulinatti, P. Maccagnani, I. Rech, M. Ghioni & S. Cova, “35 ps time resolution at room temperature with large area single photon avalanche diodes”. *Electronics Letters* **41,** 272–274 (2005).

Chapter 7

Modelling multiplication gain, excess noise and breakdown characteristics of $Al_{0.85}Ga_{0.15}As_{0.56}Sb_{0.44}$

The objective of this chapter is to model the breakdown characteristics of Geiger mode APDs based on nominally 100 *nm* thick $Al_{0.85}Ga_{0.15}As_{0.56}Sb_{0.44}$ avalanche layer presented in chapter 6. To model the breakdown characteristics, field dependent impact ionisation coefficients are required to simulate the breakdown probability. Due to the lack of experimental reports on the impact ionisation coefficients of $Al_{0.85}Ga_{0.15}As_{0.56}Sb_{0.44}$ we extract the impact ionisation coefficients by modelling the measured gain and excess noise data using a recurrence model. The ionisation coefficients and ionisation threshold energies extracted are used to predict the breakdown probability as a function of overbias in an effort to understand the *DCR* data reported earlier in chapter 5

7.1 Device layers and fabrication

For extraction of ionisation parameters, gain data under pure electron and pure hole injection conditions is required. For this purpose, two mesa diodes i.e. a *p-i-n* and *n-i-p* were used to collect photocurrent data under pure injection. The wafer layers were grown through solid source Molecular Beam Epitaxy (MBE) on semi-insulating InP substrate. Mesa diodes were then processed on the layers using standard UV-photolithography and wet chemical etching process described in Appendix. A. Fig. 1 shows the device layers of the mesa APDs. Details of fabrication and characterisation have been reported by Pinel et al [7].

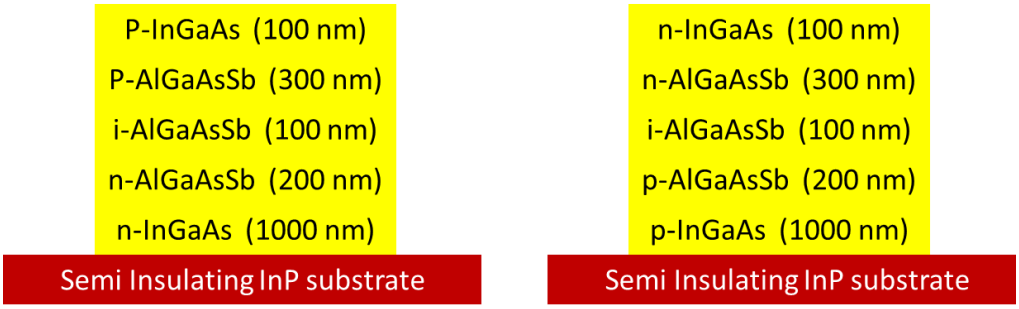

Fig. 1 (Left) Device layers of p-i-n and (Right) n-i-p mesa APD with 100 nm thick avalanche layer grown on semi-insulating InP substrate.

The conditions of pure carrier injection are important to ensure that the avalanche process is initiated by one type of carrier. This is important not only in suppressing the noise in multiplication process arising from the stochastic nature of the process, but it also aids in understanding dynamics of the breakdown probability as a function of overbias, which is the objective of this chapter.

7.2 Modelling impact ionisation coefficients, avalanche gain and excess noise

In most semiconductor materials such as $In_{0.47}Ga_{0.53}As$ [1], $In_{0.52}Al_{0.48}As$ [2], InP [3] and $Al_{0.90}Ga_{0.10}As_{0.02}Sb_{0.98}$ [4] lattice matched to GaSb substrates, the field dependence of impact ionisation coefficients of electrons and holes α and β respectively take the form described by Eq. (1-2).

$$\alpha(E) = A_e \exp\left(-\left(\frac{B_e}{E}\right)^{C_e}\right) \quad (1)$$

$$\beta(E) = A_h \exp\left(-\left(\frac{B_h}{E}\right)^{C_h}\right) \quad (2)$$

where *A*, *B* and *C* are constants. In most semiconductor materials lattice matched to InP substrates

7.2.1 Influence of *A, B C* on α and ß values

Referring to equations 1 and 2, the parameter *A*, *B* and *C* describe the field dependence of impact ionisation coefficients. Parameter *A* indicates the value of ionisation coefficient

at highest electric field value while parameters *B* and *C* define the electric field dependence of the ionisation coefficient as the electric field changes. As an instance, increasing the value of *B* increases the field dependence of the parameter i.e. a faster increase of the parameter when electric field increases. A similar effect can be observed by increasing *C*.

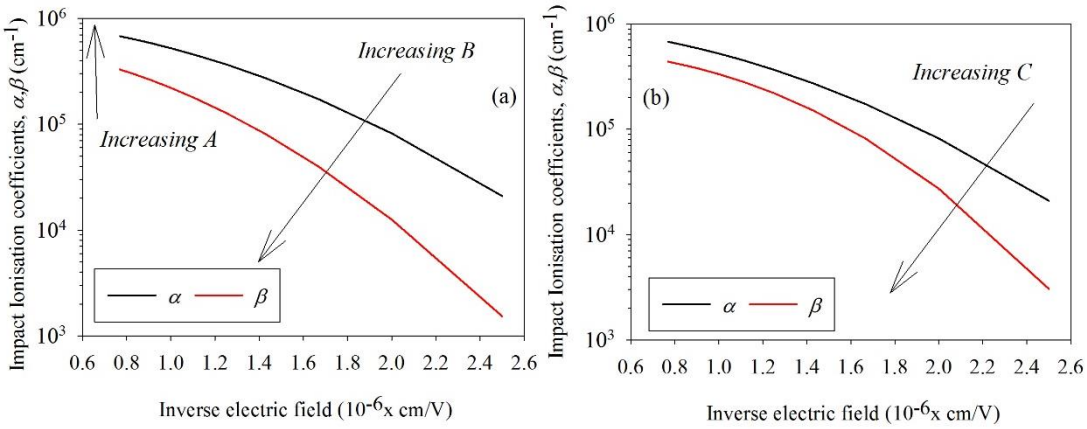

Fig. 2 (a) Simulation of α and *β as a function of inverse electric field for parameter set 1(α: A=1×10^6, B=8×10^5, C=1.95, β: A=6×10^5, B=1×10^6, C=1.95). (b) α* and *β as a function of inverse electric field for parameter set 2 (α: A=1×10^6, B=8×10^5 C=1.95, β: A=6×10^5, B=8×10^5, C=2.40). Legend shows the ionisation coefficients.*

Fig. 2 (a) and (b) compare two sets of α and β as a function of $1/E$ to illustrate the influence of the parameters *A*, *B* and *C*. Parameters for α (cm^{-1}) are the same for both sets ($A=1\times10^6$, $B=8\times10^5$, $C=1.95$). Set1 in Fig. 2 (a) shows the effect of increasing *B* for β ($A=6\times10^5$, $B=1\times10^6$, $C=1.95$) which can be observed as faster increase of the coefficient β when electric field increases. Higher value of *A* for α results in a higher value of the coefficient α for all the electric field values considered in the figure. Set 2 in Fig. 2 (b) shows the effect of increasing *C*. Keeping similar values of *B* for both sets (α: $A=1\times10^6$, $B=8\times10^5$ $C=1.95$, β: $A=6\times10^5$, $B=8\times10^5$, $C=2.40$), a higher value of *C* for β results in a faster increase of the coefficient as the electric field increases. Parameters *B* and *C* therefore collectively define the rate at which the ionisation coefficient increases/decreases when electric field changes.

7.2.2 Recurrence model for calculation of avalanche gain and excess noise

Avalanche multiplication is a random process and excess noise arising from the random position of the impact ionisation of seeded carriers is characterised by the probability

distribution function (*PDF*) of impact ionisation path length. The impact ionisation path length *PDF* simplified under the assumption that the distance *dx* traversed by an impact ionising carrier seeded at *x* is so small such that *x/dx* approaches a very large number, is expressed as

$$P_e(x) = \alpha e^{-\alpha x} \tag{3}$$

This approximation is only valid if the ionisation dead space is very small compared to the mean free path between impact ionising collisions and the length of avalanche region. The ionisation dead spaces for electrons and holes are defined as the minimum distance the carriers must travel before impact ionising and are defined as

$$d_e = \frac{E_{th,e}}{E} \tag{4}$$

$$d_h = \frac{E_{th,h}}{E} \tag{5}$$

Where $E_{th,e}$ and $E_{th,h}$ are the ionisation threshold energy of electrons and holes respectively expressed in *eV*, *E* is the electric field. In case of thin avalanche regions dead space however occupies a significant portion of the avalanche region and must be included in the analyses of multiplication gain and excess noise [5] and the impact ionisation path length PDF for electrons and holes are then approximated by

$$P_e(x) = \begin{cases} 0 & x < d_e \\ \alpha^* \exp\left(-\alpha^*(x - d_e)\right) & x \geq d_e \end{cases} \tag{6}$$

$$P_h(x) = \begin{cases} 0 & x < d_h \\ \beta^* \exp\left(-\beta^*(x - d_h)\right) & x \geq d_h \end{cases} \tag{7}$$

Where α^* β^* are non-local impact ionisation coefficients which incorporate dead space and are expressed as [6]

$$\alpha^* = \left(\frac{1}{\alpha} - d_e\right)^{-1} \tag{8}$$

$$\beta^* = \left(\frac{1}{\beta} - d_h\right)^{-1} \tag{9}$$

The excess noise and avalanche multiplication gain are predicted with ionisation path length *PDF* using a numerical recursive technique which assumes that for a uniform electric field throughout an avalanche region of width, *W*, an electron seeded at point *x*

inside the medium creates additional elector hole pairs after traversing the ionisation dead space. The newly seeded carrier pair behaves in completely independent but statistically identical manner to their parent career and this process continues till all the carriers exit the avalanche region at $x = W$. A similar argument applies to hole which exits the multiplication region at $x = 0$. Due to the extra carrier created as a result of impact ionisation the avalanche gain is expressed in terms of random number of electrons (including the parent carrier) and holes (including the parent carrier) at a given point inside the medium, $Z(x)$, $Y(x)$ as

$$M = \frac{1}{2}(Z(x) + Y(x)) \tag{10}$$

Assuming that an election injected at a position x, undergoes impact ionisation for the first time at point i such that $x < i < w$, two electrons and a hole are created which can undergo further impact ionisation creating a random number of electrons and holes, $Z_1(i)$,$Z_2(i)$ and $Y_1(i)$ respectively. $Z_1(i)$, $Z_2(i)$ and $Y_1(i)$ statistically independent and $Z_1(i)$ and $Z_2(i)$ are distributed in a similar manner in the multiplication region. Provided that the first impact ionisation event happens at i the mean $Z(x)$ is expressed in terms of the impact ionisation probability of electrons $P_e(i\text{-}x)$ as:

$$\langle Z(x)\rangle = \int_x^w \langle Z_1(i) + Z_2(i) + Y_1(i)\rangle P_e(i-x)di \tag{11}$$

In the event of electron leaving the avalanche region without any impact ionisation, the probability for this event to take place is 1- $P_e(w\text{-}i)$ where

$$P_e(x) = \int_{-\infty}^{x} P_e(i)di \tag{12}$$

And similar argument holds for holes seeded at i building up a random number $Y(i)$. Due to the complementary probabilities of carriers initiating or escaping the impact ionisation events, the carrier ensemble average of $Z(x)$ and $Y(x)$ is expressed according to Eq. (13-14) as

$$\langle Z(x)\rangle = 1 - P_e(W-x) + \int_x^w \big(2z(i) + y(i)\big)P_e(i-x)di \tag{13}$$

$$\langle Y(x)\rangle = 1 - P_h(x) + \int_0^x \big(2y(i) + z(i)\big)P_h(x-i)di \tag{14}$$

Where the squared mean average of the ensemble is

$$\langle Z^2(x)\rangle = \int_x^w \langle (Z_1(i) + (Z_2(i) + (Y_1(i))^2\rangle P_e(i-x)di \tag{15}$$

$$\langle Y^2(x)\rangle = \int_0^x \langle (Z_1(i) + (Z_2(i) + (Y_1(i))^2\rangle P_h(x-i)di \quad (16)$$

The excess noise is simply a ratio of the Eq. 15 and 16 and is simplified as

$$F(x) = \frac{\langle M^2(x)\rangle}{\langle M(x)\rangle^2} = \frac{z_2(x)+2z(x)y(x)+y_2(x)}{(z(x)+y(x))^2} \quad (17)$$

Where $z(x) = \langle Z(x)\rangle$, $y(x) = \langle Y(x)\rangle$.

7.2.3 Algorithm for calculation of avalanche gain and excess noise using recurrence equations

The step by step numerical algorithm for calculating the multiplication gain and excess noise using the recursive equations 13, 14, 15 and 16 are solved iteratively according to the following steps:

1. Avalanche region width is discretised using a mesh size, typically 600 points.
2. Ensemble averages *z(x), y(x)* are initialised to values $1-P_e(W-x)$ and $1-P_h(x)$ respectively.
3. The first estimate of *z(x)* was substituted to Eq. (14) to provide an improved estimate for *z(x).*
4. Step 3 is repeatedly processed until a convergence between *z(x) and y(x)* is achieved.

An executable program based on the theoretical model of sec. 6.2.2 and algorithm of sec. 6.2.3 was developed and provided by my supervisor Professor C.H. Tan from the Impact Ionisation group at The University of Sheffield to simulate the avalanche gain and excess noise data.

7.3 Extraction of Impact ionisation coefficients of $Al_{0.85}Ga_{0.15}As_{0.56}Sb_{0.44}$

The avalanche gain data for pure electron and hole injection conditions is obtained experimentally by illuminating the *p-i-n* and *n-i-p* diodes with 442 nm photon

wavelength. The gain and excess noise data was obtained by Lucas Pinel from the Impact Ionisation group at the University of Sheffield. The gain and excess noise data for pure electron, M_e and pure hole M_h obtained from the mesa diodes is subsequently fitted with a recurrence model and algorithm described previously. Avalanche layer thickness, W of 87 nm and 98 nm has been used for simulation of avalanche gain and excess noise of *p-i-n* and *n-i-p* diodes respectively. Ideal *p-i-n* and *n-i-p* diodes were assumed for the simulation. The model incorporates a carrier dead space into the calculations. α^*, $ß^*$, $E_{th,e}$ and $E_{th,h}$ were used as adjustable parameters to fit the experimental data for avalanche gain and excess noise. Table 1 lists the parameter sets derived using the procedure listed in previous section.

Table 1: Parameter sets 1-4 derived with adjusting *A, B, C and threshold ionisation energies*. The parameter values correspond to the field dependence of the impact ionisation coefficient described by Eq. 1 and 2.

Set. No	A_e (cm^{-1})	B_e (cm^{-1})	C_e	A_h (cm^{-1})	B_h (cm^{-1})	C_h	$E_{th,e}$ (eV)	$E_{th,h}$ (eV)
1	1.0×10^6	8.0×10^5	1.66	8.0×10^5	1.65×10^6	2.73	2.80	3.20
2	9.8×10^5	7.9×10^5	1.66	9.9×10^5	1.62×10^6	2.24	3.60	3.70
3	5.3×10^5	6.4×10^5	1.48	4.6×10^5	1.25×10^6	1.62	2.98	3.08
4	1×10^6	8.0×10^5	1.95	9.9×10^5	1.65×10^6	2.50	3.20	3.30

Fig. 3 shows experimental gain for pure electron and hole conditions fitted with the parameter sets shown in Table 1 as set 1 through 4. All parameter sets fit the experimental data reasonably. A robustness check on the parameter sets was done by fitting the excess noise data subsequently using the similar parameter set. Fig. 4 shows the experimental data for excess noise fitted with the parameter sets 1 – 4.

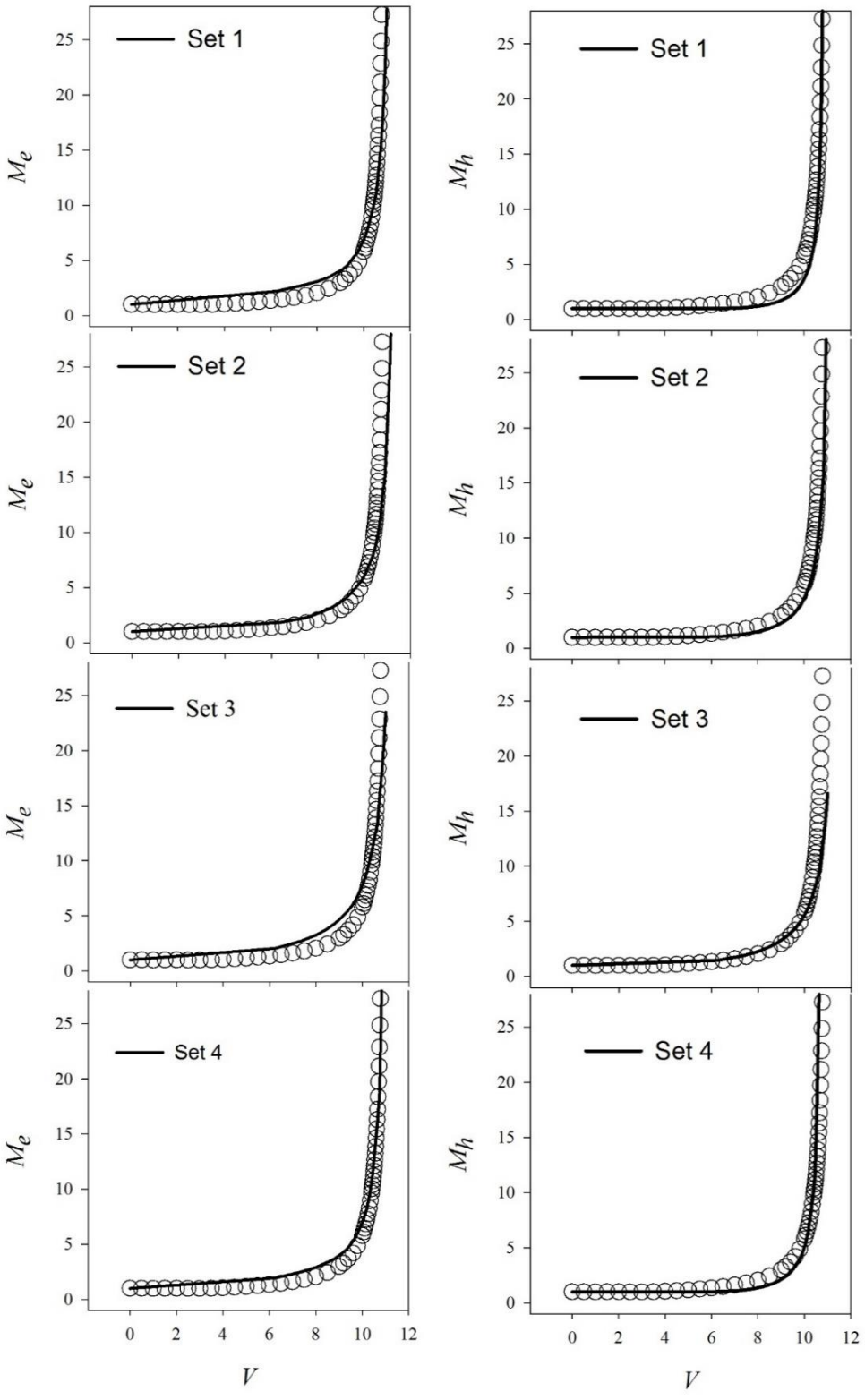

Fig. 3 Avalanche gain versus reverse bias data (circles) for pure electron injection (Left column) and pure hole injection (Right column) fitted with recurrence model using parameter sets 1-4 (solid lines). W=87 nm and 98 nm for p-i-n and n-i-p diodes respectively.

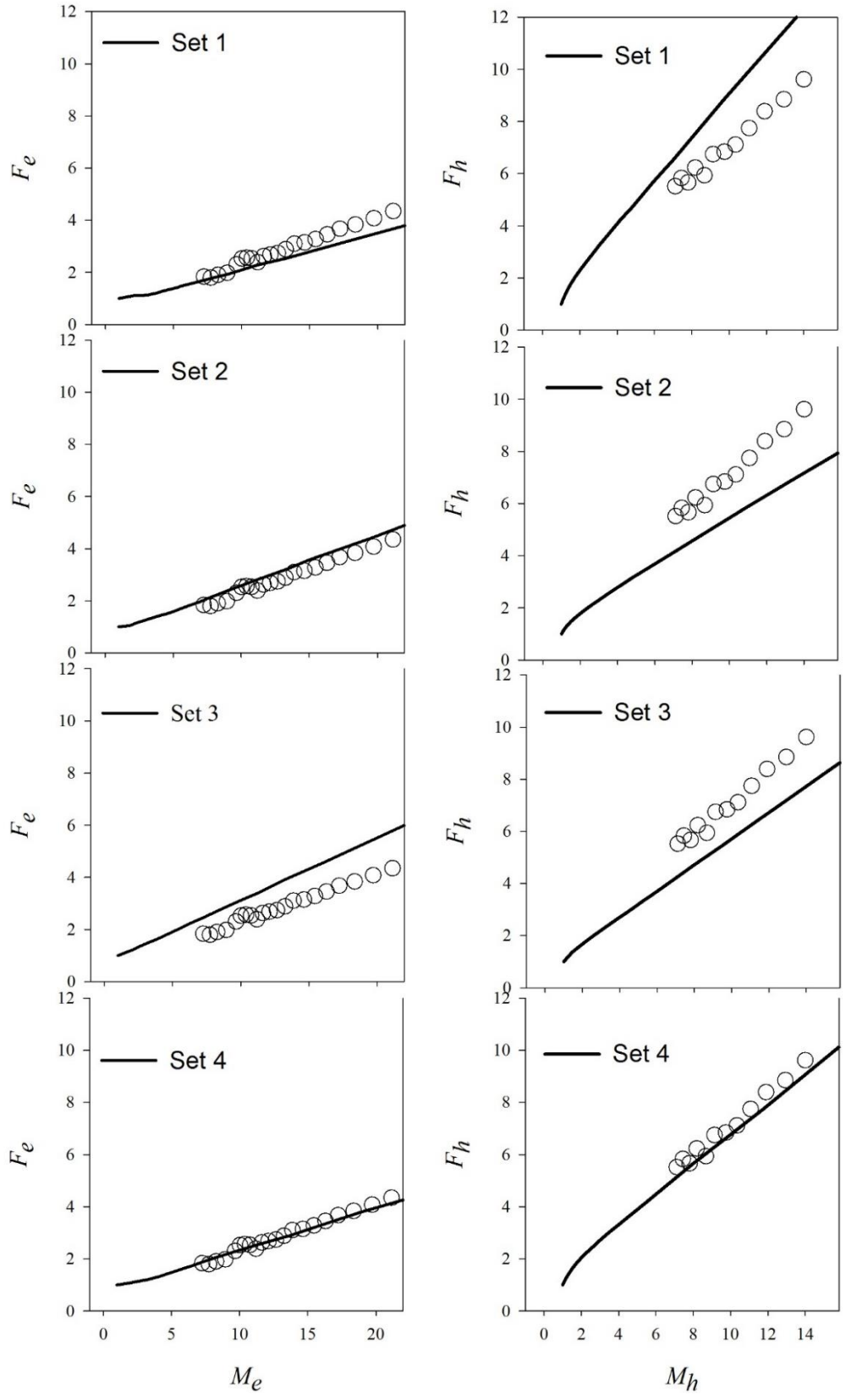

Fig. 4 Excess noise versus reverse bias data (circles) for pure electron injection (Left column) and pure hole injection (Right column) fitted with recurrence model. Parameter sets 1-4 (solid lines) are shown.). W=87 nm and 98 nm for p-i-n and n-i-p diodes respectively.

There are a number of interesting observations in Fig.4. The experimental data for excess noise for pure electron injection is consistently smaller than that of pure hole injection condition for $Al_{0.85}Ga_{0.15}As_{0.56}Sb_{0.44.}$ Recent studies on excess noise characteristics of *p-i-n* and *n-i-p* mesa diodes based on different avalanche thicknesses of $Al_{0.85}Ga_{0.15}As_{0.56}Sb_{0.44}$ by Pinel et al [7] has confirmed that electrons readily impact ionise in comparison with holes. This makes the avalanche process initiated by electrons less noisy compared to a hole initiated avalanche process.

The influence of adjusting the threshold energy can be seen with ease by comparing parameter sets 1 and 4 from Table 1. A higher hole threshold ionisation energy for set 4 leads to a reduced hole excess noise and can be seen by comparing the better fit of F_h versus M_h for set 4 in comparison with set 1 from Fig.4. It should be noted that fitting excess noise and gain data over a much wider range of electric fields would be necessary to test the accuracy of the parameters derived in set 4. However set 4 provides a mean to analyse the ionisation behaviour in $Al_{0.85}Ga_{0.15}As_{0.56}Sb_{0.44.}$ Our fitting suggests that the threshold energies are close to to InP (3.0 *eV* for both electrons and holes) [3] and $In_{0.52}Al_{0.48}As$ [8] (3.20 and 3.50 *eV* for electrons and holes respectively) and similar to $Al_{0.8}Ga_{0.2}As$ [9] (3.20 and 3.30 *eV* for electrons and holes respectively).

Other III-V materials like GaAs [10], $Al_{0.6}Ga_{0.4}As$ [10], $Ga_{0.52}In_{0.48}P$ [11] and $Al_{0.9}Ga_{0.1}As_{0.02}Sb_{0.98}$ [4] have also been investigated and field dependence of local impact ionisation coefficients in these parameters has been reported. Ionisation threshold energies (in eV) of electrons (holes) of 3.0 (3.0), 3.20 (3.50), 3.0 (3.3), 3.4 (3.6), 4.1 (4.1) and 1.74 (3.38) respectively in the order of mentioned references in this paragraph earlier. The local field coefficients, α and *ß* are extracted from Eq. 8 and 9 based on the calculation of non-local impact ionisation coefficients α^* and *ß** from parameter set 4.

To select an electric field range for calculating the impact ionisation coefficients as a function of electric field, we show a semi-log plot of *M-1* as a function of reverse bias for pure electron injection condition i.e. a *p-i-n* diode. Fig. 5 shows the result.

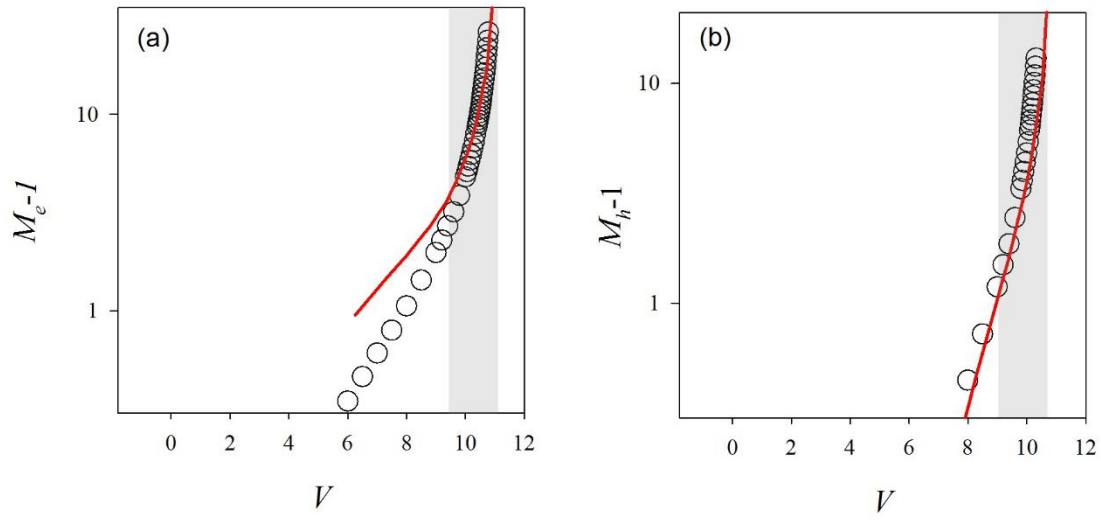

Fig. 5 M-1 versus reverse bias for (a) pure electron injection, p-i-n diode, W = 87 nm. (b) Pure hole injection using the n-i-p diode, W=98 nm Circles: Experimental data, Solid lines: Numerical fit. Rectangular grey shaded region shows the best fit to experimental data.

The modelling in Fig. 5 suggests a better fit to the experimental data in an electric field range of 1080-1263 kV/cm and 1069-1245 kV/cm respectively for electron and hole injection condition (grey shaded regions in Fig. 5). The gain values corresponding to the maximum and minimum electric field are M_e = 6 and 61for pure electron and M_h = 1.8 and 11 for pure hole injection condition respectively. Based on the data in Fig. 5, we select electric field in the range of 1080-1263 kV/cm for calculation of impact ionisation coefficients as a function of electric field.

Fig. 6 shows the local impact ionisation coefficients as function of inverse electric field along with impact ionisation coefficient ratio, *k* defined as $ß/\alpha$. The ionisation coefficients are plotted as a function of inverse electric field in the range of 1080-1260 kV/cm corresponding to gains of 6 and 61 for an ideal *p-i-n* diode. Both the ionisation coefficients and *k* value are shown on a log scale. The impact ionisation coefficients for both electrons and holes increase as electric field increases. The values are relatively disparate in at low field (1080 kV/cm, $\alpha = 2.13\times10^5$ cm^{-1}, $ß = 4.94\times10^4$ cm^{-1}) and tend to merge as the electric field increases (1263 kV/cm, $\alpha = 2.47\times10^5$ cm^{-1}, $ß = 1.35\times10^5$ cm^{-1}). Such a trend has been observed for a host of semiconductor materials including InGaAs [1], InAlAs [8], AlGaAs [10] and AlAsSb [12]. The field dependence of impact ionisation coefficients is influenced by the conduction and valence band structures for impact ionising electrons and holes respectively.

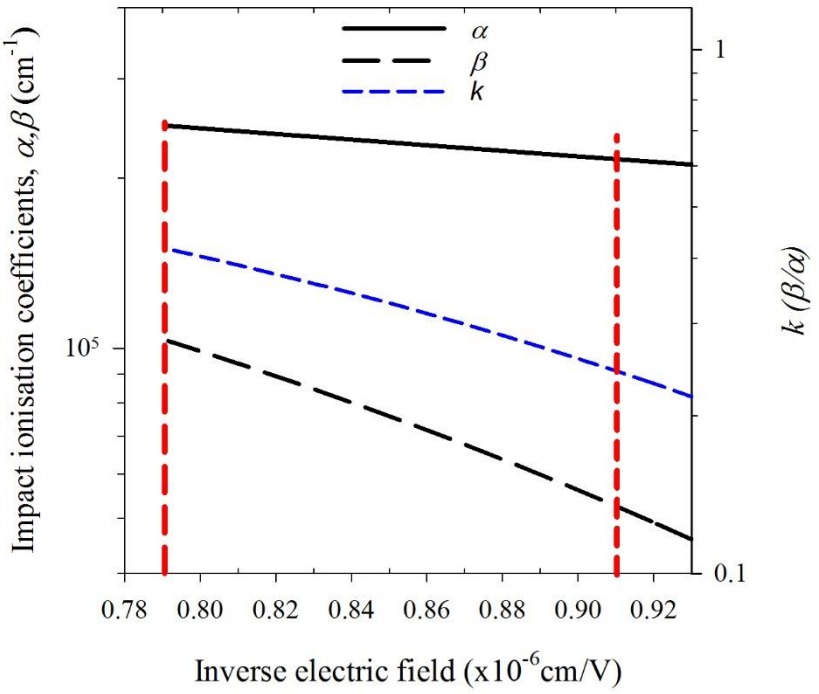

Fig. 6 Impact ionisation coefficients of electrons and holes as a function of inverse electric field for parameter set 4. Impact ionisation coefficients ratio is shown as well. Red dashed lines specify the electric field ranges specified earlier.

The higher electron ionisation coefficient for all electric field values in Fig.6 is indicative of the trend that electrons have a higher impact ionisation probability per unit distance in comparison to holes. This increase in the *k* value is due to the increase rapid increase of the holes ionisation coefficient as the electric field increases. The *k* value increases from 0.23 at 1080 kV/cm (0.91×10^{-6} cm/V) to 0.42 at 1263 kV/cm (0.79×10^{-6} cm/V)

7.3.1 Comparison with other works

The extracted impact ionisation coefficients for $Al_{0.85}Ga_{0.15}As_{0.56}Sb_{0.44}$ have been compared to the work of Yi et al [12] on $AlAs_{0.56}Sb_{0.44}$ for *p-i-n* structure avalanche photodiodes. Comparison in terms of the ionisation coefficients and the *k* value is provided in Fig. 7 and 8 respectively. The calculated local α and ß values for this work are higher than those of the $AlAs_{0.56}Sb_{0.44}$ from Yi et al [12]. The ionisation coefficients from the work of Yi et al are shown for a maximum electric field of 1263 kV/cm.

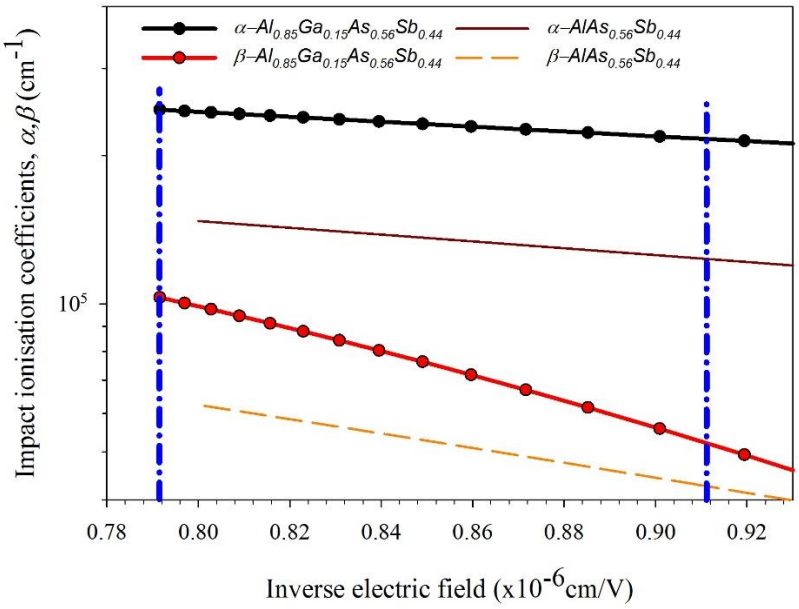

Fig. 7 Comparison of field dependence of impact ionisation coefficients of this work (parameter set 4, solid lines) with $AlAs_{0.56}Sb_{0.44}$ [12]. Dashed blue lines indicate the electric field used for calculation of the impact ionisation coefficients.

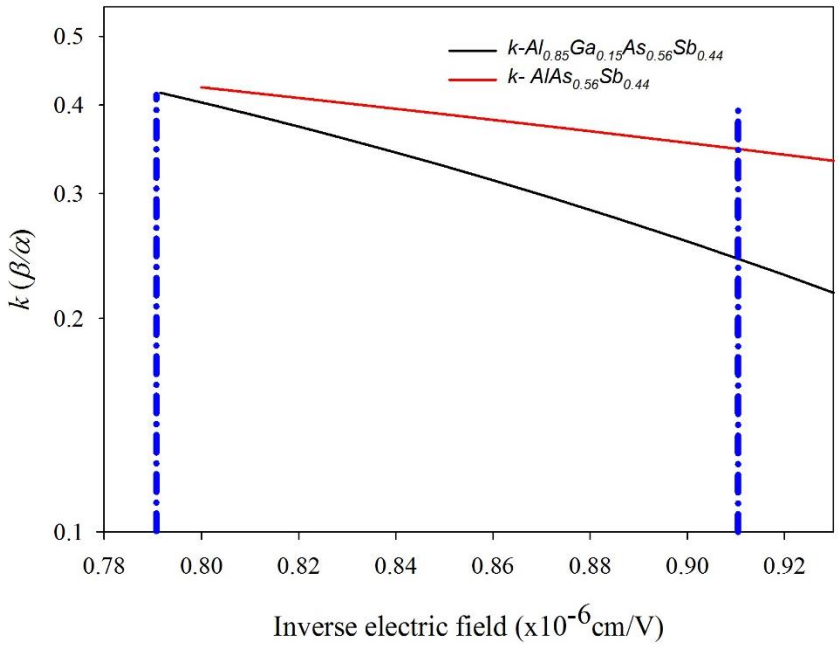

Fig. 8 Comparison of ionisation coefficient ratio, k of this work (parameter set 4) with $AlAs_{0.56}Sb_{0.44}$ [12]. Blue dashed lines show the range of electric field over which the impact ionisation coefficients are calculated.

In Fig. 8, the calculated *k* value of an 87 nm *p-i-n* diode is lower than that of Yi et al. Recalling Eq. 5 from chapter 1, a lower *k* value for a pure electron injection results in a lower avalanche excess noise. This is in agreement with the lower excess noise reported

by Pinel et al [7] for $Al_{0.85}Ga_{0.15}As_{0.56}Sb_{0.44}$ *p-i-n* diode based on 87 nm thick avalanche layer in comparison with a *p-i-n* diode based on 80 nm thick $AlAs_{0.56}Sb_{0.44}$ avalanche layer [13]. The fastest increase in the *k* value for $Al_{0.85}Ga_{0.15}As_{0.56}Sb_{0.44}$ in comparison with $AlAs_{0.56}Sb_{0.44}$ in Fig. 7 can be explained by the rapidly increasing hole ionisation coefficient for $Al_{0.85}Ga_{0.15}As_{0.56}Sb_{0.44}$ as observed in Fig. 6 and 7 as well. The rate of increase of individual ionisation coefficient of electrons and holes influences the increase of *k* ratio. Now we turn our attention to model the breakdown probability and the *DCR* as a function of overbias using the parameter set 4. In the next section we would like to discuss the model limitations.

7.3.2 Limitation of the model

The model assumes a perfect *p-i-n* and *n-i-p* structures where an abrupt doping profile is expected. Real devices however are not perfect *p-i-n* or *n-i-p* structures and depending on the doping the *p* and *n*- $Al_{0.85}Ga_{0.15}As_{0.56}Sb_{0.44}$ layers affect the rate at which the electric field develops across the avalanche layer. Different reverse biases are required to produce a similar change in the electric field across the avalanche layer as in case of a real *p-i-n/n-i-p* structure the electric field develops slowly across the avalanche region in comparison to an ideal *p-i-n/n-i-p* structure. Fig. 9 compares the electric field profile of an ideal and real *p-i-n* diodes. The electric field has been calculated for a real *p-i-n* diode with an 87 nm thick avalanche layer and *p,i* and *n* doping of $2\times10^{18}cm^{-3}$, $1\times10^{15}cm^{-3}$ and -2×10^{18} cm^{-3} respectively using the calculation procedure shown in Appendix. A. The field has been calculated for a reverse bias of 11.99 V for *p-i-n* diode based on an 87 nm thick avalanche layer. A radius of 210 μm has been used for the electric field calculation.

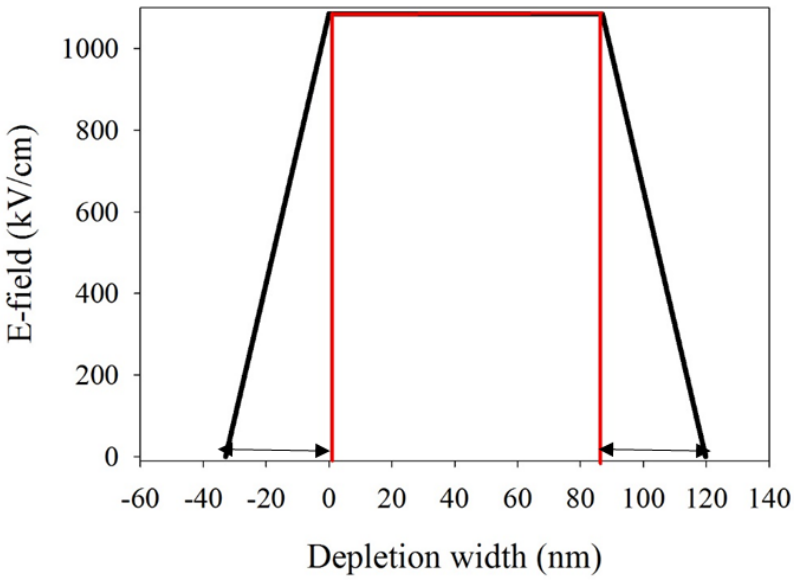

Fig. 9 Calculated electric field as a function of depletion width. Black line: real p-i-n diode, Red: Ideal p-i-n diode.

The arrows in the figure show the depletion in the *p* and *n* layers. It can be observed from Fig. 9 that the depletion in the *p* and *n*- $Al_{0.85}Ga_{0.15}As_{0.56}Sb_{0.44}$ layers changes the rate at which the electric field changes in the avalanche layer. This leads to an effectively higher ionisation coefficients for a real diode structure in comparison with an ideal structure. In order to illustrate this point, a schematic in Fig. 10 shows the electric field profiles for two different reverse bias values. For an ideal *p-i-n* diode in Fig. 10 (a), the entire electric field is confined within the avalanche layer whereas for a real *p-i-n* diode in Fig. 10 (b), there is an effective reverse bias V_{eff} which is lost in extending the depletion region into the adjacent *p* and *n* layers. Consequently a slow increase in the ionisation coefficient is expected for a real *p-i-n* structure leading to an effectively higher ionisation coefficient for each carrier as shown schematically in Fig. 10 (c).

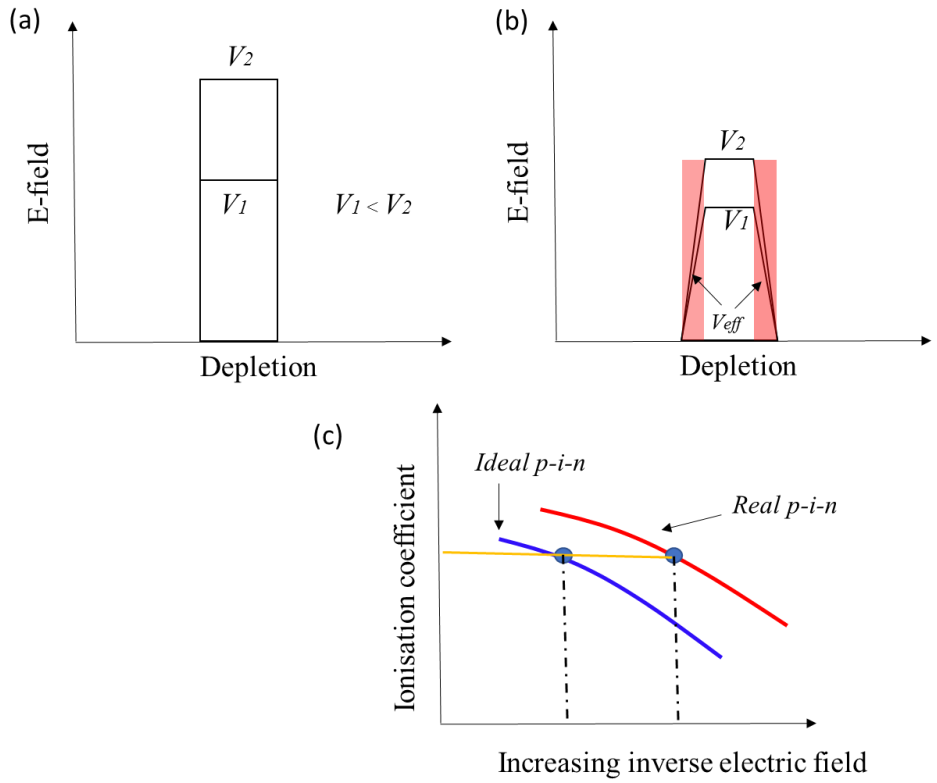

Fig. 10 (a) Electric field profiles at reverse bias values V1, V2 where V2>V1 for (a) ideal p-i-n diode and (b) real p-i-n diode. The red dashed regions in (b) show the depletion into the p and n regions. Veff schematically shows the voltage lost in extending the depletion region into the adjacent layers. (c) Schematic of ionisation coefficient as a function of inverse electric field for an ideal and a real p-i-n diode.

7.4 Modelling breakdown probability as a function of overbias for AlGaAsSb

Impact ionisation coefficients from the parameter set 4 derived previously are used to simulate the breakdown probability as a function of overbias using the numerical modelling technique of Ng et al [14]. The model calculates the breakdown probabilities due to electron-hole pairs for pure injection conditions corresponding to $x=0$ and $x=W$ for a *p-i-n* structure. $x=0$ represents the top edge of avalanche region close to the *p* layer whereas $x=W$ represents the bottom edge of the avalanche region close to the *n* layer in Fig. 1 (a). The breakdown probabilities as a function of position inside the avalanche layer are calculated as a function of the impact ionisation coefficients using the following expressions,

$$\frac{dP_{be}}{dx} = (1 - P_{be}) \times \alpha \, (P_{be} + P_{bh} - P_{be}P_{bh}) \quad (18)$$

$$\frac{dP_{bh}}{dx} = -(1 - P_{bh}) \times \beta \, (P_{be} + P_{bh} - P_{be}P_{bh}) \quad (19)$$

Where the breakdown probability for an electron-hole pair is calculated using the expression,

$$P_{bp}(x) = P_{bh}(x) + P_{be}(x) - P_{bh}(x)P_{be}(x) \quad (20)$$

The executable programme for simulating the breakdown probability was provided by my co-supervisor, Professor Jo Shien Ng. For calculation of the breakdown probability, an avalanche layer thickness of *W=110* nm is used based on fitting the capacitance data of $Al_{0.85}Ga_{0.15}As_{0.56}Sb_{0.44}$ mesa diode, *D = 220 μm* using the experimental method described in sec. 3.2 in chapter 3 and simulation procedure described in Appendix. A. The breakdown voltage is calculated from the simulation and corresponds to the reverse bias where the breakdown probability becomes non-zero. The calculated breakdown voltage for $Al_{0.85}Ga_{0.15}As_{0.56}Sb_{0.44}$ mesa diode based on 110 nm thick avalanche layer is 11.99 V. The breakdown probability is simulated as a function of overbias for pure electrons and hole injection conditions corresponding to positions *x = 0* and *W* respectively. Fig. 11 shows the calculated pair breakdown probability as a function of overbias for pure carrier injection conditions using the impact ionisation coefficients from parameter set 4.

The pair breakdown probability as a function of overbias for pure electron injection is higher than that of holes. This is explained by the fact that electrons readily impact ionise in $Al_{0.85}Ga_{0.15}As_{0.56}Sb_{0.44}$ compared to holes and therefore a higher breakdown probability is expected for carrier injection conditions maximising the injection of electrons.

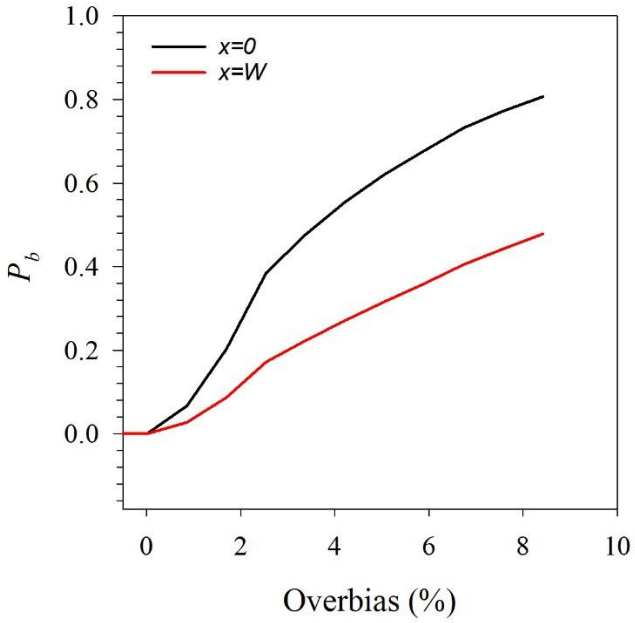

Fig. 11 Breakdown probability as function of overbias for pure electrons (x=0) and pure hole injection conditions (x = W) for an ideal p-i-n diode. W=110 nm for the simulation and the calculated breakdown voltage from the simulation is 11.99 V.

Comparing the calculated breakdown probability for pure electron injection conditions with experimental *DCR* data can be useful in assessing the suitability of the parameter set 4 in modelling the breakdown probability. To facilitate the comparison, the experimental data for *DCR* from chapter 5 is normalised to the maximum achievable *DCR* for the experimental conditions. The *DCR* data for a 15 ns pulse (Fig. 8 chapter 5) is normalised to the maximum *DCR* of 66 MHz and a comparison is made with the calculated breakdown probability as shown in Fig. 12.

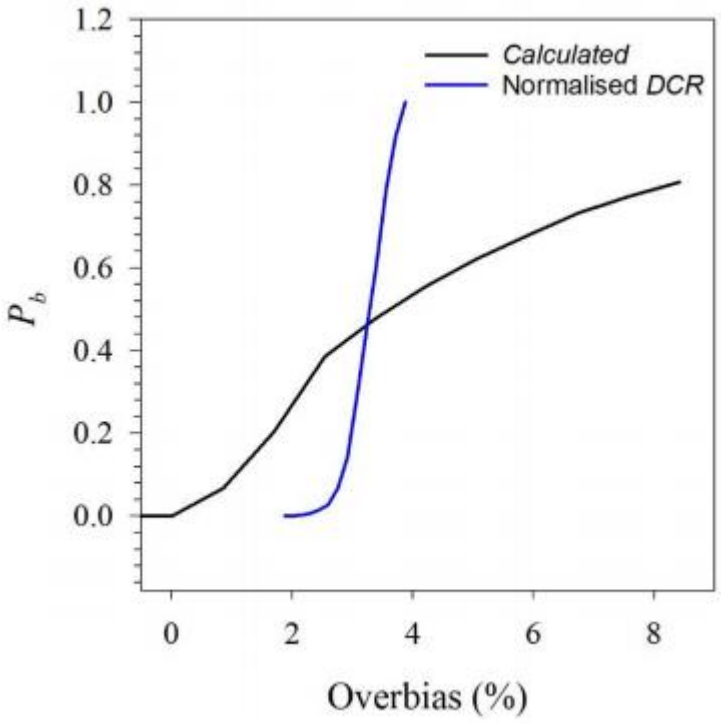

Fig. 12 Comparison of calculated breakdown probability with normalised DCR. The normalised DCR is calculated from the experimental conditions of Fig. 7 chapter 6. Normalised DCR is for 15 ns overbias pulse,

The normalised *DCR* increases very fast in comparison with the predicted breakdown probability. The calculated breakdown probability for pure electron injection reaches 0.8 at an overbias of 8.4% whereas the normalised *DCR* reaches saturation at 2.5% overbias. Unless a dark carrier generation rate inside the avalanche layer is known, breakdown probability is not sufficient to model the *DCR*. Modelling *DCR* as function of overbias [15 - 17] is possible only if both the breakdown probability due to pure carrier injection and dark carrier generation rates inside the avalanche layer are known. At the moment we do not know the dark carrier generation rate inside the avalanche layer mostly due to experimental constraints. Provided that the dark carrier generation rate is known, conservative impact ionisation coefficients may not be sufficient to model the breakdown probability. In the next section, I would like to address these points in an effort to provide possible explanation of why the predicted breakdown probability is not sufficient to model the *DCR* as a function of overbias.

7.4.1 Dark carrier generation rate

Dark carrier generation rate which strongly depends on overbias and increases as the overbias is raised. Several researchers for example Huntington et al [15, 17] have used the following model to estimate *DCR* as function of overbias using the position dependent breakdown probability P_{be}(x) and a position dependent dark carrier generation rate *G(x)* and is expressed as

$$DCR(x) = A_{GM-APD} \times \int G(x) \times (P_{be}(x) + (P_{bh}(x))\, dx \tag{22}$$

The dark carrier generation rate *G(x)* in Eq (22) can be a contribution from various sources of dark carriers generated inside avalanche layer including thermal generation and recombination, afterpulsing, trap assisted tunnelling and band to band tunnelling effects. Eq. (23) elaborates further the position dependent *DCR* in terms of the various sources just mentioned.

$$DCR(x) = A_{GM-APD} \times \int [G_{G-R}(x) + G_{afterpulse}(x) + G_{trap}(x) + G_{band-to-band}(x)] \times (P_{be}(x) + (P_{bh}(x))\, dx \tag{23}$$

- **Generation recombination rate**

In expressing Eq. (23) instantaneous effects of afterpulsing have been ignored. The carrier generation and recombination rates in the avalanche layers are tied to the Shockley-Read-Hall (*SRH*) life time. In typical InP Gieger mode operation for example, the generation recombination rates are negligible in wide bandgap avalanche layer and are only considered for narrow bandgap InGaAs absorber [17]. In such consideration, the thermal generation from absorber layer is negligible as they are cooled. In our Geiger mode APD we do not have any absorber layer, nonetheless the thermal generation component cannot be ignored as our GM-APD is not cooled and the experiments carried out in this chapter are at room temperature with no temperature stabilisation. At the moment we do not know the *SRH* life time for the nominally 100 nm thick AlGaAsSb avalanche layer.

- **Afterpulsing induced dark carrier generation rate**

As discussed in previous chapter, afterpulsing is due to the trap defects in the avalanche layer that can trap charge carries which can be released later on during the avalanche flow causing spurious and unwanted avalanches. Assuming a position dependent excess trap concentration of *N(x)* with a characteristic trap life time T_{trap}, the dark carrier generation rate due to afterpulsing traps at time *t* after breakdown can be expressed in Eq. (24) as

$$G_{afterpulse}(x) = \frac{N(x)}{T_{trap}} \exp(-\frac{t}{T_{trap}}) \quad (24)$$

DCR versus pulse repetition frequency data shown earlier in Fig. 12, Chapter 6 indicated a possible afterpulsing effect in the avalanche region. However to confirm on this hypothesis, data on temperature dependent *DCR* will be imperative to extract the afterpulsing trap life time [16]. Since the dimensions of our *DCR* measurement equipment is not compatible with the physical dimensions of a Janis probe pump station we were not able to perform low temperature *DCR* measurements and therefore we do not know the afterpulsing trap life time. In addition, the position dependent afterpulsing trap concentration inside the avalanche layer is not known.

- **Dark carrier generation due to trap assisted and band to band tunnelling currents**

Dark carrier generation through trap assisted tunnelling is a 2-step process. Firstly an electron is promoted out of the valence band into the mid-gap defect site resulting in a mobile hole in valence band and an occupied trap. In the second step, if the trapped electrons manages to tunnel to the conduction band from the trap site, an electron hole pair is created in the avalanche layer. Provided that the excess pair have enough energy, dark carriers can be generated during the avalanche flow. This generation rate depends on position dependent density of trap states, $N_t(x)$ trap energy level E_t, Fermi energy of the semiconductor material and the tunnelling trap life time, T_{tunn} and is expressed in Eq. (25) as

$$G_{trap}(x) = \frac{N_t(x)}{T_{tunn}}(1 + \exp[\frac{E_t - E_F}{k_B T}])^{-1} \quad (25)$$

Where k_B is Boltzmann's constant. Experimental study of *DCR* at different temperatures by Tosi et al [17] on a Princeton Lightwave, PLI InP Geiger mode APD has shown that trap assisted tunnelling is dominant contributor to *DCR* due to deep traps in the InP multiplication layer. Such an analysis is not possible at our facilities due to the lack of low temperature characterisation of *DCR*.

Band to band tunnelling currents are negligible due to wide bandgap of $Al_{0.85}Ga_{0.15}As_{0.56}Sb_{0.44}$ (1.59 eV at 294 K) avalanche layers as confirmed by Zhou et al [18] on their study on breakdown characteristics of $Al_xGa_{1-x}As_{0.56}Sb_{0.44}$.

In summary, parameters on *SRH* life time, tunnelling trap life times, position dependent tunnelling trap concentration, afterpulsing trap life time and position dependent afterpulsing trap concentration will be needed for estimation of dark carrier generation rate inside the $Al_{0.85}Ga_{0.15}As_{0.56}Sb_{0.44}$ avalanche layer and presently we cannot model the experimental data for *DCR* as a function of overbias. Now we turn our attention to the conservative Impact Ionisation coefficients extracted earlier in this chapter and comment on the need for a more comprehensive experimental data for avalanche gain and excess noise needed for modelling the Impact Ionisation coefficients.

7.4.2 Conservative Impact Ionisation coefficients

The calculation of the breakdown probability in this chapter is based on the Impact Ionisation coefficients extracted from fitting the gain and excess noise data for an 87 nm and 98 nm thick avalanche layers. At the moment, we have calculated the ionisation coefficients in the electric field ranges of 1080-1263 kV/cm. Based on the calculated breakdown voltage of 11.99 V for a 110 nm thick avalanche layer, an electric field calculation has been carried out at different overbias values (Breakdown probability in Fig. 12) in the range of 0.01 – 8.4% and the result is shown in Fig. 13 where the electric field profile is plotted as a function of depletion region.

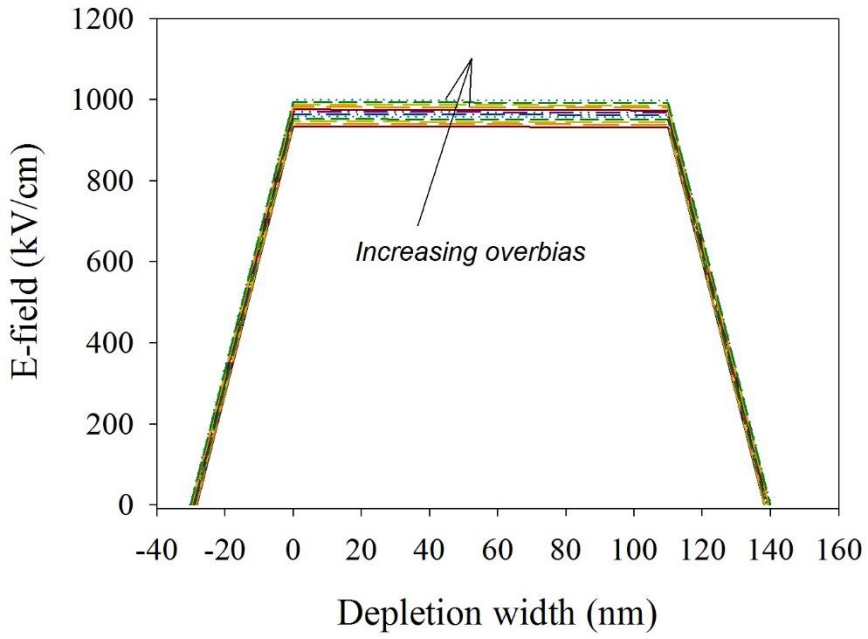

Fig. 13 Electric field as a function of depletion width for a 110 nm thick avalanche layer. The Data sets correspond to overbias values in the range of 0.01% to maximum of 8.4 % overbias using a breakdown voltage of 11.99 V.

As observed in Fig. 13, the maximum electric field for 8.4% overbias is 999 kV/cm which is outside the range of electric field covered in calculation of the impact ionisation coefficients for $Al_{0.85}Ga_{0.15}As_{0.56}Sb_{0.44}$. This can possibly be a reason (s) for the disagreement between the normalised *DCR* and breakdown probability in Fig. 12.

A range of avalanche layer thicknesses is needed to test the accuracy of the ionisation coefficients which may model the normalised *DCR* more accurately provided that lack of impact ionisation coefficient values in low electric field range is the only reason for disagreement between normalised *DCR* and breakdown probability. In this regard, it is worthwhile to note that the authors of ref. [12] have extracted the local Impact Ionisation coefficients for $AlAs_{0.56}Sb_{0.44}$ experimentally by fitting excess noise data for seven (7) different avalanche layer thicknesses in the range of 100 *nm* to 1.5 μm covering an electric field range of 220 – 1250 kV/cm for α and 360 – 1250 kV/cm for β. Whereas the coefficients extracted in this work are based on an avalanche layer thickness of 87 *nm* and 98 *nm* only covering an electric field range of 1080 – 1263 kV/cm and 1069 – 1245 kV/cm for α and β respectively. Moreover, as described in sec. 6.3.2 the model is valid only for an ideal *p-i-n* structure and the actual impact ionisation coefficients corresponding to a real *p-i-n* structure are expected to be slightly different.

In summary, given the lack of parameters involved in estimation of dark carrier generation rates and the conservative Impact Ionisation coefficients used in this work to predict the breakdown characteristics, it is not possible to model the *DCR* as a function of overbias at the moment. Further experimental work on the following is needed:

- Characterisation of *DCR* as a function of overbias at different temperatures.
- Avalanche gain and excess noise data for several thicknesses of $Al_{0.85}Ga_{0.15}As_{0.56}Sb_{0.44}$ avalanche layer.

7.5 Summary

In summary, we have modelled the breakdown characteristics of Geiger mode APDs based on 110 nm thick avalanche layers of $Al_{0.85}Ga_{0.15}As_{0.56}Sb_{0.44}$ lattice matched to InP substrate. The impact ionisation coefficients were extracted by fitting the experimental data for avalanche gain and excess noise under pure carrier injection conditions for *p-i-n* and *n-i-p* diodes based on 87 nm and 98 nm thick avalanche layers respectively. A comparison of the field dependence of local ionisation coefficients was made with $AlAs_{0.56}Sb_{0.44}$ lattice matched to InP substrate. Based on the extracted impact ionisation coefficients, the breakdown probability was modelled as a function of overbias for pure injection conditions.

References

[1] J. S. Ng, C. H. Tan, J. P. R. David, G. Hill, and G. J. Rees, "Field dependence of impact ionization coefficients in $In_{0.53}Ga_{0.47}As$," *IEEE Transactions on Electron Devices*, vol. 50, no. 4, pp. 901–905, Apr. 2003.

[2] Y. L. Goh, D. J. Massey, A. R. J. Marshall, J. S. Ng, C. H. Tan, W. K. Ng, G. J. Rees, M. Hopkinson, J. P. R. David, S. K. Jones, "Avalanche Multiplication in InAlAs," *IEEE Transactions on Electron Devices*, vol. 54, no. 1, pp. 11–16, Jan. 2007.

[3] L. W. Cook, G. E. Bulman, and G. E. Stillman, "Electron and hole impact ionization coefficients in InP determined by photomultiplication measurements," *Applied Physics Letters*, vol. 40, no. 7, pp. 589–591, Apr. 1982.

[4] X. Collins, A. P. Craig, T. Roblin, and A. R. J. Marshall, "Impact ionisation in $Al_{0.9}Ga_{0.1}As_{0.08}Sb_{0.92}$ for Sb-based avalanche photodiodes," *Appl. Phys. Lett.*, vol. 112, no. 2, p. 021103, Jan. 2018.

[5] S. A. Plimmer, J. P. David, D.C. Herbert, T.-W. Lee, G. J. Rees, P.A. Houston, R. Grey, P.N. Robson, A. W. Higgs, D.R. Wright, "Investigation of impact ionization in thin GaAs diodes," *IEEE Transactions on Electron Devices*, vol. 43, no. 7, pp. 1066–1072, Jul. 1996.

[6] A. Spinelli and A. L. Lacaita, "Mean gain of avalanche photodiodes in a dead space model," *IEEE Transactions on Electron Devices*, vol. 43, no. 1, pp. 23–30, Jan. 1996.

[7] L. L.G. Pinel, S. J. Dimler, X. Zhou, S. Abdullah, S. Zhang, C.H. Tan, and J. S. Ng, "Effects of carrier injection profile on low noise thin Al_{085} Ga_{015} As_{056} Sb_{044} avalanche photodiodes," *Optics Express*, vol. 26, no. 3, p. 3568, Feb. 2018.

[8] Y. L. Goh, D. J. Massey, A.R. Marshall, J.S. Ng, C.H. Tan, W. K. Ng, H. J. Rees, M. Hopkinson, J. P. David, S. K. Jones, "Avalanche Multiplication in InAlAs," *IEEE Transactions on Electron Devices*, vol. 54, no. 1, pp. 11–16, Jan. 2007.

[9] B. K. Ng, J. P. David, S. A. Plimmer, G. J. Rees, R. C. Tozer, M. Hopkinson, G. Hill, "Avalanche multiplication characteristics of $Al_{0.8}Ga_{0.2}As$ diodes," *IEEE Transactions on Electron Devices*, vol. 48, no. 10, pp. 2198–2204, Oct. 2001.

[10] S. A. Plimmer, J. P. R. David, G. J. Rees, and P. N. Robson, "Ionization coefficients in $Al_xGa_{1-x}As$ (x = 0 - 0.60)," *Semicond. Sci. Technol.*, vol. 15, no. 7, p. 692, 2000.

[11] R. Ghin, J. P. David, S. A. Plimmer, M. Hopkinson, G. J. Rees, D.C. Herbert, D.R. Wright, "Avalanche Multiplication and Breakdown in Ga In P Diodes," *IEEE TRANSACTIONS ON ELECTRON DEVICES*, vol. 45, no. 10, p. 6, 1998.

[12] X. Yi, B. Liang, L.W. Lim, X. Zhou, M. C. Debnath, D. L. Huffaker, C.H. Tan and J. P. David, "Demonstration of large ionization coefficient ratio in AlAs 0.56 Sb 0.44 lattice matched to InP," *Scientific Reports*, vol. 8, no. 1, p. 9107, Jun. 2018.

[13] J. Xie, S. Xie, R. C. Tozer, and C. H. Tan, "Excess Noise Characteristics of Thin AlAsSb APDs," *IEEE Transactions on Electron Devices*, vol. 59, no. 5, pp. 1475–1479, May 2012.

[14] J. S. Ng, C. H. Tan, and J. P. R. David, "A comparison of avalanche breakdown probabilities in semiconductor materials," *Journal of Modern Optics*, vol. 51, no. 9–10, pp. 1315–1321, Jun. 2004.

[15] Y. Kang, H. X. Lu, Y.-H. Lo, D. S. Bethune, and W. P. Risk, "Dark count probability and quantum efficiency of avalanche photodiodes for single-photon detection," Applied Physics Letters, vol. 83, no. 14, pp. 2955-2957

[16] B. Korzh, T. Lunghi, K. Kuzmenko, G. Boso, and H. Zbinden, "Afterpulsing studies of low noise InGaAs/InP single-photon negative feedback avalanche diodes," *arXiv:1411.0653 [physics]*, Nov. 2014.

[17] A. Tosi, A. D. Mora and F. Zappa, "Performance evaluation of InGaAs/InP SPAD for high clock rate QKD", Private communication, 2019 (Researchgate).

[18] X. Zhou, S. Zhang, J. P. R. David, J. S. Ng, and C. H. Tan, "Avalanche Breakdown Characteristics of Al1-xGaxAs0.56Sb0.44 Quaternary Alloys," *IEEE Photonics Technology Letters*, vol. 28, no. 22, pp. 2495–2498, Nov. 2016.

Chapter 8

Conclusion and Future Work

8.1 Conclusion

We have fabricated and characterised linear and Geiger mode avalanche photodiodes based on thin avalanche layers of $Al_{0.85}Ga_{0.15}As_{0.56}Sb_{0.44}$. Device fabrication for linear and Geiger mode APDs was carried out. Uniform breakdown voltages were observed across the wafer. A series resistance problem was observed with devices of smaller sizes possibly due to poor metal adhesion and smaller contact area.

For the linear mode characterisation, temperature and temporal dependence of avalanche gain was assessed. The results showed that mesa diodes based on thin AlGaAsSb avalanche layers showed a reduced temperature sensitivity of avalanche breakdown (1.6 mV/K) which is attributed to the combination of reduced phonon scattering at high electric fields for thin avalanche layers and dominant alloy scattering. The temporal stability of avalanche gain shows promising results with a maximum fluctuation in mean percentage gain of ±1.33% at 353 K. No premature edge breakdown was observed in the devices. An analyses of the dark current after gain measurements at elevated temperature confirmed there was no significant thermal degradation. Thin avalanche layers of $Al_{0.85}Ga_{0.15}As_{0.56}Sb_{0.44}$ have the potential to replace state-of-the-art InP and InAlAs avalanche layers and can simplify the operational complexity of APD packages which rely on temperature stabilisation circuitry to maintain constant gain.

The promising temperature and temporal stability of avalanche gain is also beneficial for Geiger mode operation. $Al_{0.85}Ga_{0.15}As_{0.56}Sb_{0.44}$ mesa diodes were operated in Geiger mode and the maximum overbias was limited to 2.5 – 4 %. The electric field is confined entirely across the undoped layer in the *p-i-n* mesa diodes and this is a possible reason for

saturation of *DCR* at low overbias values. This is in stark contrast to InP or InAlAs Geiger mode APDs where the electric field is not entirely confined in the multiplication layer. The voltage transient signals were not a problem in *DCR* characterisation and the overbias pulse amplitudes and *DC* levels did not affect the *DCR* values which is a practical advantage over InP or InAlAs Geiger mode APDs. In addition, owing to the small device capacitance, weak avalanche signals were easily discriminated. Study on the *DCR* characterisation showed that the avalanche current was properly quenched. Studies on *DCR* as a function of dead time suggested that shorter overbias pulses should be used to see any influence from possible afterpulsing effects. *DCR* characterisation as function of pulse repetition frequency and dead time for narrow overbias pulse (15 ns) showed an increase in the dark count as dead time was reduced below 700 ns. A temperature dependent study of *DCR* is needed to confirm the afterpulsing effect. The *DCR* for $Al_{0.85}Ga_{0.15}As_{0.56}Sb_{0.44}$ Geiger mode APDs demonstrated a promising temporal stability without relying on conventional Peltier coolers and showed a maximum increase of 2.23% which was attributed to variations in threshold level. Time distribution of *DCR* showed an exponential decay where majority of avalanche breakdown events were registered close to the rising edge of the overbias pulse. The breakdown events were recorded within a well-defined pulse duration of 100 ns.

Impact ionisation coefficients for thin $Al_{0.85}Ga_{0.15}As_{0.56}Sb_{0.44}$ avalanche layers were derived by fitting experimental data for avalanche gain and excess noise under pure injection conditions with recurrence technique. Reasonable fits to the avalanche gain and excess noise data were obtained. Subsequent modelling of breakdown probability as function of overbias was carried out using the impact ionisation coefficients derived previously. Modelling suggested that the recorded *DCR* increased at a significantly faster rate than predicted breakdown probability characteristics. This suggests either significant onset of tunnelling current, inaccuracies in ionisation parameters or influence of threshold level used in measurements.

8.2 Future work

Based on the *DCR* results obtained in this thesis, we recommend the following as our suggested future work.

8.2.1 Temperature dependent *DCR* characterisation

Temperature dependent study of *DCR* can shed light on two important aspects of the Geiger mode APDs under study in this thesis. Studies on the *DCR* as a function of pulse repetition frequency in chapter 5 have suggested that their might be thermal generation in the avalanche region at higher repetition frequencies which resulted in an increase of the *DCR* as the repetition frequency was increased from 800 kHz to 4.4 MHz. Since the temperature coefficient of avalanche breakdown is very small for $Al_{0.85}Ga_{0.15}As_{0.56}Sb_{0.44}$ we believe thermal generation can possibly increase the *DCR*. If this study is carried out at a lower temperature, this hypothesis can be confirmed. Therefore as a future work based on this study, we suggest carrying out *DCR* characterisation at lower temperatures.

Temperature dependent study of *DCR* as a function of overbias can be very useful to ascertain the origin of the dark counts registered in the Geiger mode. According to Arrhenius equation the temperature dependence of *DCR* can be expressed according to

$$DCR = A\exp(-\frac{E_A}{Tk_b}) \quad (1)$$

Where E_A, T and k_B are process activation energy, temperature and Boltzmann's constant respectively and A is a constant. Carrying out the *DCR* characterisation as a function of overbias at different temperatures can help in estimating the activation energy of the mechanism which can help in assessing if the *DCR* is from thermally generated carriers or tunnelling effects.

8.2.2 Single Photon Detection Efficiency of *p-i-n* Geiger mode $Al_{0.85}Ga_{0.15}As_{0.56}Sb_{0.44}$ avalanche photodiodes

In Geiger mode, $Al_{0.85}Ga_{0.15}As_{0.56}Sb_{0.44}$ avalanche photodiodes have demonstrated a potential for photon detection for short overbias pulse duration of 15 ns. The device was biased at 1.95% overbias for a pulse repetition rate of 100 kHz. The result shows a potential of AlGaAsSb for photon detection for shorter overbias pulse durations which are useful for high count rate applications. Since the light source was not calibrated, a single photon detection efficiency cannot be estimated. Using a controlled light source with a certain frequency and wavelength, the number of photons per pulse at the test

wavelength can be estimated and single photon detection efficiency can consequently be calculated. In the next section we discuss the future prospects of turning the Geiger mode, $Al_{0.85}Ga_{0.15}As_{0.56}Sb_{0.44}$ *p-i-n* avalanche photodiodes into Single Photon Avalanche Diodes (SPADs).

8.2.3 $In_{0.47}Ga_{0.53}As$/ $Al_{0.85}Ga_{0.15}As_{0.56}Sb_{0.44}$ Single Photon Detectors

$Al_{0.85}Ga_{0.15}As_{0.56}Sb_{0.44}$ is lattice matched to InP and using a separate absorption multiplication structure (SAMAPD), $In_{0.47}Ga_{0.53}As$ layer can be incorporated with $Al_{0.85}Ga_{0.15}As_{0.56}Sb_{0.44}$ to provide detection at 1550 nm. For conceiving an $In_{0.47}Ga_{0.53}As$/ $Al_{0.85}Ga_{0.15}As_{0.56}Sb_{0.44}$ SAMAPD type Geiger mode photodiode (also referred to as a SPAD), the following needs to be considered.

Higher depletion thickness due to charge sheet, grading and absorption layers will result in a higher C_{bd} value in comparison with a simple *p-i-n* structure. Assuming, that all the breakdown events are confined only to the avalanche region, the C_{bd} of a SAMAPD structure is expected to be higher than a *p-i-n* structure with similar avalanche region thickness. However as far as the avalanche material is concerned, results in this thesis have demonstrated that thin $Al_{0.85}Ga_{0.15}As_{0.56}Sb_{0.44}$ layers are robust and have demonstrated stable avalanche gain under high temperatures in the linear mode. Keeping view the wide bandgap and reduced temperature coefficient of avalanche breakdown of $Al_{0.85}Ga_{0.15}As_{0.56}Sb_{0.44}$ in comparison with InP and InAlAs It will be interesting to compare the performance of $Al_{0.85}Ga_{0.15}As_{0.56}Sb_{0.44}$ GM-APD with InP and InAlAs single photon detectors.

As far as the low temperature operation of the SPAD will be concerned, it will be imperative to cool the device as the narrow bandgap $In_{0.47}Ga_{0.53}As$ absorber will excessively contribute to the *DCR* through thermal generation mechanism. In order to provide a comparison to the in-class Si SPADs, it will be instructive to remove the bandgap disparity between Si and AlGaAsSb SPADs by comparing the performance at temperature that compensates for the bandgap disparity. To elaborate this, we note that the thermal generation due to Shockley-Read-Hall (*SRH*) processes is proportional to $E_g/2kT$ where E_g is material bandgap, k and T the Boltzmann's constant and device temperature respectively. The factor of 2 is due to the mid-gap states in the material close

to energy levels of $E_g/2$. At room temperature the tem $E_g/2kT$ for Si (E_g = 1.6 eV) whereas for AlGaAsSb the similar value for $E_g/2kT$ is reached at - 70ºC. It will therefore be important to perform the *DCR* measurement of AlGaAsSb SPAD at low temperatures to compensate for the thermal generation from the narrow bandgap InGaAs absorber.

Appendix

Electric field calculation

Poisson solver is used to calculate the electric field profile of diodes used in this work. The model assumes a full depletion for all the layers except the 1st and n^{th} layer for an *n*-layer device structure. For a p^+-*i*-n^- layer structure which is the same structure as the linear and Geiger mode APDs of this thesis, let the doping in these layers be N_1, N_2 and -N_3 and the thickness of these layers be X_1, X_2 and X_3, the electric field gradient of position inside the layers is given according to Poisson equation in equation set 1 as,

$$\left(\frac{dE}{dx}\right)_1 = \frac{qN_1}{\varepsilon}, \left(\frac{dE}{dx}\right)_2 = \frac{qN_2}{\varepsilon}, \left(\frac{dE}{dx}\right)_3 = \frac{qN_3}{\varepsilon} \quad (1)$$

Where q and ε are electronic charge and permittivity of medium. Electric field at the junctions of the p^+-*i*-n^- layer can be written as,

$$E_1 = \frac{qN_1X_1}{\varepsilon}, E_2 = E_1 + \frac{qN_2X_2}{\varepsilon}, \text{ and } E_2 = -\frac{qN_3X_3}{\varepsilon} \quad (2)$$

Re-arranging and substitution of E_1 gives an expression for X_3 as,

$$X_3 = -\frac{(N_1X_1+N_2X_2)}{N_3} \quad (3)$$

Total voltage V_t developed across the structure as a result of the electric field at the junctions can be expressed as,

$$V_t = \frac{(E_1X_1+E_2X_3+(E_1+E_2)X_2)}{2} \quad (4)$$

Substituting Eq. 2 and 3 into 4 gives,

$$N_1\left(1-\frac{N_1}{N_3}\right)X_1^2 + 2N_1\left(X_2-\frac{N_2X_2}{N_3}\right)X_1 - \frac{(N_2X_2)^2}{N_3} + N_2X_2^2 - \frac{2\varepsilon V_t}{q} = 0 \quad (5)$$

Eq. 5 is a quadratic equation in variable X_1 and can be calculated as,

$$X_1 = \frac{-b\pm\sqrt{b^2-4ac}}{2a} \quad (6)$$

Where

$$a = N_1\left(1 - \frac{N_1}{N_3}\right), b = 2N_1\left(X_2 - \frac{X_2N_2}{N_3}\right), c = -\frac{(N_2X_2)^2}{N_3} + N_2X_2^2 - \frac{2\varepsilon V_t}{q} \quad (7)$$

Similarly, for a 5-region structure such as the one discussed in Fig. 5 chapter 5, the analysis yields the values of *a*,*b* and *c* as,

$$a = N_1\left(1 - \frac{N_1}{N_5}\right), b = 2N_1\left((X_2 + X_3 + X_4) - \frac{X_2N_2 + X_3N_3 + X_4N_4}{N_5}\right), \; c = -\frac{(N_2X_2 + N_3X_3 + N_4X_4)^2}{N_5} + N_2X_2^2 + N_3X_3^2 + N_4X_4^2 + 2N_2X_2(X_3 + X_4) + 2N_3X_3X_4 - \frac{2\varepsilon V_t}{q} \quad (8)$$

Where N_i and X_i are doping and thickness of i^{th} layer. For *n* layer structure, the 2nd to (*n-1*)th are completely depleted and the depletion in 1st and n^{th} layers can be calculated according to Eq. 3 and 7 (3-layers) and Eq. 3 (generalised for *n*-layers) and 8. The model requires user defined inputs of doping and thickness of the epitaxial layers and built-in voltage.